NTNU

Norwegian University of
Science and Technology

Superconducting magnetic energy storage in power systems with renewable energy sources

Knut Erik Nielsen

Master of Science in Energy and Environment
Submission date: June 2010
Supervisor: Marta Molinas, ELKRAFT

Norwegian University of Science and Technology
Department of Electric Power Engineering

Problem Description

The work on the master will be focused on a comparative evaluation of power conditioning systems for interfacing SMES to power systems for load levelling applications. Current source and voltage sources solutions will be evaluated based on the requirements for filtering, reactive power support and losses of the converter. A conditioning system will be designed and dimensioned considering available devices in the market today. The conditioning system will be tested by simulation in the network model used for the project part of this study.

Assignment given: 26. January 2010
Supervisor: Marta Molinas, ELKRAFT

Abstract

The increasing focus on large scale integration of new renewable energy sources like wind power and wave power introduces the need for energy storage. Superconducting Magnetic Energy Storage (SMES) is a promising alternative for active power compensation. Having high efficiency, very fast response time and high power capability it is ideal for levelling fast fluctuations.

This thesis investigates the feasibility of a current source converter as a power conditioning system for SMES applications. The current source converter is compared with the voltage source converter solution from the project thesis. A control system is developed for the converter. The modulation technique is also investigated.

The SMES is connected in shunt with an induction generator, and is facing a stiff network. The objective of the SMES is to compensate for power fluctuations from the induction generator due to variations in wind speed. The converter is controlled by a PI-regulator and a current compensation technique deduced from abc-theory. Simulations on the system are carried out using the software PSIM. The simulations have proved that the SMES works as both an active and reactive power compensator and smoothes power delivery to the grid. The converter does however not seem like an optimum solution at the moment. High harmonic distortion of the output currents is the main reason for this. However this system might be interesting for low power applications like wave power.

Preface

This report concludes my master thesis at Norwegian University of Science and Technology (NTNU).

I would like to thank my supervisor Marta Molinas, ph.D student Alejandro Garces for assisting me in my work. I would also like to thank my good friends Nathalie, Kristian and Mari for helping me and making the hard days at the office easier.

Knut Erik Nielsen
Trondheim, Norway

Contents

Chapter 1

Introduction

The ever increasing demand for energy is one of the biggest challenges in the world today. The combination of the threat from climate changes, increased environmental focus and peak oil forces the introduction of new renewable energy sources. There is no single renewable energy source which points itself out to be the only solution [1]. The different energy sources have to be combined. The most promising new renewables for large scale use are onshore and offshore wind energy, wave energy, solar energy and tidal energy. There are several issues regarding large scale introduction of renewable energy sources like these. One of the issues is the quality of supply. More specific it is not possible to control the power output from a wind park or a wave power plant like it is for hydropower. These energy sources will deliver or not deliver energy independent of the demand. There can also be variations within a relatively short time span. These variations can occur due to wind gusts, clouds shadowing for the sun or other random events. These phenomena present challenges which have to be solved before the new renewables can provide the base load. A solution to this problem is the concept of energy storage. There are several different types of energy storage. Fig. 1.1 shows different concepts and their properties regarding output power and output duration. These can mainly be divided into two groups. One type is the energy storage solutions having the ability to store large amounts of energy but have slow reacting times, in the other end are devices which have poor energy storage capacity but react faster. Pumped hydro has large output power and it has the ability to supply power for a relatively long time. However it has a long start-up time and is not suitable for fast fluctuations as the afore mentioned. For these types of disturbances the SMES (Superconducting Magnetic Energy Storage) is most suitable having a very fast reaction time and relatively large power output.

The main task of this master thesis is comparison of power conditioning

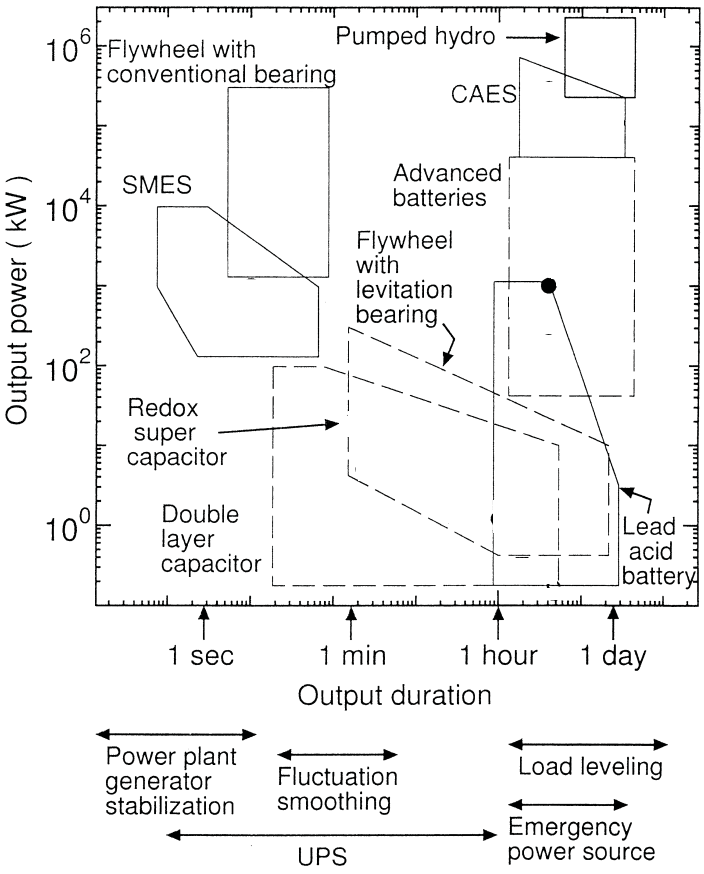

Figure 1.1: Range of output power and output duration for different energy storage concepts [2].

systems which connects a SMES system to the power grid. Both current source and voltage source typologies will be evaluated. The purpose of the SMES is to level out power fluctuations from a generator which supplies an interconnected power network. The system response is studied using simulation software. Loss characteristics are also taken into consideration.

Chapter 2

Wind energy

Wind energy is one of the most promising renewable energy sources available. The worldwide production is increasing every year, and the installed capacity reached 159 GW in 2009. Despite the financial crisis an increase rate of 31.7% occurred from 2008. This was the highest increase rate since 2001, and a decline is not anticipated. The worldwide capacity is expected to exceed 200 GW in 2010. The total electricity generated from the installed wind power plants installed by 2009 will add up to 340 TWh. This equals 2% of the world's electricity production. The target in the European Union of having a share of 20% renewables in the power system by 2020 will contribute to further growth of wind power. In 2008 a report on the topic of increasing the wind energy percentage to 20% by 2030 was released by U.S. Department of Energy [3]. According to this report the installed capacity would have to increase from 11.6 GW in 2006 to 305 GW in 2030. In 2009 the installed capacity was 35 GW meaning that the building rate would have to increase in order to reach the target.

A large share of wind power will result in a number of challenges in the power system [4]. One of the two most basic ones is the challenge of how to keep the voltage on an acceptable level for all customers at all time. The other is how the fluctuating nature of wind power can meet the power demand in the system. Wind energy is already integrated in some power systems with a medium penetration level (18% - 31%) in some regions in Denmark and Germany. However these regions are connected to strong networks which are able to manage the power fluctuations from wind energy. High penetration of wind power makes demands such as flexible sources in the network. Nuclear power for instance is regarded as a very inflexible, and should be operated on constant power to cover base loads. Other thermal power sources are also desirable to operate on constant power because of the narrow maximum efficiency band. Hydropower is a flexible source which is possible to operate

on a start and stop basis. However hydropower is a limited resource which not every country is benefited by having. It is obvious that some measures need to be taken. The various nature of wind power generation can be seen by the following equation, which gives the power in the wind in watts:

$$P = \frac{1}{2}\rho A V^3 \tag{2.1}$$

ρ is the average air density, A is the area swept by the turbine blades, and V is the wind speed in m/s. It is not possible to extract all of the power in the wind using a wind turbine as this would make the kinetic energy in the wind equal to zero. The result of this would be accumulation of air masses behind the turbine, and thereby a wall of air meeting the incoming wind. Because of this there is a theoretical optimum of how much which is possible to extract. This limit was discovered by Betz in 1926, and introduces a constant (the Betz limit) in Eq. 2.1. The Betz limit is equal to 16/27 or 0.59 [5]. This means that maximum 59% of the energy in the wind can be utilized by the wind turbine. In addition are the different losses in the mechanical and electrical system before the kinetic energy in the wind is converted to electrical energy.

There are two different types of turbine generator systems. These can be divided into:

- Fixed speed systems.
- Variable speed systems.

In a fixed speed system the generator is of the squirrel cage induction generator type. This is connected directly to the grid, and runs at nearly constant speed. The small speed variations are in the range of 1-2 % around rated speed. The simplicity of this system is its advantage. Among disadvantages is the more robust, and thereby expensive, construction than its variable speed counterpart. Because the invariability of the turbine speed, wind speed variations are lead into the drive train as torque variations.

In a variable speed system the mechanical speed of the wind turbine has to be decoupled from the frequency of the electrical grid. To implement this, a power electronic converter has to interface the generator and the grid. By doing this, the generator can operate on different velocities than the one which correspond to the frequency of the grid [6]. The emphasis in this thesis is on the fixed speed system and the variable speed systems will not be further dealt with.

It is evident from Eq. 2.1 that the power output from a wind turbine is heavily dependent on the wind speed. This is at least true between the cut-in speed, which is the wind speed where the turbine starts to generate power,

and the rated power wind speed. The cut-in speed is normally in the range $3 - 5$ m/s, and the rated wind speed is in the range $12 - 16$ m/s. When the wind speed exceeds the rated power speed the blades are normally pitched to keep the output at the rated power level. Because of this some of the power in the wind remains unexploited, but the output power from the turbine is more predictable. The turbine is usually stopped when the wind speed goes beyond 25 m/s. The pitch control can be used for compensating for fast wind speed variations. However in many systems the dynamics of the actuators controlling the blades are too slow to do this and are only used for limiting the power output [7].

Fig. 2.1 shows the annual wind distribution and the annual energy production by a turbine with a blade diameter of 60 m. It has a MAWS (Mean Annual Wind Speed) of 7 m/s. The graph is of course not equal for every site, but it has more or less the same shape. The essential information to withdraw from the two graphs are that the extreme wind speeds occur very infrequently and contribute to a small amount of the energy production. It is also clear that the low wind speeds which occur quite often neither contribute to a large share of the energy production. The largest contribution comes from the wind speeds around the rated wind speed. Fig. 2.1 does not show how effective the plant is compared to its theoretical potential, meaning how productive it is. The capacity factor c_f gives this information. It is defined as:

$$c_f = \frac{\text{actual yearly energy production}}{\text{maximum plant rating} \times 8760} \tag{2.2}$$

The energy production is given in watt-hours, the plant rating in watt and 8760 equals the amount of hours in a year. The capacity factor is dependent on the wind speed. A plant having a MAWS of 7 m/s has a capacity factor about 30 %, but if the MAWS is 5 m/s the capacity factor drops to 12 %. c_f will of course never reach 100 %. The consequence of this is that the installed capacity of wind power plants must be larger than for thermal power plants which have higher capacity factors [4].

The power output from wind power plants will fluctuate. According to a study made in 1957 the wind speed will vary with three distinct frequencies [8]. One frequency which is around one minute, another which is around 12 hours and the third is about four days. These variations are caused by turbulence, diurnal variations and long term weather systems. The two last variations can be predicted with fairly good certainty. Weather forecast is very important when it comes to good operation of power systems having rather high penetration of wind power. The short term fluctuations are not possible to predict in the same manner. The short term variations are strongly coupled with the size of the wind park, more specifically the number of

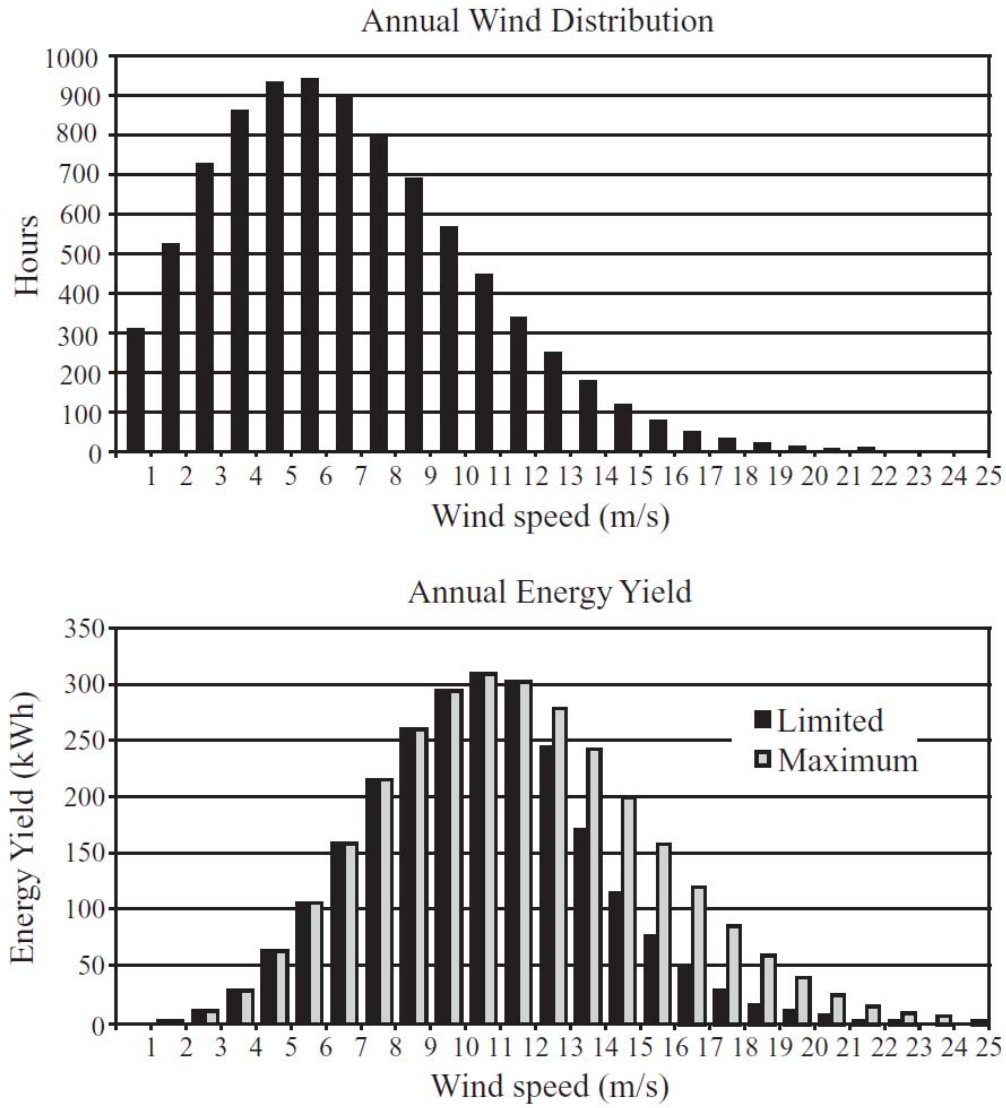

Figure 2.1: The annual production by a turbine of 60 m diameter [8].

wind turbines. The aggregation of many turbines will damp the fluctuations heavily [9]. This comes from the fact that wind gusts will very seldom hit a large part of the turbines at the same time. Some turbines can experience an increase in power output, while others a decrease. According to [9] the maximum change in one second at a 100 MW wind park was ± 2.5 MW during three months of measuring. The average change in one second was zero. This result certainly shows the positive aspects of several turbines in one

area. For distributed generation the case is totally different and the power output fluctuations can be quite severe for a single turbine. This introduces the requirement for energy storage. An energy storage unit which covers the fast power fluctuations from a single turbine will improve the power quality from the power plant. A SMES unit will be a suitable technology for this purpose as it can deliver high power. The necessity for storing large amounts of energy is not present for covering the fast fluctuations. For covering the fluctuations having longer duration a SMES system will probably not be suitable.

Chapter 3

Superconducting Magnetic Energy Storage

Parts of this chapter is taken from the project thesis.

3.1 The principles of superconducting magnetic energy storage

Energy stored in a normal inductor will fade out rather quickly due to the ohmic resistance in the coil when the power supply is disconnected. Obviously this will not be an acceptable energy storage for use in a power system. The ohmic resistance has to be removed before an inductor can work for this purpose. This is possible by lowering the temperature of the conductors, and by this making the conductors superconducting. A superconducting wire is in a state where the resistance in the material is zero. In this state the current in a coil can flow for infinite time. This can also be seen from the time constant of a coil $\tau = \frac{L}{R}$ where R goes to zero and τ then goes to infinity. There are constraints for a superconducting wire to stay superconducting. The conductor has to be operated below a critical temperature T_c, below a critical current I_c and below a critical magnetic field H_c. There should also be some safety margin between the critical values and the operating conditions [10].

There are several types of superconducting material. They can be divided into two groups. High Temperature Superconductors (HTS) and Low Temperature Superconductors (LTS). The HTS types are cooled to 77 K using liquid nitrogen. A LTS is generally cooled using liquid helium to 4.2 K [10]. There are advantages and drawbacks attended with both the technologies.

Liquid nitrogen used for cooling HTS is much cheaper than the liquid helium used for LTS. It is also an advantage having the higher operating temperature. One disadvantage regarding HTS is the fact that the materials being used are brittle and hard to shape, at least into the form of a coil. The price is also much higher than for the LTS. Because of this the LTS is generally used for SMES. In a superconducting coil the normal conductor material is the LTS alloy Niobium-Titanium (Nb/Ti) [11]. This becomes superconducting when the temperature drops below 9.8 K [10].

The need for cooling to 4.2 K is a drawback comparing SMES with other forms of energy storage. It lowers the efficiency and introduces refrigerators and compressors to the system which lower the reliability. The superconducting coil itself has very good lifetime. In a test of a SMES system in Bonneville, US in the 1980s a total of 10^6 charge and discharge cycles were completed of a total planned 10^7. The reason for not reaching the planned number was not because of the inductor but problems with the refrigerator [12]. The coil itself showed no sign of wear. Despite losses in the non superconducting parts of the system, and energy needed for cooling, the total efficiency of a SMES system can exceed 90%, a lot higher than for pumped hydro (70%) and batteries (70-90%). The reason for the high efficiency is that there is no need to convert the energy between different forms, chemical to electrical or mechanical to electrical. SMES is together with capacitors the only energy storage form which is a pure electrical [13].

SMES has a rather poor energy storage capacity compared to pumped hydro or Compressed Air Energy Storage (CAES). There are conceptual design studies for large scale SMES systems which can operate in diurnal power compensation having the ability to store large amounts of energy [14]. This makes use of several thousand coils to store the energy. However this is only a study case and a real system is not likely to be constructed in the near future. While the energy density of a SMES system is low, one of the main properties of SMES is the ability to deliver large amounts of energy in a very short time, or said in another way, deliver high power. Combined with very short response time, this makes SMES one of the most suitable energy storage solutions to compensate for fast power fluctuations.

Summed up the features of SMES are the following:

- Capability of absorbing and delivering large amounts of power.
- High efficiency.
- Long lifetime.
- Short response time.
- Completely static construction, low maintenance.
- All electric energy storage

3.2 Experimental testing of a superconducting coil

During the project thesis in the autumn an educational trip to Tokyo Institute of Technology, Japan was performed. The purpose of the trip was to participate in a laboratory experiment on a superconducting coil which took place in November 2009. Due to problems and delays the experiment did not finish before the stay was over and the results were not ready until the delivery date of the project. Because of this the experiment results are included in this thesis.

In a superconducting coil strong electromagnetic forces caused by the high currents and strong magnetic fields cause big challenges when it comes to the construction of the coil [14]. A large-scale SMES would require rigid supports and a very strong construction. Traditional topologies such as solenoids and toroidal field coils experience these issues strongly. The only current component in the solenoid is in the toroidal direction, see Fig. 3.1a. Axial forces exert compressive stress on the solenoid. Forces in the radial direction, also called hoop forces, cause tensile stress in the toroidal direction which strain to widen the solenoid. In a toroidal field coil (TFC), which is made up of several solenoids the only current component is in the poloidal direction, see Fig. 3.1b. The hoop forces which work on each of the solenoids exert tensile stress in the poloidal direction. Compressive stress is generated in the toroidal direction due to the compressive forces which work towards the centre. All these forces require strong constructions in order to not tear the coil apart.

The concept of balancing the electromagnetic forces is used in the forced balanced topology (FBC). Using this typology it is also possible to control the distribution of the stress. The method of doing this is by choosing an optimum winding configuration. The number of poloidal turns which is the optimum is calculated using the following formula [14]:

$$N = \sqrt{\frac{\alpha \ln 8\alpha(\sqrt{\alpha^2 - 1} - \alpha)}{\alpha^2 + 1}} \tag{3.1}$$

The variable in the formula is α which is the aspect ratio. This is equal to the radius of the torus divided by the radius of the torus cross section (α = torus radius/torus cross section radius). Fig. 3.2 shows the concept of FBC. It indicates that the coil is composed by several windings, each having the same number of poloidal turns. By having both poloidal and toroidal current components, the tensile stress in a pure solenoid will be equalized by the compressive stress in a TFC. The forces in the radial direction will

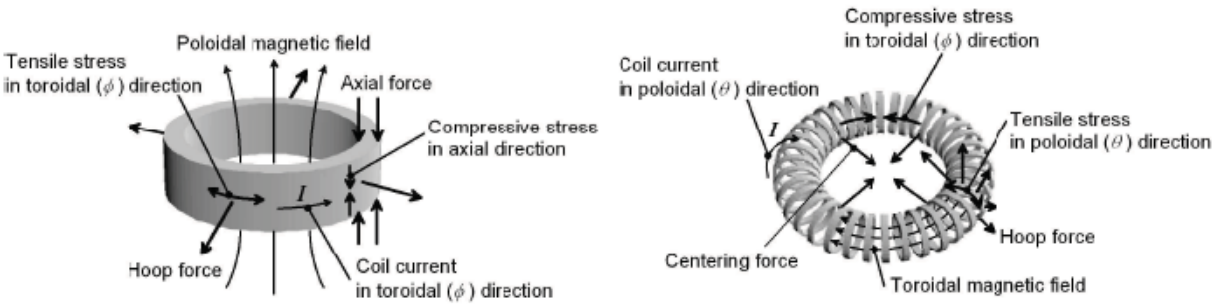

(a) Solenoid (b) Toroidal field coils

Figure 3.1: Electromagnetic forces and mechanical stress in traditional topologies [14].

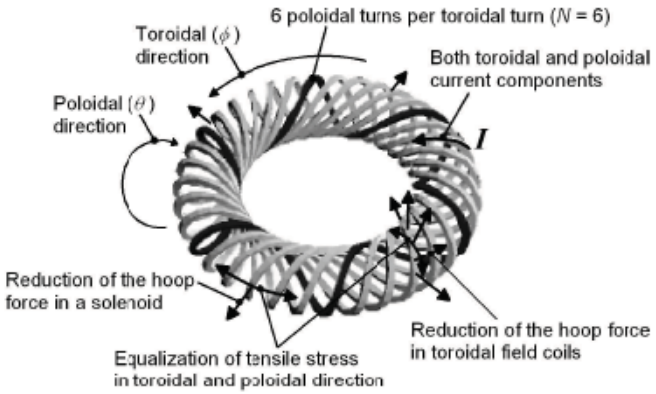

Figure 3.2: The winding configuration and mechanical stress in a FBC.

also work against each other. As a result of the smaller resultant stress it is possible to reduce the total mass of the coil structure for the same magnetic energy stored. Theoretically it is feasible to bring down the total mass to a quarter compared to a TFC and more than halve it compared to a solenoid. A property like this would be of great importance for large scale SMES.

The superconducting coil in the experiment was constructed as a FBC. The coil with its dimensions is shown in Fig. 3.3a. It is composed of three helical windings. Each helical winding does six poloidal turns, and is composed by an inner and outer winding block. The schematic of the coil is shown in Fig. 3.3b. Each of the inner winding blocks consists of 329 turns and each of the outer winding blocks has 259 turns. Together this gives 10584 turns, and an inductance of 1.8 H. Other parameters can be found in Appendix A.

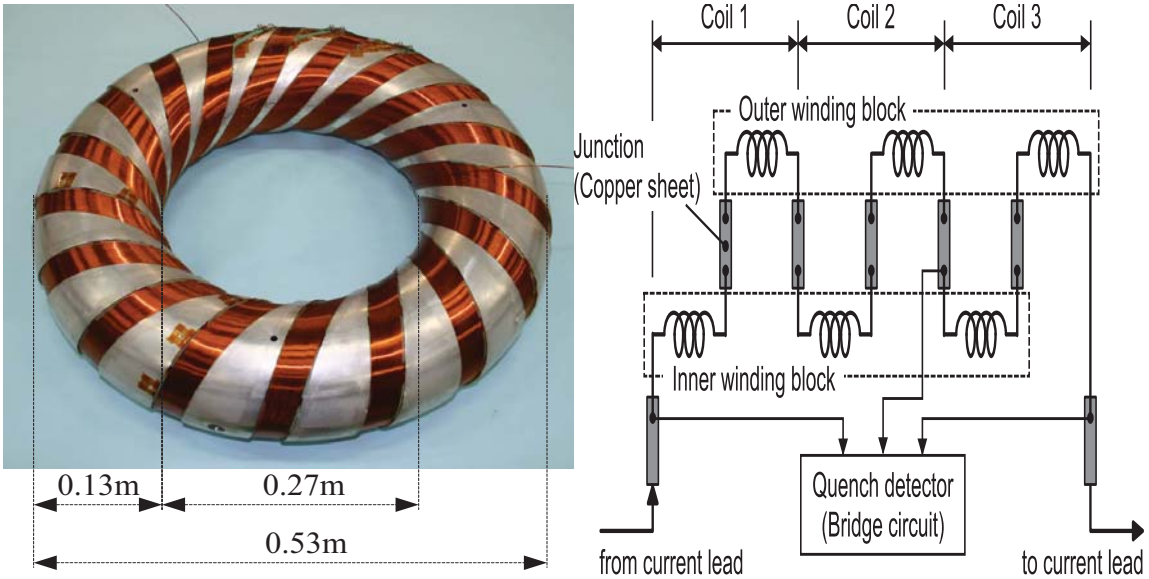

(a) The bare force balanced coil.

(b) The composition of the FBC.

Figure 3.3

During the experiment the coil was kept inside an isolated container. The laboratory setup is displayed in Fig. 3.4. The two large tanks on the left contained liquid helium, used to cool the FBC. The total amount of helium used in the experiment was 5000 l. The smaller container to the right contained the FBC. The current cables were connected to the top of the container. It is possible to spot frost on top of the container which was formed from the condensed humidity in the air.

The critical limits for superconductivity of the FBC were three parameters. Current, magnetic field and temperature. The current limit was 552 A. The magnetic field limit was 7.1 T. The coil became superconducting below 9.8 K, but to obtain high values of current and magnetic field the temperature limit was 4.2 K,the temperature of liquid helium which was used as cooling agent. The test runs starting in November 2009 was the fourth series of test runs. The first was in February 2007, second in September 2007 and third in March 2008. Even though the critical current of the FBC is 552 A the coil was never exited to this value in the first three test runs. A transition from superconducting state to normal conducting state occurred before this value was reached. This phenomena is called ”quench”. The first quench in February 2007 happened at 293 A and 3.8 T, only 53 % of the critical limits. However the quench currents increased from test run to test run. In the third test run, the highest quench current was 476 A, 86 % of the cur-

Figure 3.4: The experimental setup in the laboratory. The two left tanks contain liquid helium. The right one contains the superconducting coil.

rent limit. The phenomena of increasing quench currents is called ”training”. The physics behind the quench and training is not fully understood. It is believed to have something to do with the position of each of the superconducting strands which compose the windings. When the current increases the electromagnetic forces on the strands increase. At a certain current, the force will become too big for the strand to keep in position, and it will move slightly. This small movement will result in a temperature increase, and move the FBC out of its limits, and a quench occurs. The complex winding configuration and the fact that it is handmade will make some imperfections in the windings. To improve the quench performance an optimized winding technique is necessary.

The objective of the test run in November 2009 was to investigate the effect of using super cooled liquid helium at a temperature of 2.17 K. The method of doing this was to reduce the pressure inside the FBC Dewar below one atmosphere using a vacuum pump. By doing this a larger margin from operating conditions to the quench limits would be present. The circuit in the experiment is shown in Fig. 3.5. The DC-power supply is connected to

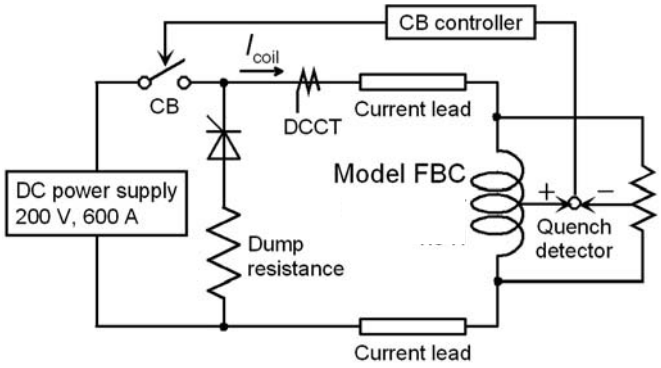

Figure 3.5: The circuit in the FBC experiment.

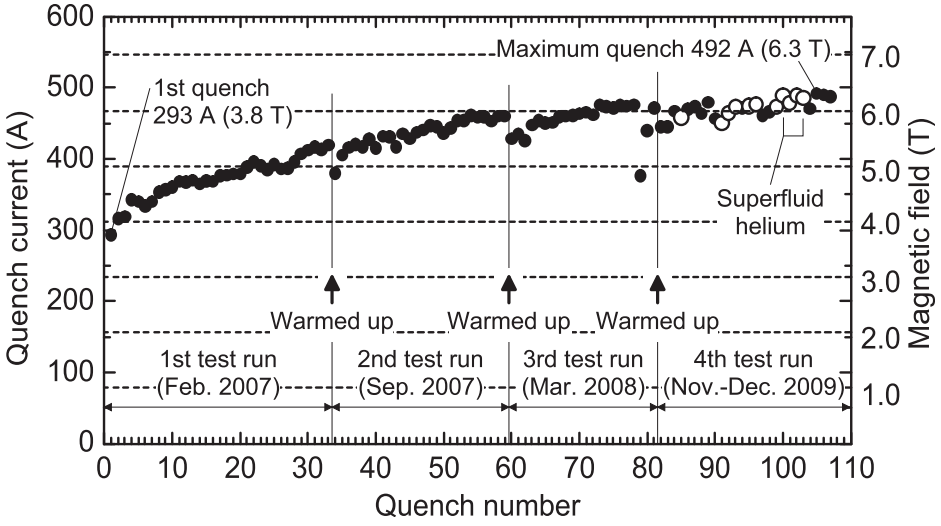

Figure 3.6: The training effect of the FBC.

the network through a thyristor rectifier. The branch containing the dump resistance is connected using a thyristor when a quench is detected. At the same time the circuit breaker (CB) is opened.

The result of the experiment and the training effect can be seen in Fig. 3.6 and Table 3.1. The current ramp rate was 1 A/s. The current values were read from an ammeter on the DC-source. The magnetic field was calculated from the current, and corresponded to the toroidal field. The quench current increased for each test run, but the first quench current when a new test run started was lower than the last at the previous test run. However the quench current was not reduced to the value for the first quench. This showed that the training effect not disappeared after the coil was warmed to room temperature. The record quench current occurred on the 105th quench.

Table 3.1: The quench currents and magnetic fields in the fourth test run.

Quench no.	*Quench current (A)*	*Magnetic field (T)*	*Temperature (K)*
82	445	5.7	4.2
83	445	5.7	4.2
84	467	6.0	4.2
85	458	5.9	2.6
86	470	6.0	4.2
87	473	6.1	4.2
88	464	6.0	4.2
89	480	6.2	4.2
90	457	5.9	4.2
91	451	5.8	2.6
92	464	6.0	2.3
93	473	6.1	2.2
94	472	6.1	4.2
95	474	6.1	2.3
96	477	6.1	2.3
97	461	5.9	4.2
98	466	6.0	4.2
99	473	6.1	2.2
100	489	6.3	2.1
101	479	6.1	2.1
102	489	6.3	2.0
103	486	6.2	2.0
104	471	6.0	4.2
105	492	6.3	4.2
106	490	6.3	4.2
107	487	6.2	4.2

492 A corresponded to 89 % of the maximum coil current. This was an increase compared to the lowest quench current in the fourth run of 10.6 %, and to the all time lowest of 67.9 %. The record quench current did however not come when the FBC was cooled using the super cooled helium, but at the normal temperature of liquid helium. The difference between the quench current at super cooled conditions and normal conditions were not big, which indicated that the temperature difference of a few Kelvin were not crucial. The reason for this could be that the margin from around 2 K to the superconductivity limit was too small anyway when a strand moved and there was a temperature rise. The procedure of cooling the liquid helium further from 4.2 K was done by reducing the helium gas pressure inside the Dewar. This was a slow process as the pressure decreased, and limited the amounts of tests per day. Problems with the vacuum pumps did also cause problems in the experiment which decreased the amounts of test runs using super cooled liquid helium. Taking these problems into consideration, reaching 89 % of the theoretical limit was satisfactory. Especially when regarding the complex winding configuration of the FBC.

Chapter 4

The System Topology

The system which is studied in this thesis is shown in Fig. 4.1. The components in the system are a wind turbine, a gear box, an induction generator, two transformers and a connection to a main grid and the SMES and converter system. The power in the system is generated by the wind turbine. This is connected through an ideal gearbox to an induction generator. The gearbox has a transmission ratio of 1/100. The wind turbine is on the slow rotating side. The wind turbine is based on the one used in [15]. This has a rated wind speed of 12 m/s and rated power of 2 MW. The wind turbine has no pitch control which makes the power output completely dependent on the wind speed. This may seem unrealistic, but the scope of this thesis is studying the compensation of power fluctuations due to wind speed variations using SMES. A slow pitch control would not contribute to this smoothing. The induction generator is of the normal squirrel cage type. It has a rated power of 2 MW. The generator is connected to the grid through a transformer (T1) having a ratio of 690/1100 V. The main grid is connected to magnetize the induction generator, and supply the constant frequency and stiff voltage. The main grid is also the part of the system which it is desirable to control the power flow to. The converter is connected in shunt with the grid through a transformer (T2). The ratio of this is 1100/1100 V. The purpose of it is mainly to act as a filter. The converter is of current source converter type as distinct from the converters in the project thesis which were voltage source converter and a DC-DC chopper. All the lines in the system are modeled as ideal, having no impedance. The capacitances at the input of the converter acts as a filter together with T2. The system frequency is 50 Hz. Detailed overview of the wind turbine, the generator and the transformer parameters can be found in Appendix B.

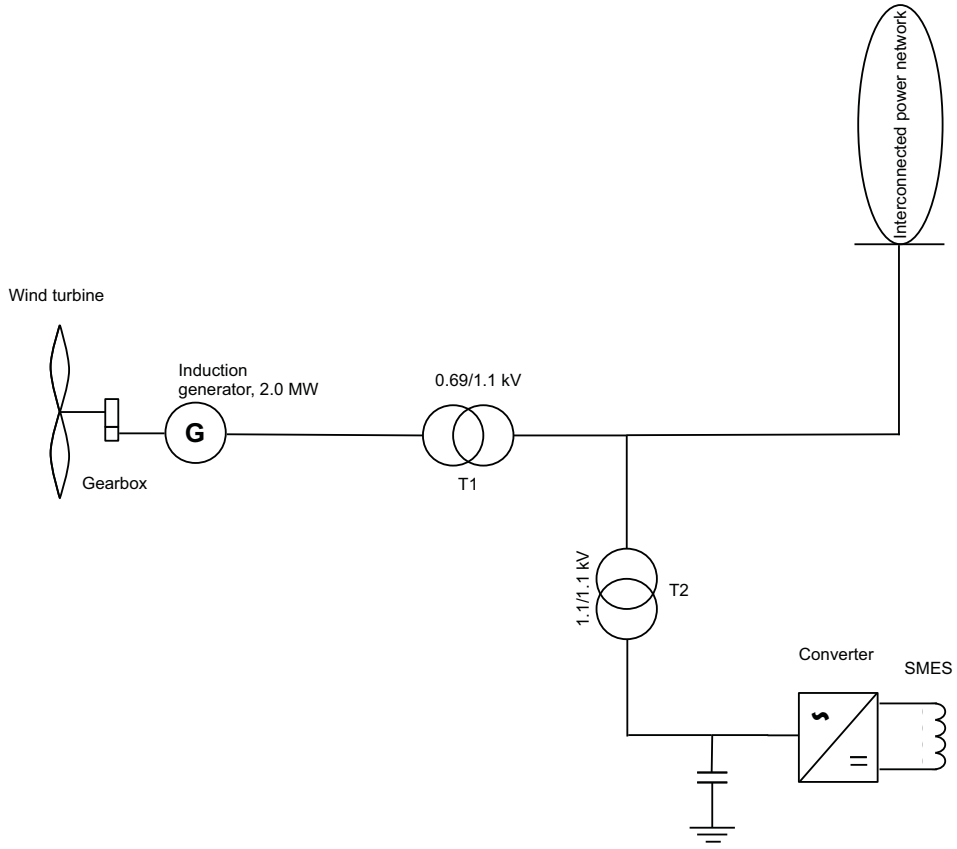

Figure 4.1: Single line diagram of the system being studied.

4.1 Per unit representation of the system

Per unit (pu) system analysis generally makes the calculations a lot easier. Especially when calculations are made in a system where there are several voltage levels. If the reference values are selected properly, transformation to a pu-system removes the transformers from the calculations. All of the different values of voltage, current, impedance and power will normally be in the interval 0 - 1.0. This makes the comparison between different voltage levels easier than if the physical values were used. It is easy to distinct between normal state and fault state. There are different strategies for deciding the base values for voltage. In power system analysis the RMS values of the phase to ground voltage or line to line voltage is normally set as voltage reference [16]. However in this project the base for the voltage is chosen as the peak value of the phase to ground voltage. The following value is chosen

as the power reference in the system, this corresponds to the rated power of the generator:

$$S_r = 2.0 \text{ MVA} \tag{4.1}$$

The two voltage references in the AC-part of the system are chosen as the peak value of the phase to ground voltages of the primary and secondary side of the transformers. V_{r2} is also equal to the rated voltage of the induction generator.

$$V_{r1} = \sqrt{\frac{2}{3}} \times 1100 \text{ V} = 898.15 \text{ V} \tag{4.2}$$

$$V_{r2} = \sqrt{\frac{2}{3}} \times 690 \text{ V} = 563.38 \text{ V} \tag{4.3}$$

The base current and impedance on each side of the transformers are:

$$I_{r1} = \frac{2}{3}\frac{S_r}{V_{r1}} = 1484.53 \text{ A} \tag{4.4}$$

$$I_{r2} = \frac{2}{3}\frac{S_r}{V_{r2}} = 2366.67 \text{ A} \tag{4.5}$$

$$Z_{r1} = \frac{V_{r1}}{I_{r1}} = 0.605 \ \Omega \tag{4.6}$$

$$Z_{r2} = \frac{V_{r2}}{I_{r2}} = 0.238 \ \Omega \tag{4.7}$$

The reference frequency in rad/s is necessary to calculate the pu-values of inductances and capacitances:

$$\omega_r = 2\pi f_r = 100\pi \text{ rad/s} \tag{4.8}$$

The DC-side of the inverter should also be transformed to pu-values. The reference value of the DC-link voltage is chosen to be two times the AC-side reference voltage:

$$V_{dcr} = 2\sqrt{\frac{2}{3}} \times V_{r1} = 1466.67 \text{ V} \tag{4.9}$$

The reference current is calculated by using the three phase power. Considering the AC-power equal to the DC-power gives:

$$S_{3ph} = 3V_{ph}I_{ph} = \frac{3}{2}V_{r1}I_{r1} = V_{dcr}I_{dcr} \tag{4.10}$$

Eliminating the voltages gives:

$$I_{dcr} = \frac{3}{4} I_{r1} = 1113.40 \text{ A} \tag{4.11}$$

And the reference impedance for the DC-side:

$$Z_{dcr} = \frac{V_{dcr}}{I_{dcr}} = 1.317 \ \Omega \tag{4.12}$$

4.2 The converter

The ideal converter topology used to connect the SMES system to the rest of the network will have no harmonic distortion, no usage of reactive power and no losses. These requirements are of course not possible to fulfil, and the choice of topology will be a compromise between the different aspects. A line commutated converter using thyristors has low on-state losses and the thyristor devices can cope with large amounts of power. The disadvantages are lagging power factor and high low order harmonics pollution. Neither does a thyristor converter provide the same degree of control as a self-commutated converter. The requirement of a present strong grid is also a drawback considering line-commutated converters. Because of these disadvantages a self-commutated converter is chosen.

When choosing the converter type among self-commutating types there are mainly two different types to choose from. They are the voltage source converter type (VSC), see Fig. 4.2a and the current source converter type (CSC), see Fig. 4.2b. In a VSC the DC-voltage will always have the same polarity. Bidirectional power flow of the converter is achieved by reversing the DC-current polarity. In a CSC the DC-current will always flow in the same direction and the bidirectional power flow is achieved by reversing the DC-voltage polarity. The VSC has a big capacitor on the DC-side. This is sized to be large enough to sustain the voltage in the DC-link on a constant level for the expected operating conditions. Because the current flow can be bidirectional, the so called converter valves also have this feature. As Fig. 4.2a shows this is normally solved having a diode connected in antiparallel with the switching device which very often is an IGBT. Because the DC-voltage never switches polarity, there is no need for reverse blocking capability. A CSC will need a blocking diode in series connection with the switching device in absence of reverse blocking capabilities in a normal IGBT. [17].

The CSC and VSC topology have quite different properties, and because of that they have different advantages and disadvantages. The VSC has the advantage of having lower harmonic pollution. The CSC needs capacitors on

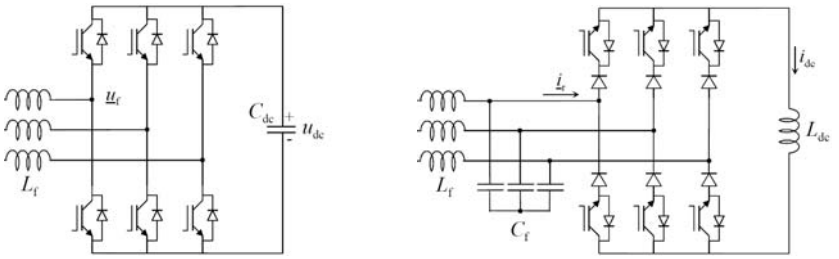

(a) Voltage source converter. (b) Current source converter.

Figure 4.2

the AC-side to filter out harmonics. The reason for this is the rapid changing current pulses which are created from the switching of the continuous DC-current. The capacitors provide a stiff bus interfacing the converter. These filter capacitors are expensive and bulky and are clearly a disadvantage compared to the VSC. A drawback with the VSC is that the switches are more vulnerable to high short circuit currents. If two switches on the same leg are on at the same time the DC-voltage will be short circuited and a large current will flow. This can cause failure of the converter. In a CSC the short circuit current is limited by the coil. In fact a short circuit of one leg normally happens several times during one cycle. Another drawback regarding the VSC is the capacitor on the DC-side. This has limited lifetime compared to the inductor in a CSC [18]. Despite these drawbacks the VSC configuration is by far the preferred over the CSC. The reasons have normally been economics and performance.

In this master project the purpose is to study a CSC and its feasibility in SMES applications. The converter which has been used is the CSC shown in Fig. 4.3a. This converter is different from the converter used in the project thesis which is shown in Fig. 4.3b. The fact that the superconducting coil is a current source requires another converter in addition to the VSC, a DC-chopper. This is placed on the DC-side to directly manage the current in the coil. The process of feed in and extraction of energy is quite different in the two topologies. In a CSC the energy management is directly to and from the coil as there is only one converter interfacing the power system. In the VSC/DC-chopper topology the energy management in the SMES is a two step procedure. If extracting energy from the SMES, the energy is as a first step withdrawn from the DC-link capacitor. The capacitor is then charged again by the superconducting coil. If feeding energy into the SMES, the capacitor is first charged and then it charges the superconducting coil. Compared to a CSC solution the VSC will as a consequence of this have faster response because of the DC-link capacitor which can deliver large cur-

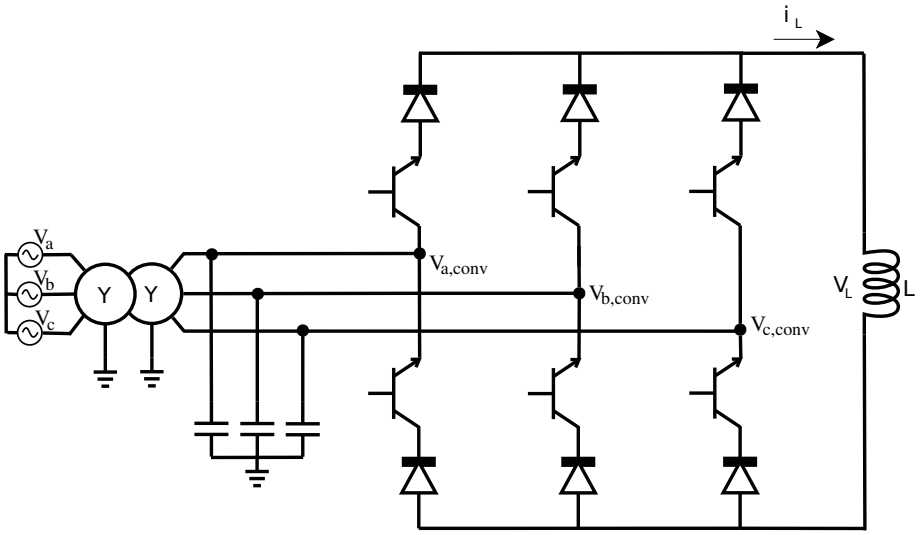

(a) The CSC linking the system and the superconducting coil.

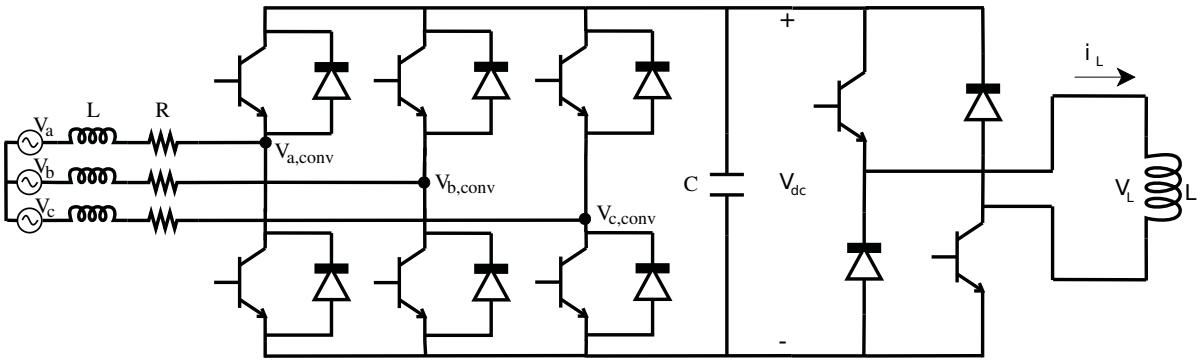

(b) The VSC and DC-DC chopper linking the system and the superconducting coil in the project thesis.

Figure 4.3: The two different converter topologies to connect the superconducting coil to the grid.

rents quicker than an inductor as this does not allow instantaneous change of current. The larger inductance, the slower response time is present. A disadvantage regarding the capacitor is as mentioned its limited lifetime. This ad to the running expenses of the converter. In a CSC topology the DC-DC chopper is superfluous. Because of this the control system can be made simpler than for the VSC solution. A drawback of the conventional CSC is the requirement of blocking diodes. This increases the amount of semiconductors the current has to flow through, and thereby increase the conduction

losses. A reverse blocking IGBT would help decreasing these losses as this does not require a blocking diode. On the other hand the VSC/DC-chopper topology has fewer semiconductor devices conducting in the VSC part, but it also has semiconductors in the DC-chopper which contribute to losses. The number of semiconductors the current flows through is actually higher for the VSC/DC-chopper solution than for the CSC. The reason for this is that three half-legs is on compared to two in the CSC. Together with the devices in the chopper this equals five devices to pass compared to four in the CSC. However two of the half-legs in the VSC will share the current making the load on each unit smaller.

4.2.1 Sizing of the converter

The two constraining factors on the switching units are applied voltage and the current in the SMES coil. The voltage applied gives the rate of change of the current according to the following equation:

$$V_L = L\frac{di}{dt} \tag{4.13}$$

From this follows that the SMES will be able to charge and discharge faster the higher the applied voltage is. This also implies that the power in the SMES will be higher. The rated turbine power in the system is as mentioned 2 MW. To cope with power oscillations from the turbine the SMES system should be able to cover fluctuations in the megawatt range. The purpose of the system in this thesis is to cover for fast power fluctuations, not for diurnal variations. On basis of this the rated power of the converter is selected to be 1.5 MW. As is well known this is equal to 1.5 MJ/s. To store 1.5 MJ the current flowing, can be calculated using:

$$W_L = \frac{1}{2}LI^2 \tag{4.14}$$

The inductance of the superconducting coil is 1.8 H, a value found to be suitable in the project thesis. The rated current is then 1290 A. This will be the maximum operating current and the switches must be rated to cope with this current. Reverse blocking diodes will as mentioned decrease the losses. However these IGBTs are not rated for high power usage. A prototype device described in [19] is rated at 600 V and 200 A. The manufacturer IXYS can currently deliver RB-IGBTs with a rating of 1200 V and 55 A [20]. These rather poor ratings strongly limit their feasibility in energy storage capability like SMES.

ABB has in a document given guidelines to choose the voltage ratings of high power semiconductors [21]. These are taken into account when devices have been chosen here. It is important that there are safety factors compared to the operating voltage. On the other hand the semiconducting devices should not be selected having to high ratings as this would increase the losses. The CSC is subjected to AC-voltage, and it is the peak of this which is interesting. The peak of the AC-voltage is calculated and a certain safety margin, x is added:

$$V_{ACpeak} = \sqrt{2} \times V_{NOMRMS} \times (1 + \frac{x}{100}) \tag{4.15}$$

The safety factor varies according to the application, but 15 % is not unusual. The maximum repetitive peak forward voltage is calculated according to:

$$V_{DR} = V_{ACpeak} \times (1 + \frac{y}{100}) \tag{4.16}$$

In the system studied here the results from Eq. 4.15 and Eq. 4.16 are given below. The semiconductors used in the simulations in this thesis are models

Table 4.1: The dimensioning voltages.

V_{NOMRMS}	V_{ACpeak}	V_{DR}
1100 V	1700 V	2900 V

of real ones from ABB. The IGBTs have voltage rating of 3300 V and current rating of 1500 A. The voltage rating of the diodes is 4500 V and the current rating is 1650 A. This also gives safety factor for the current of 15 %. The devices will not break down at 1500 A. According to the data sheets they can handle much larger currents for shorter durations. There is also a built in over current protector having the large inductance coil. Data sheets for the devices can be found in Appendix F.

4.2.2 Losses

These loss considerations are based on the theory given in [22]. In an ideal semiconductor the current conduction capabilities are infinite at the same time as the voltage drop is zero. The transition from OFF-state to ON-state happens instantaneously. However these characteristics are not present in the real world, which means there are power losses involved when operating semiconductor devices. The losses in a semiconductor can be divided into two categories. Conduction losses and switching losses. The former arise

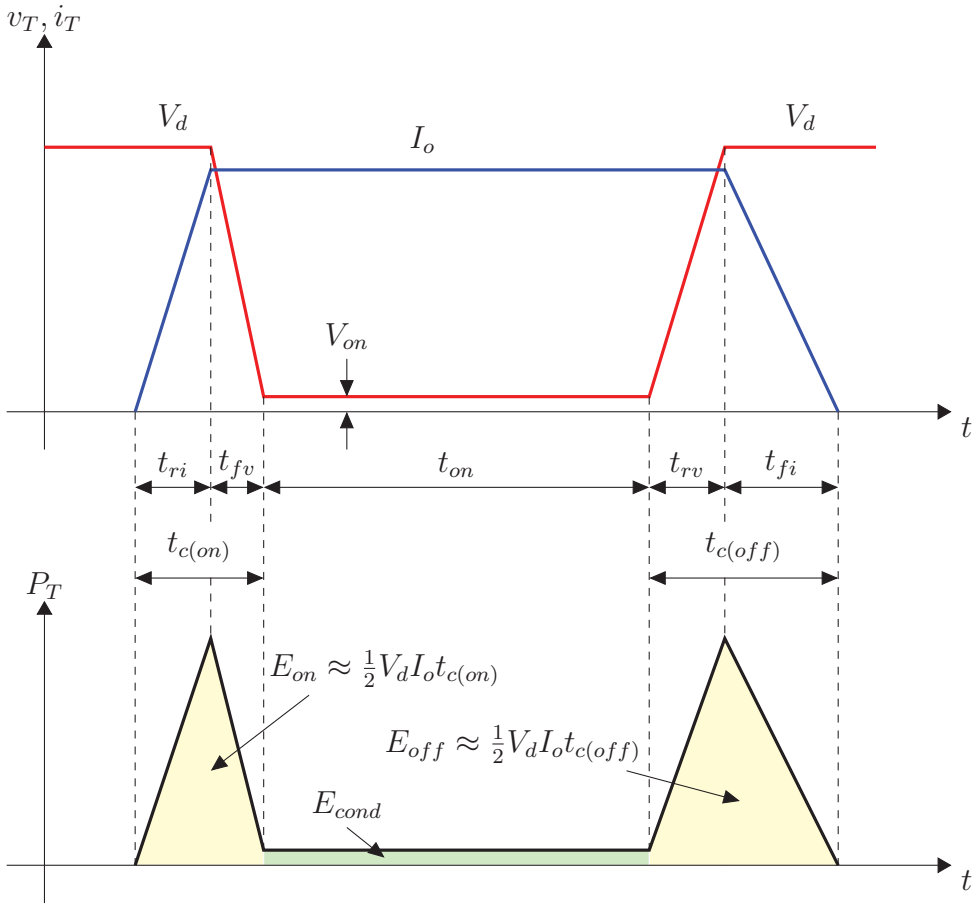

Figure 4.4: The power dissipation in a semiconductor.

because the device has a small on-state voltage. The latter arise because the current does not rise in an instant when the device is turned on, nor does the voltage fall immediately. When switching off, the current does not fall instantaneously and the voltage does not rise in an instant either. Fig. 4.4 shows the principal of losses in a semiconductor which is first switched on, then conducts for a time and then is switched off. V_d is the voltage which the device blocks, I_o is the current conducted when fully on, V_{on} is the on-state voltage. There are some exaggerations in the figure to make the points clearer. The magnitude of V_{on}, which in reality is in the order of a few volts is exaggerated compared with V_d. The length of t_{on} is on the other hand shortened compared to the length of $t_{c(on)}$ and $t_{c(off)}$. The coloured areas correspond to the energies lost during one cycle. The conduction losses are given by Eq. 4.17.

$$P_{on} = V_{on} I_o \tag{4.17}$$

This equation integrated over t_{on}, the green area, E_{cond} in Fig. 4.4 is given. The energies lost in the switching actions correspond to the two yellow areas, E_{on} and E_{off}. These are obtained by integration of P_T during t_{on} and t_{off}. These energies are lost f_s times per second, and the averaged switching losses can be expressed by:

$$P_S = \frac{1}{2} V_d I_o f_s (t_{c(on)} + t_{c(off)}) \tag{4.18}$$

Based on these equations it is desirable to have a low on-state voltage and short switching times. These losses are important when choosing the operating conditions for the converter. The switching frequency which greatly influences the losses will be looked upon in the next section.

4.2.3 Switching frequency selection

The converter will operate on a fixed switching frequency. The value of this will influence on the switching losses in the converter and the harmonic pollution. The higher switching frequency, the higher switching losses, but lower harmonic content. The selection is therefore a compromise between these two factors. The maximum switching frequency is dependent on the minimum pulse width and the temperature on the junction. Guidelines given in [23] are used when considering this.

The maximum theoretical switching frequency is constrained by the turn-on and turn-off switching times and the rise and fall times of the current. These times added up is an estimate of the total switching time, and should not exceed 5 % of the switching period. The intention of this is just that there has to be time for current conduction during a switching period in addition to "lost" time in the switching moments. Each of these times are given in the data sheet in Appendix F. The voltage rise and fall times are ignored in this consideration as they are very short compared to the equivalent times of the current. This identity is given by Eq. 4.19:

$$f_{max1} = \frac{0.05}{t_{d(on)} + t_{d(off)} + t_r + t_f} \tag{4.19}$$

Inserting the values from the the data sheet gives a theoretical maximum switching frequency of 16.8 kHz. This frequency does not take the heat which is created on the junction and the heat which is dissipated from the

junction into consideration. Eq. 4.20 does this, and will in the most cases give a lower switching frequency than Eq. 4.19.

$$f_{max2} = \frac{\frac{T_J - T_C}{R_{\theta JC}} - P_{cond}}{E_{on} + E_{off}} \tag{4.20}$$

The terms in the equation corresponds to the following:

- $\boldsymbol{T_J}$ is the temperature on the junction.
- $\boldsymbol{T_C}$ is the temperature on the case.
- $\boldsymbol{R_{\theta JC}}$ is the thermal resistance of between the junction and the case. The unit of this quantity is K/W This unit can be compared with the ohmic resistance in an electrical circuit which has the unit Ω or V/A In a thermal circuit the temperature difference corresponds to the voltage in its electrical counterpart, and the power represents the current. It describes how much power which is dissipated through the material depending on the temperature difference.
- $\boldsymbol{P_{\mathbf{cond}}}$ is the conduction losses in the IGBT. It is composed by the current through the device, and the voltage drop. $P_{cond} = V_{CE} \times I$.
- $\boldsymbol{E_{\mathbf{on}}}$ is the energy loss when switching ON the IGBT.
- $\boldsymbol{E_{\mathbf{off}}}$ is the energy loss when switching OFF the IGBT.

The last three items in the list was further explained in Sec. 4.2.2. Inserting the data from the data sheet gives the maximum switching frequency 1552 Hz. This frequency is used as a maximum limit, and the best switching frequency below this is chosen based on simulations.

Chapter 5

Control and modulation

5.1 Control system

The objective of the control system is to smooth out the power flow from the generator to the power system. Ideally the combined power output from generator and SMES will be constant. The control unit to maintain this is rather simple and contains only one PI-regulator, see Fig. 5.1. The input to this regulator is the difference between the reference power and the measured power flow to the grid. The reference power is a constant value, set in advance. The PI-regulator is tuned using trial and error, and the output is forwarded into a block which uses so called abc theory to calculate current references [24]. This theory and its employment in the system will be further explained in the next section. The parameters of the PI-regulator are found to be as following:

$$K_{pi,pu} = 0.1$$
$$T_i = 0.01$$

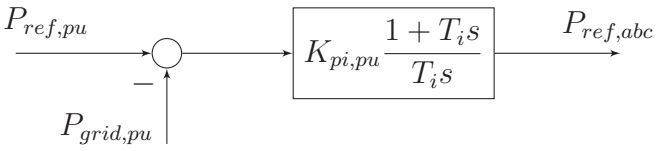

Figure 5.1: The PI power controller.

5.2 ABC theory

The abc theory in this system, also called instantaneous abc theory is used to construct the reference currents for the modulation. The abc theory is generally used to compensate for reactive power. However in this system it is used for compensating active power. The concept of the theory will first be explained as it is stated in [24]. Then its implementation in this system will be explained.

The idea of the abc theory is to determine the active part of a total load current which has both active and reactive components, or active and nonactive current as the terminology is in [24]. The goal is to deliver the same amount of energy from the source to the load, without having to transport reactive power on the lines. The method of doing this is to establish a minimized, instantaneous active current component which fulfil the energy constrain mentioned. The difference between this new minimized active current and the uncompensated load current is the nonactive current which now comes from a type of compensator, as seen in Fig. 5.2. The determination of the instantaneous active current is carried out using e.g. the Lagrange Multiplier Method. The objective of this method is to find the extreme values of a function whose domain is constrained to lie within some particular boundaries [25]. The active, i_{pf}, and nonactive, i_{qf}, currents of any given load current, i_k are given by the following equation:

$$i_f = i_{pf} + i_{qf}, \qquad f = (a, b, c) \tag{5.1}$$

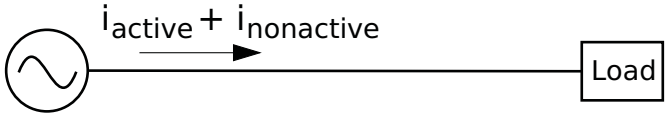

(a) Uncompensated currents.

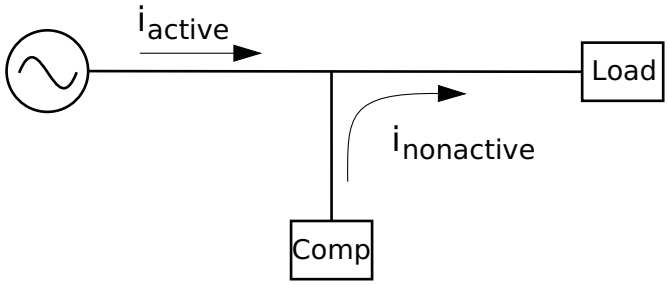

(b) Compensated currents.

Figure 5.2: The concept of active and nonactive currents.

The goal is to minimize the load current, and the constraint is that the nonactive current components i_{qa}, i_{qb} and i_{qc} do not generate any three-phase instantaneous active power. The minimization of the load current will of course be $-\infty$, but as this is a invalid and uninteresting solution the function which is interesting to find the minimum of is given by:

$$L(i_{qa}, i_{qb}, i_{qc}) = (i_a - i_{qa})^2 + (i_b - i_{qb})^2 + (i_c - i_{qc})^2 \tag{5.2}$$

This will minimize the absolute value of the active load currents i_{pf}. The constraint is given by:

$$h(i_{qa}, i_{qb}, i_{qc}) = v_a i_{qa} + v_b i_{qb} + v_c i_{qc} = 0 \tag{5.3}$$

Eq. 5.4 gives the method of the Lagrange multiplier, where λ is the Lagrange multiplier:

$$\nabla h = \lambda \nabla g \tag{5.4}$$

Eq. 5.4 is applied to Eq. 5.2 and Eq. 5.3 which gives a set of three equations:

$$\begin{aligned} -2(i_a - i_{qa}) &= \lambda v_a \\ -2(i_b - i_{qb}) &= \lambda v_b \\ -2(i_c - i_{qc}) &= \lambda v_c \end{aligned} \tag{5.5}$$

Rewritten this gives the following system of equations:

$$\begin{aligned} 2i_a - \lambda v_a &= 2i_{qa} \\ 2i_b - \lambda v_b &= 2i_{qb} \\ 2i_c - \lambda v_c &= 2i_{qc} \\ v_a i_a + v_b i_b + v_c i_c &= 0 \end{aligned} \tag{5.6}$$

Eq. 5.6 is solved for λ:

$$\lambda = \frac{2(v_a i_{qa} + v_b i_{qb} + v_c i_{qc})}{v_a^2 + v_b^2 + v_c^2} = \frac{2P_{3\phi}}{v_a^2 + v_b^2 + v_c^2} \tag{5.7}$$

Eq. 5.7 is inserted into Eq. 5.6 and the following is achieved on vector form:

$$\begin{bmatrix} i_{qa} \\ i_{qb} \\ i_{qc} \end{bmatrix} = \begin{bmatrix} i_a \\ i_b \\ i_c \end{bmatrix} - \frac{P_{3\phi}}{v_a^2 + v_b^2 + v_c^2} \begin{bmatrix} v_a \\ v_b \\ v_c \end{bmatrix} \tag{5.8}$$

The last term in Eq. 5.8 corresponds to the active part of the total load current in Eq. 5.1. Because of the constraint given on the minimization the

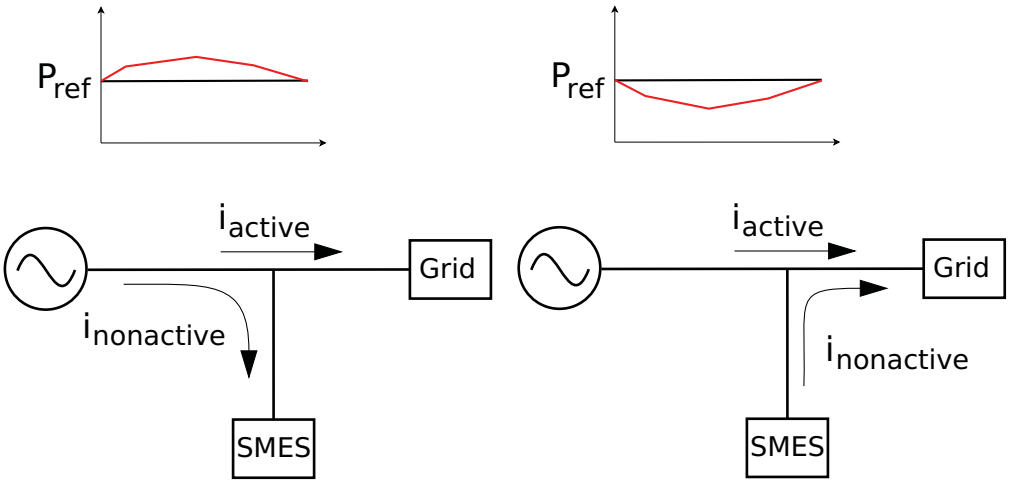

(a) Positive power fluctuation. (b) Negative power fluctuation.

Figure 5.3: The different flow directions of current into the SMES.

active currents in Eq. 5.8 will deliver the same amount of instantaneous active power to the load as the original load currents. This is expressed as:

$$P_{3\phi} = v_a i_a + v_b i_b + v_c i_c = v_a i_{pa} + v_b i_{pb} + v_c i_{pc} \tag{5.9}$$

So how can this theory be applied to the SMES power conditioner? The idea is that the current from the induction generator also consists of an active and nonactive part. These do not correspond to active and reactive power, but reference power and power fluctuations. The reference power is the power generation from the generator set according to predictions of wind speed, and the power fluctuations arise according to wind speed fluctuations around the reference wind speed. The active part of the current gives the reference power, and the nonactive gives the power fluctuations. This can be expressed by the following principal equations:

$$\begin{aligned} i_{active} &= \frac{P_{reference}}{V} = i_{reference} \\ i_{nonactive} &= \frac{P_{fluctuations}}{V} = i_{fluctuations} \end{aligned} \tag{5.10}$$

The meaning of this is that the SMES will supply the nonactive current. If the power fluctuation is positive the sum of the active and nonactive current components will be larger than the reference current, and the opposite if the power fluctuation is negative. The concept is shown in Fig. 5.3. A

vital detail is that the nonactive current can flow in both directions. What distinguish this from the conventional abc theory is of course that it is used for compensating active power. However reactive power fluctuations will also be included in this compensation as it is part of both the reference current and the fluctuating currents. This is a drawback of this control system as it is not possible to compensate for active and reactive power separately. Another control strategy could be to implement the pq-theory, which enables this feature.

The output from the abc block in the control system is three phase current references which correspond to the left side of Eq. 5.8. These currents are transformed to a current space vector having an angle θ. A ratio between the space vector and the DC-current is then calculated in per unit. This is called the modulation factor m and is forwarded into the modulation block which generates signals for the self commutating semiconductors in the converter. The modulation technique is explained in the next section.

5.3 Space vector modulation

The number of research projects involving voltage source converters (VSC) is as mentioned much higher than for current source converters (CSC) [26]. Because of this the different modulation and control techniques for CSC is not as well known as for its counterpart. The space vector modulation (SVM) used in this thesis is based on the modulation strategy for a VSC.

In a converter there are only a limited number of possible switch combinations. For a VSC there are eight, and in a CSC there are nine. The different switch combinations are shown in Fig. 5.4. Three of them (SC7, SC8 and SC9) give a short circuit of the DC-current. Each of the switch combinations forms space vectors in the complex dq-plane. The three short circuit combinations give zero vectors. The other six give stationary vectors. This is illustrated in Fig. 5.5. Each of the stationary space vectors encloses a sector together with the nearest space vector. It is readable from Fig. 5.5 that the space vector $\vec{i_s}$ in sector I can be made by adding $\vec{i_{ac}}$, $\vec{i_{bc}}$ and a zero vector. This is the concept of SVM. The space vector $\vec{i_s}$ is a transformation of the currents in the three phase input to the converter. It rotates anti-clockwise at a rotational speed equal to the frequency in the network. The space vector is derived from the current equations for a three phase balanced

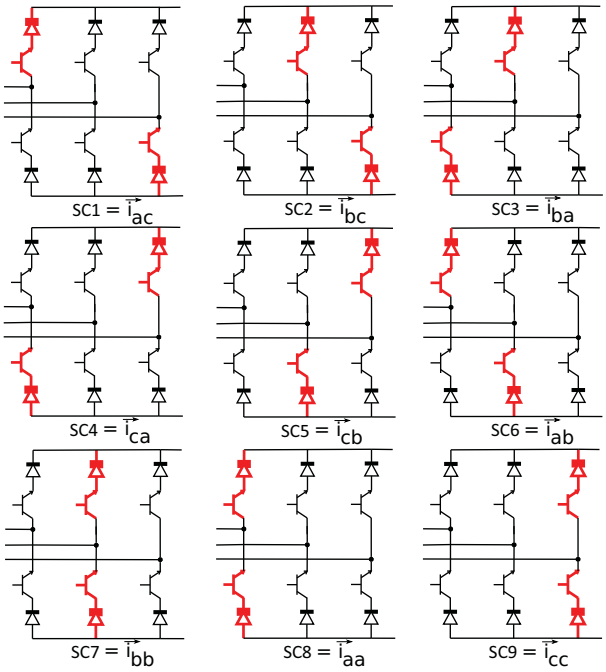

Figure 5.4: The different switch combinations.

system having a frequency of ω and a phase shift of ϕ [27]:

$$\begin{aligned} i_a &= I_m cos(\omega t + \phi) \\ i_b &= I_m cos(\omega t + \phi - 2\pi/3) \\ i_c &= I_m cos(\omega t + \phi + 2\pi/3) \end{aligned} \tag{5.11}$$

The current space vector $\vec{i_S}$ is then given by:

$$\vec{i_S} = \frac{2}{3}(i_a + i_b e^{j2\pi/3} + i_c e^{j4\pi/3}) \tag{5.12}$$

By using trigonometric identities and Euler's formula [28], and inserting Eq. 5.11 into Eq. 5.12 the expression for the current space vector becomes:

$$\vec{i_S} = I_m e^{j(\omega t + \phi)} \tag{5.13}$$

Eq. 5.13 shows that the space vector rotates at the frequency of the network, and at a phase delay equal to ϕ. Compared to the current on the DC-side the magnitude of the space vector can be calculated by simple considerations. For instance the space vector $\vec{i_{ac}}$ is formed by the switch combination SC1 in Fig. 5.4. This state implies that the current in phase a, $i_a(t)$, defined positive

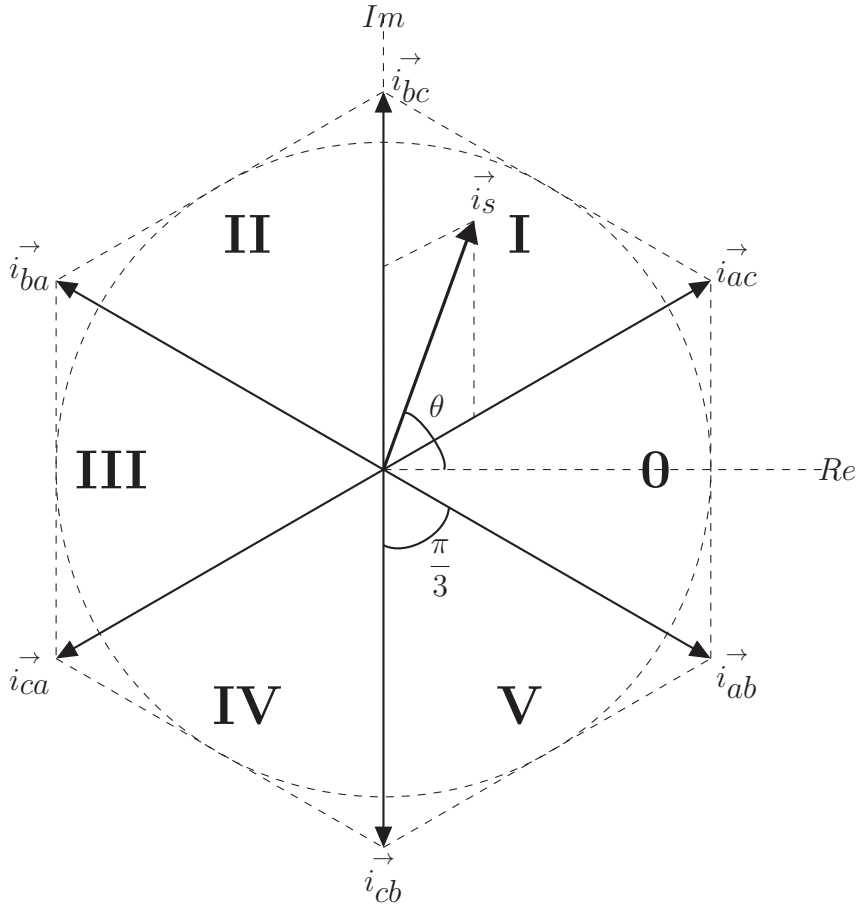

Figure 5.5: Space vector states for current source converter.

into the converter equals the DC-current i_{dc}, and the current in phase c, $i_c(t)$ equals $-i_{dc}$. None of the switches in leg B is connected, hence the current in phase b is zero. This is put into Eq. 5.12, and $\vec{i_{ac}}$ equals:

$$\vec{i_{ac}} = \frac{2}{3}(i_{dc} + 0e^{j2\pi/3} - i_{dc}e^{j4\pi/3}) = \frac{2}{3}i_{dc}(1 - e^{j4\pi/3}) = \frac{2}{\sqrt{3}}i_{dc}e^{j\pi/6} \qquad (5.14)$$

The wanted space vector is formed by applying the enclosing fixed space vectors for fractions of a switching period, T_s. Depending on the size of $\vec{i_S}$ a zero vector must also be applied. The desired space vector must be within the limits of the straight lines drawn between the tips of the adjacent fixed vectors in Fig. 5.5. However it is advantageous that the space vector has constant length, or at least not a maximum value depending on where it is. Hence the circle spanned within the limits of these lines defines the maximum space vector magnitude.

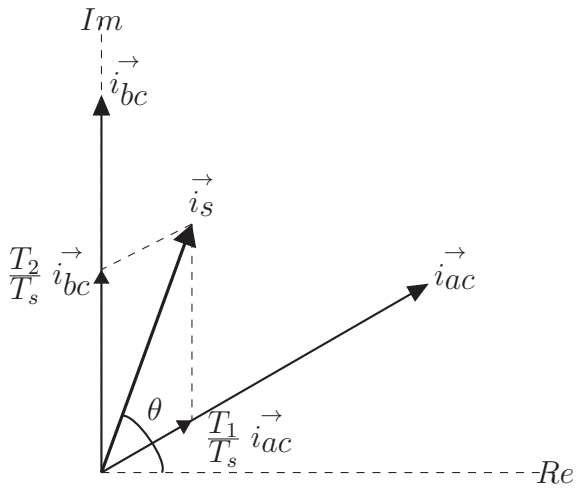

Figure 5.6: The calculation of switch times.

$\vec{i_S}$ in Fig. 5.5 is composed of $\vec{i_{ac}}$, $\vec{i_{bc}}$ and $\vec{i_{cc}}$. To calculate how long time each fixed vector must be applied to create $\vec{i_S}$ a method from [29] is used. Fig. 5.7a illustrates the principle of time intervals. It is readable that $\vec{i_{ac}}$ has to be applied for $\frac{T1}{T_s}$ and $\vec{i_{bc}}$ for $\frac{T2}{T_s}$ to create the space vector. A zero vector must also be applied unless the desired space vector is equal to the maximum space vector. The time intervals are calculated considering SVM for VSC which sectors are shifted $\frac{\pi}{6}$ in the clockwise direction compared to a CSC. Therefore it is a term of $\frac{\pi}{6}$ in the equations to rotate back again:

$$T_1 = T_s \frac{I_m sin(\frac{\pi}{3} - (\theta + \frac{\pi}{6})) - S\frac{\pi}{3}}{i_{dc}} \tag{5.15}$$

$$T_2 = T_s \frac{I_m sin((\theta + \frac{\pi}{6})) - S\frac{\pi}{3}}{i_{dc}} \tag{5.16}$$

The mentioned zero vector time interval is then given as the time rest in the switching interval:

$$T_z = T_s - T_1 - T_2 \tag{5.17}$$

The above equations are valid for all sectors. The last term in the numerator of Eq. 5.15 and Eq. 5.16 is rotating the angle back to sector 0. S corresponds to the sector the space vector is in. The reason for this term is that the space vector angle, θ, is measured from the real axis. Having the rotating term allows the same equations being used for every sector. The ratio $\frac{I_m}{i_{dc}}$ in

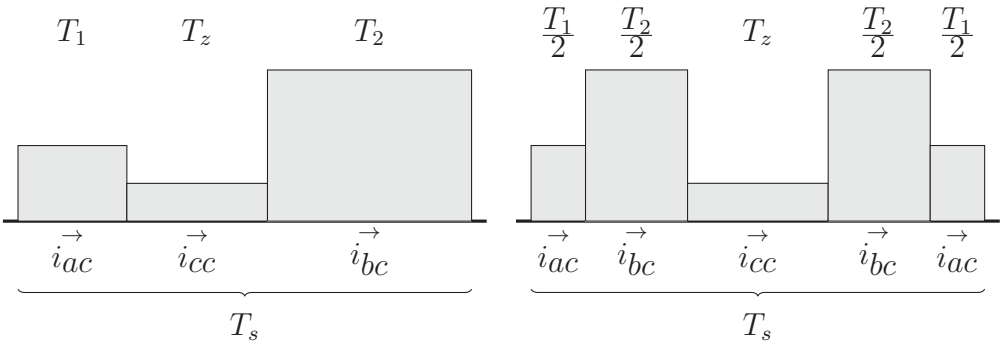

(a) The distribution of switching states.

(b) The distribution of switching states in a symmetrical modulation pattern.

Figure 5.7: The switching pattern to create $\vec{i}_S$ in one switching period for two different patterns.

the equations is the modulation factor, m, which is taken as input from the control system. This can attain values between 0 and 1. Above 1 there is overmodulation. This should be avoided as it will not give the desired space vector as the entire switching period is employed before the space vector is formed. The distribution of the switch states to create $\vec{i}_S$ in Fig. 5.5 is illustrated in Fig. 5.7a. This type of distribution is not the only one possible to create the wanted space vector. The sequence of the applied vectors is not affecting the created space vector. There are numerous considerations:

- Which zero vector is the best to apply?
- When should the zero vector be applied?
- In which sequence should the fixed space vectors be applied?
- How many times each switching period should each vector be applied?

The first item is fairly easy to decide. In the example here, the two active vectors creating $\vec{i}_S$ both involved the lower half-leg of leg C being ON. Considering this the zero vector also employing this half-leg being ON would be preferable. This would lead to a minimum amount of switching, as only two switches will change its state between the transition from active vector to zero-vector. This applies of course to the other sectors as well.

When it comes to the second item there is no set answer to this. One very small advantage of placing the zero vector in the middle of the switching pattern as in Fig. 5.7a is present. This pattern entails that the last active

vector before a sector change will be the first active vector in the new sector. As this is the case, there is no need for switching during sector changes. This will decrease the switching losses by a fraction, but considering the sectors only change six times in a cycle compared to the switching frequency in the kHz −area the advantage of this switching pattern is almost neglectable.

The third item has the same argument as the previous item. The only time it matters is at the sector changes, and these are not very often compared to the switching frequency.

The last item refers to the fact that each of the vectors can be applied several times during one switching period. Check Fig. 5.7b for illustration of this switching pattern, which applies the two active vectors two times. The switching states in the two different cases will produce the same vector as the applied vectors are ON at equal amounts of time in total. The symmetrical switching pattern is said to have less harmonic pollution than its non symmetrical counterpart [30]. Although this did not give any significant result in the simulations here. Besides, this switching pattern has higher switching losses due to the fact that it actually switches twice as often as the simpler pattern. Because of this, the symmetrical pattern has been abandoned in this thesis, and the pattern shown in Fig. 5.7a is used.

5.4 Principle of operation

The SMES coil in this system works as an active power compensator. When the output power from the generator is higher than a preset reference value, the SMES coil will absorb the extra power and store it in the magnetic field. This can be called Mode 1. The reference in this system is fixed, but in a real system the reference power can be set by predicting the future wind conditions on site, and thereby predicting the output power from the generator. The time span of this prediction cannot be too long as the wind speed is hard to foresee. Mode 2 applies when the power from the generator equals the reference power. In this mode the energy in the SMES will be stored in almost lossless conditions. However there are losses in the semiconductors in the converter. For longer time intervals in this mode, a superconducting bypass path would be preferable. A path like this would be slower to operate than the IGBTs in the converter and the response time of the converter would be increased. On the other hand the usage of this path would be rare as the output from a wind turbine is seldom constant for long. Mode 3 is when the power output from the generator is less than the power reference. In this mode, the SMES will deliver power to the network. Here it will be explained how these modes of operation are achieved.

The error signal for the PI power regulator is the difference between the power reference and the actual power delivered to the network. The output of the regulator is then forwarded into the ABC-block. Here it is used to calculate three phase reference currents. These are transformed to a rotating space vector, which is scaled with the DC-current and the modulation ratio is obtained. This ratio together with the space vector angle and switching frequency is passed into the modulation. This block gives the gating signals to the IGBTs.

Chapter 6

Simulation and results

The power system in Fig. 4.1 has been simulated using the software PSIM. The simulation model and the code for the modulation can be found in appendix D and appendix E. Due to a misunderstanding, the proper model was not received before more than half of the project time had passed. This has limited the testing, and confined the results which are achieved.

6.1 Simulation setup

The induction generator is started for each simulation. This start-up period generates some transients in the power output from the generator and it both draws and delivers active power before it settles at a constant level. During the first 1.3 seconds, the converter works as a diode rectifier. The reason for doing this is that the superconducting coil is being charged at the same time as the start-up of the generator. During this time interval the network together with the generator supplies power to the SMES. In the diode rectifier mode, the control system is disconnected and all of the controllable switches are constant ON. This ensures a fast charging of the coil as it is subjected to the peaks of the line voltages in a six-pulse manner. Because the applied voltage is always positive the current is increasing during the entire time interval. Fig. 6.1 shows the voltage across the superconductor during this charging. The average value of the voltage is 1574 V. This ensures a current ramp rate of: $\frac{di}{dt} = \frac{V}{L} = 874$ A/s. The diode operation also ensures that the control system do not try to compensate for the big power oscillations in the start-up. The response in these 1.3 seconds has not been considered important for the study of the system response.

Losses in the converter are also analyzed. This is done using the built in feature in PSIM called Thermal module. Using this tool a semiconductor

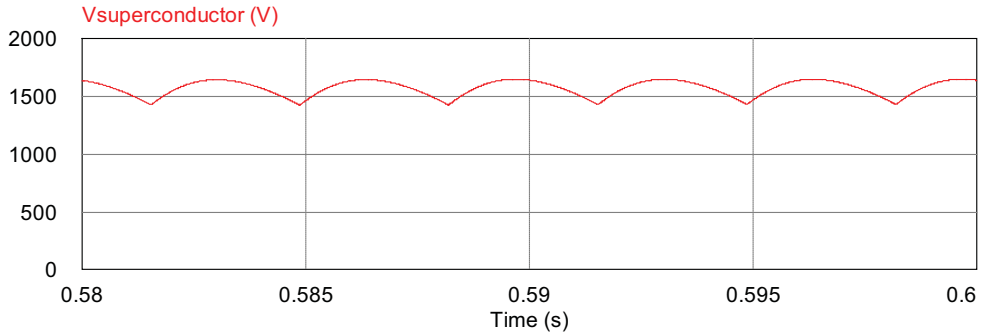

Figure 6.1: The voltage on the superconductor during one 50 Hz-cycle in the charging period.

device is given the characteristics of a real switch when it comes to losses. The conduction and switching losses are obtained for both the diode and the IGBT. Regarding the IGBT, both the IGBT part and the anti parallel diode give are measured, but the anti parallel diode is not loaded and its contribution to the losses are near zero.

The simulations which have been done demonstrate the capability of the coil to operate as an active power compensator. Different cases have been simulated to show the capabilities and constraints of the SMES system. The rated wind speed is 12 m/s, and the power output varies according to Fig. 6.2. It is readable that the simulated power-output is less than for an ideal curve which is created from the physical relation given in Eq. 2.1, and multiplied by a Betz factor of 0.59. The rotor area and the air density give the same power output as PSIM for 12 m/s. The reason for the deviation is partly that PSIM in its manual refers to a maximum Betz limit of 0.49 [31]. As mentioned in Chapter 2 the maximum is 0.59. This points out an error in the manual, but whether or not this is implemented in the software as well is unknown. This can be one small reason for the bias, but it does not explain the shape of the curve which does not correspond to a third power function. However the shape is not very important owing to the fact that the essential aspect is that there are variations in power output when variations in wind speed occur.

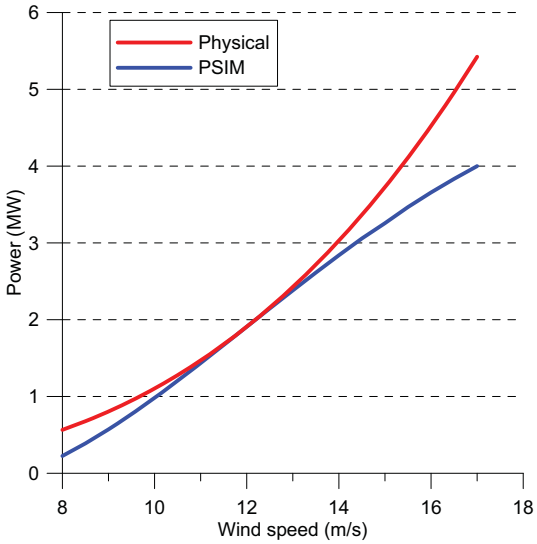

Figure 6.2: The power versus wind speed curves of the ideal physical model and the PSIM model.

6.2 Results

6.2.1 Linearly changing wind speed

Fig. 6.3 shows the power output from the generator, and the power flow into the grid. In the simulation run, the converter is not put into the compensating mode until 1.3 s has passed. The sequence of events is given below in Table 6.1. As can be seen the fluctuations in the start-up period is quite large. The power output settles at around 1.3 s. It is evident compared to Table 6.1 that there is a delay in the power output after the wind speed has changed. This is readable both at the decrease of wind speed, and increase. The delay is about 0.2 s. The reason for this is a small delay in the mechanical system. The torque changes on the wind turbine are not instantaneously transferred to the induction generator.

Table 6.1: The sequence of events when wind speed changes linearly.

Time (s)	*Event*
0.0	System starts up. Diode rectifier charge mode starts. Wind speed is 12 m/s.
1.3	SMES compensating starts.
1.5	Wind speed drops, and power generation decreases.
3.0	Wind speed rises, and power generation increases.

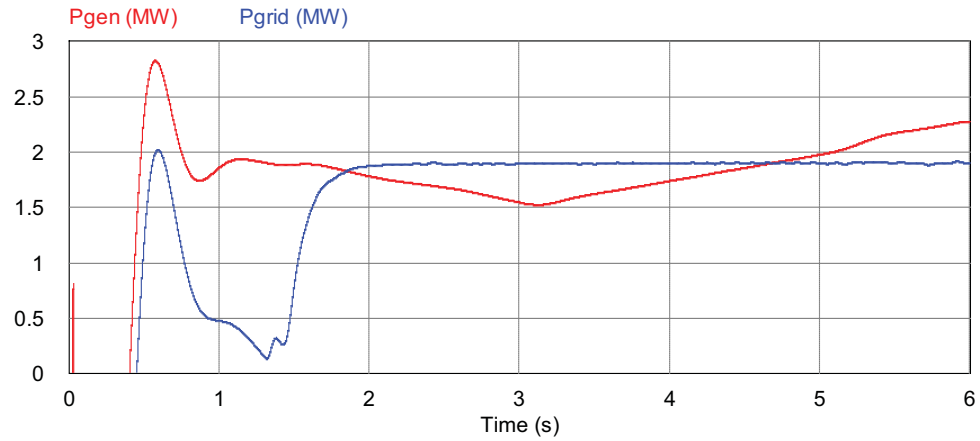

Figure 6.3: The power output from the generator and power delivered to the grid.

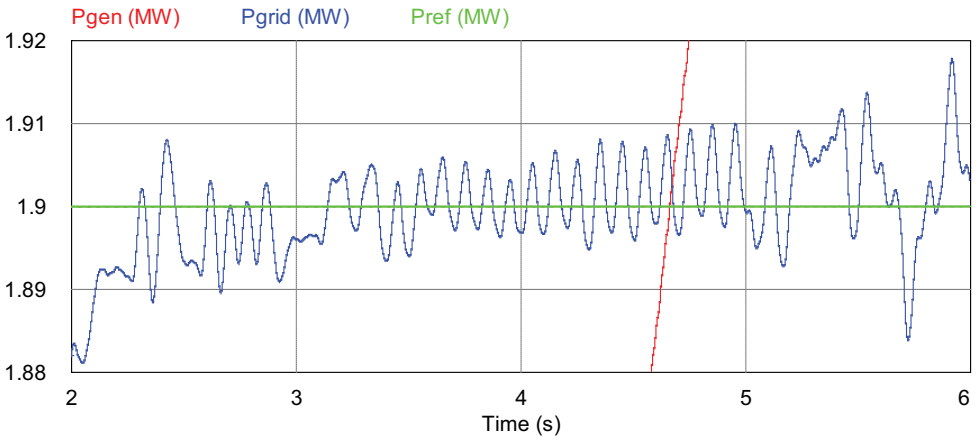

Figure 6.4: Zoom of the power delivered to the grid.

It is clear that the SMES-unit stabilizes the power output to the grid. Even though the generator output falls to 1.53 MW the output to the grid has an average from 2.2 s to the end of simulation equal to the reference of 1.9 MW. The power output from the generator increasing above the reference does not change this. Fig. 6.4 shows a zoom of the power delivered to the grid. There is ripple present in the power delivered, however this is small compared to the magnitude of the power. In percentage of the reference power the ripple is only around $\pm 0.6\%$. Fig. 6.4 does also show how steep the change in the generator power is and that the power delivered to the grid is not affected by this. The ripple in the grid power does not have constant magnitude. The reason for this can be that the power which must be compensated for is

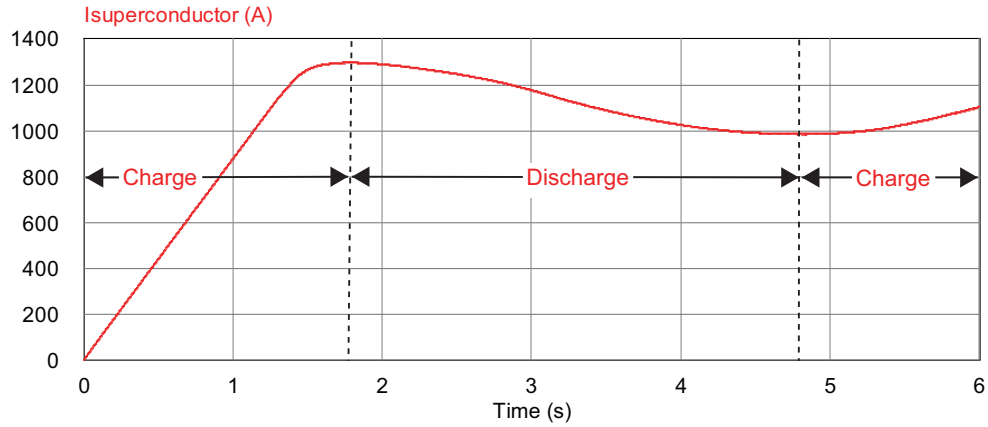

Figure 6.5: Current in superconducting coil.

not constant, and the control system does not manage to compensate quick enough. The current in the coil during this line of events is shown in Fig. 6.5. The first period shows the charging. The coil continues to charge for a while after the diode rectifier mode is finished. The reason for this is that the generator power not has reached the reference power yet. It even continues to charge after the power output from the generator decreases. However this is still in the start-up period, and is not representative for the rest of the operation. When the generator power crosses the reference power again, the SMES current hits its minimum. Then a new charging period begins, this time operating with the switches controlling the current flow. This results in a much slower charging than in the first period, but the charging is now controlled. Fig. 6.6 shows a zoom of the coil current during this charging period. The voltage applied is also showed. As is readable the current both increase, decrease and constant during the small time interval. The voltage is switched between the different line voltages, and depending on the value of these the current is changing. In interval ”a” the current increases due to the applied positive voltage. In interval ”b” the current decrease, due to the negative voltage, and in interval ”c” the current is constant because of zero voltage. Although the applied voltage is changing during the whole interval it is positive on average. The average value is 160.1 V. Due to measurements the current is found to have an average increase rate during this interval of 86.02 A/s. Meaning $\frac{di}{dt} = 86.02$. This should equal $\frac{V}{L}$ in an ideal lossless circuit. However because of the small resistance in the IGBT and diode, this is not the case here. According to only the voltage and inductance, the current increase should be 88.94 A/s. When discharging the average voltage will be negative. The SMES power demand will determine the magnitude of

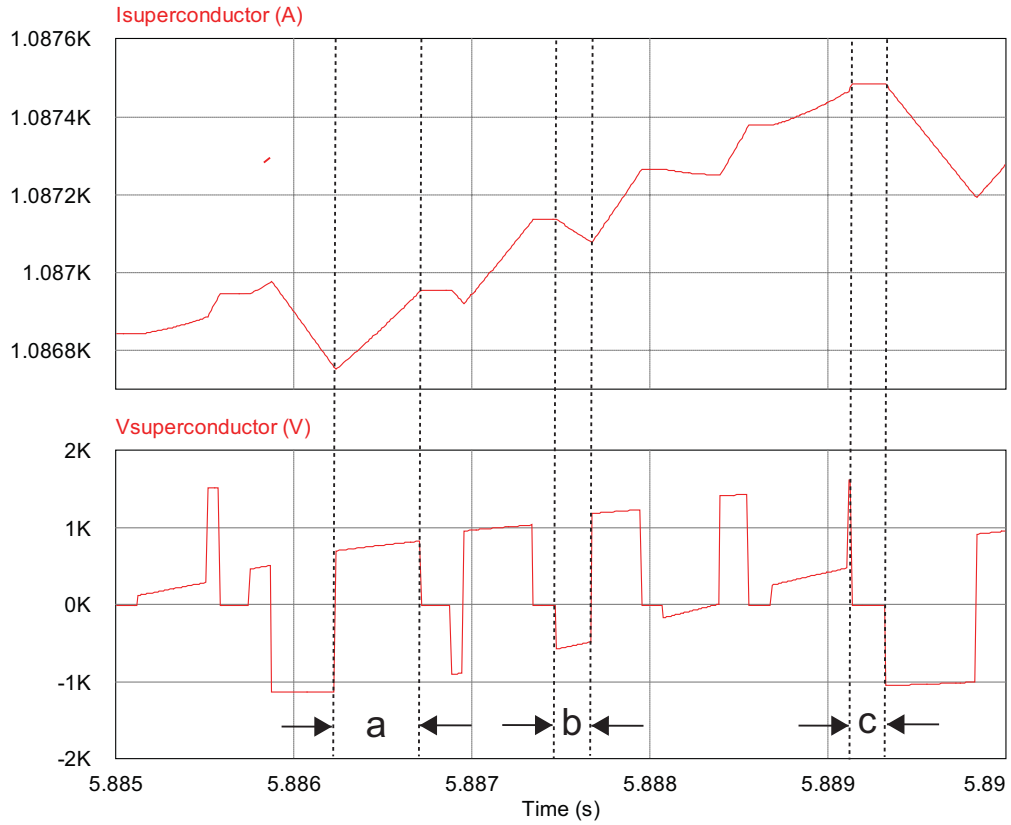

Figure 6.6: Current and voltage in superconducting coil during charge.

this average voltage value. The voltage in Fig. 6.6 illustrates the statement in Section 4.2.1 that the converter is subjected to AC-voltage. However the current is DC.

The switching pattern during the same time interval is shown in Fig. 6.7. The magnitude of the switch signals are scaled to make the figure easier to read. Value equal to zero means OFF and magnitude larger than zero corresponds to ON. The switch on the upper half-leg of leg B (positive) is on for a long share of the total time interval. From this the sector where the space vector is can be found. Sector II is the sector which is covered by the positive B, and the other switches on the lower half-leg. At the ends of sector II it can be seen that there is a overlap as described in section 5.3. Meaning that the first space vector in sector II is the first in sector I, and the last in sector II is the first in sector III. This shows the distribution of switching times in practice. The uneven distribution of the the BP-CN and BP-AN switch combinations shows that the modulation index (M) is changing through the time interval, which correspond good with the fact

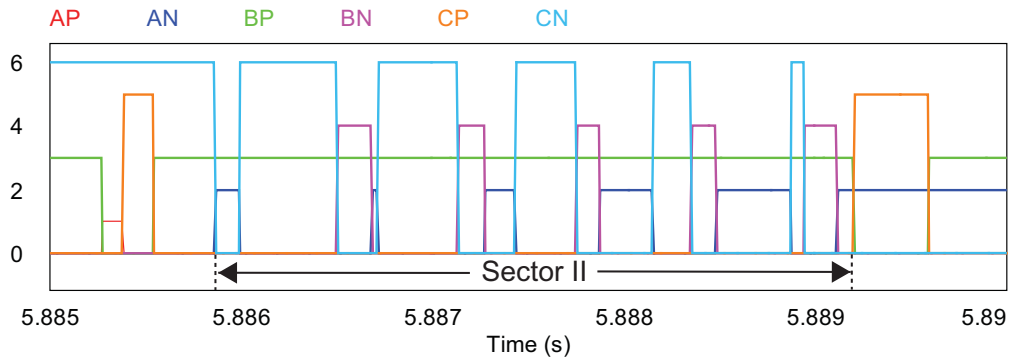

Figure 6.7: Switch pattern.

that the power from the generator is increasing. These switch combinations would have been equal if M had been constant.

The losses in the converter are important to judge on its performance. Figures showing the losses follow below. The losses are not the instantaneous losses, but averaged on 50 Hz-cycle. The jagged shape of the switching loss curves is present because of this averaging, and the fact that the switching does not follow the exact same pattern from cycle to cycle. The switching losses in the first 1.3 s are of course zero. The conduction losses increase during this charging period as these are dependent on the current through the device and have the same shape as the current in the superconducting coil through the simulation. The conduction losses in both of the devices are nearly identical. The reason for this is simply that the on state voltage for the currents conducted here are nearly equal for the two devices. The switching losses are nearly equal as well, the IGBTs having slightly better performance. One way to calculate the efficiency in the converter is by the following formula which takes the power flow into consideration.

$$\eta_{power} = \frac{|Power| - P_{Losses}}{|Power|} \tag{6.1}$$

The meaning of this equation is that the absolute value of the power in the converter subtracted the losses, divided by the absolute power in the converter gives the percentage of power which is not lost. Fig. 6.9 shows a plot of the power in the SMES and the efficiency calculated by Eq. 6.1. The efficiency performance is very dependent on the power. The highest efficiency is gained when the converter delivers or absorbs most power. The efficiency drops to zero when the power flow in the SMES changes direction. However this type of definition might seem a bit unfair as the intention of the converter is not delivering power nor absorbing power and the current will

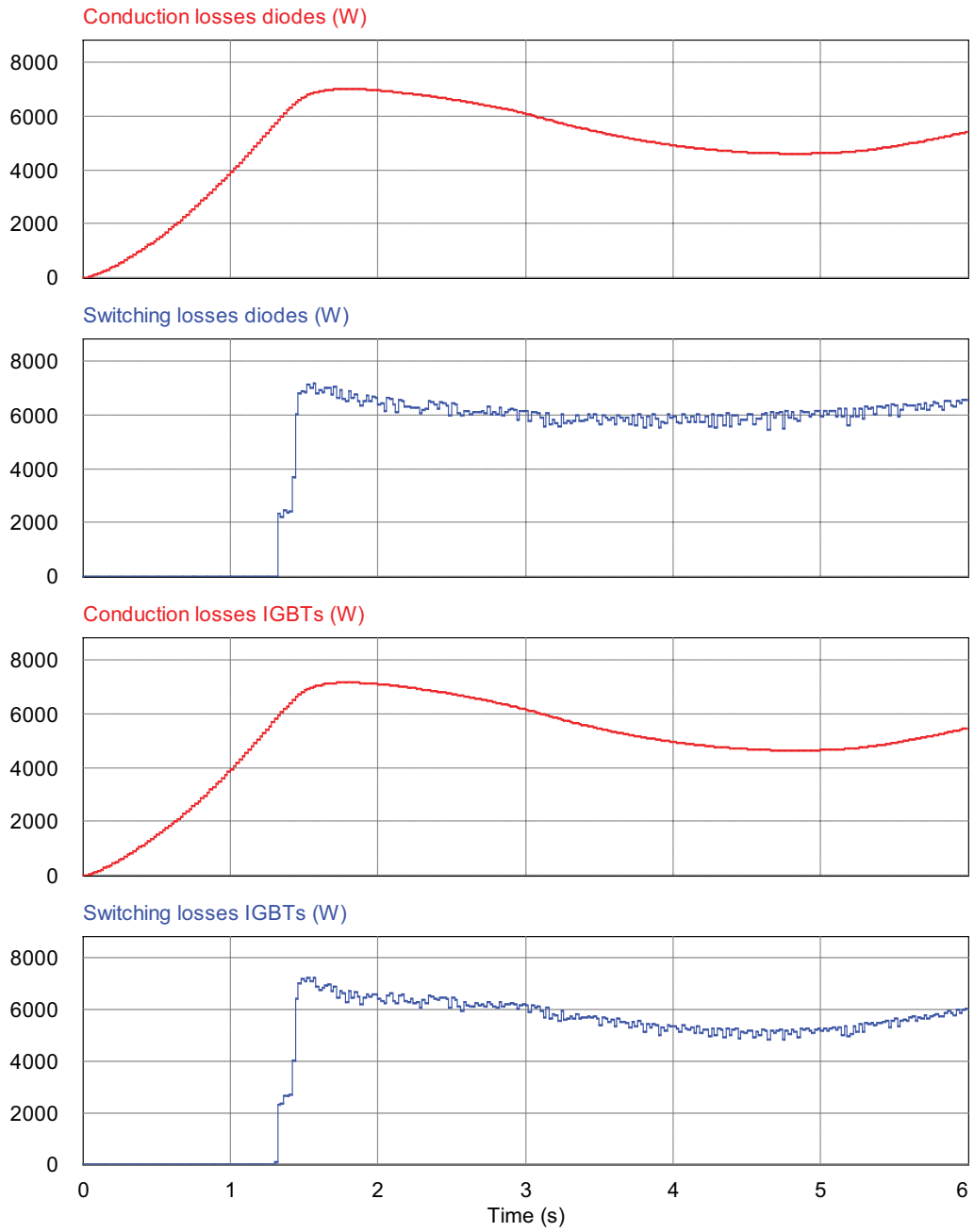

Figure 6.8: The losses in the semiconductors.

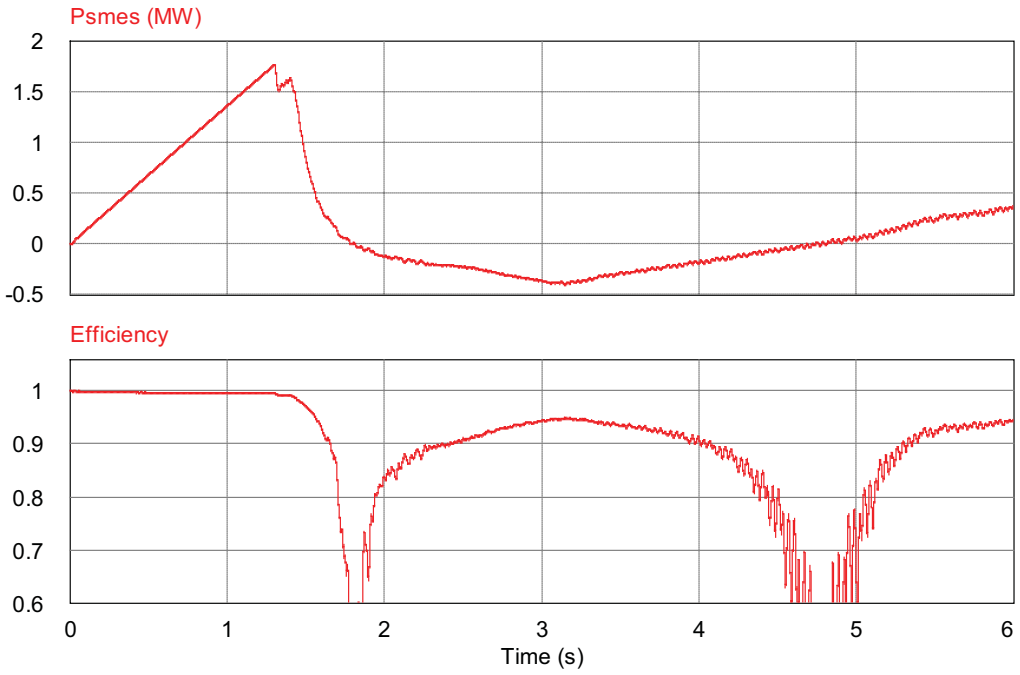

Figure 6.9: The power in the SMES and the efficiency.

have to flow through the semiconductors anyway. In fact the efficiency is also dependent on how much current which is conducted. The higher current, the higher are the losses. Based on this the efficiency should maybe be calculated on different terms, or at least another type of efficiency should be defined. This is done by taking the energy in the converter system into consideration. Because the SMES is an energy storage system, it is interesting to study how much energy which is lost. The total losses are then integrated for one 50 Hz-cycle. The energy stored in the coil is calculated by the formula:

$$E_{SMES} = \frac{1}{2} L I_{SMES}^2 \tag{6.2}$$

The efficiency with regard to the energy is then given by:

$$\eta_{energy} = \frac{E_{SMES} - E_{Losses}}{E_{SMES}} \tag{6.3}$$

The results of this energy efficiency consideration are shown in Fig. 6.10 together with the energy stored in the SMES. The efficiency calculated this way is much better than for the power consideration, and shows that the energy storage has very good performance in this type of operation. Although the energy losses seem small they would rather quickly empty the coil if no

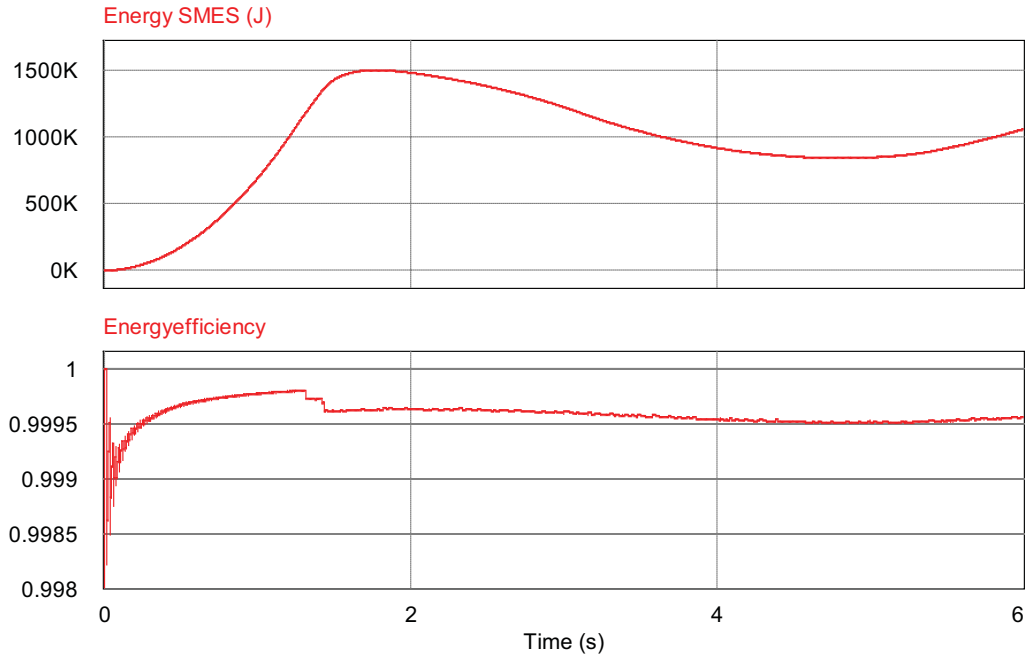

Figure 6.10: The energy in the SMES and the energy efficiency.

energy were to be supplied. A long term storage is therefore not possible using this typology. In a real system the energy used for cooling the coil must also be regarded. This will decrease the efficiency but not by much regarding to the energy. The energy needed for cooling is small compared to the energy stored in the coil. According to [32], a SMES unit at a LCD TV plant in Japan was having a stored energy capacity of 7.34 MJ. The refrigerator power was 40.5 kW, which correspond to 810 J in one cycle. This is only a fraction of 0.011 % of the maximum stored energy. A similar ratio in the system studied here would give an energy loss of 165 J per cycle. Accordingly this would not influence the efficiency much. The efficiency according to Eq. 6.1 would be more affected by the inclusion of the refrigerator power.

6.2.1.1 Output currents and switching frequency

The output currents from the converter are heavily distorted due to the switching of the continuous DC-current. These are shown in Fig. 6.11. To extract the fundamental frequency of 50 Hz the current needs filtering. This is done by a simple LC-filter, having a capacitor connected from each phase and to a grounded star point. The transformer represents the inductance in the filter. The desired cut off frequency of a low pass passive filter is given

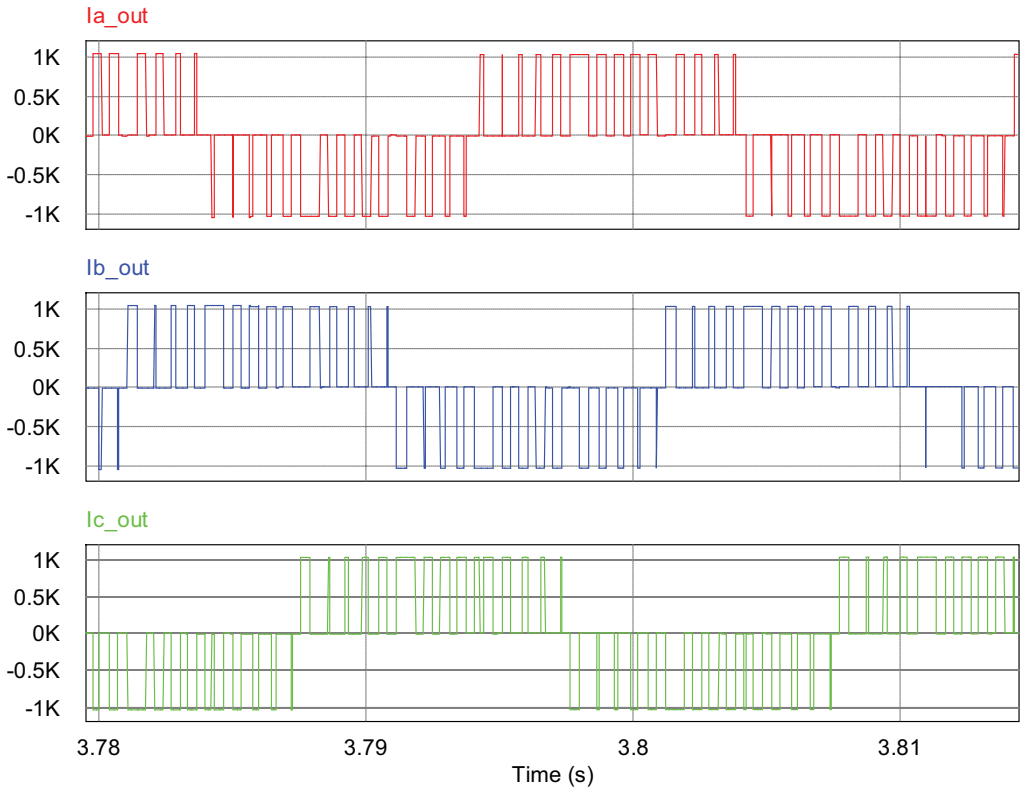

Figure 6.11: The currents from the converter.

by the identity [27]:

$$f_{cutoff} = \frac{1}{2\pi\sqrt{LC}} \tag{6.4}$$

[27] also states that the filter cut-off frequency should be chosen one decade lower than the lowest switching frequency. However tuning the filter like this did not give any good results at all. Because of that the tuning was based on trial and error around the output of Eq. 6.4. The switching frequency selected was based on the theory in Section 4.2.3, studies of output currents after the filter and the power oscillations in the power delivered to the grid. The maximum frequency was 1.5 kHz. In the interval between this maximum frequency and 1 kHz, 1.4 kHz was found to give the best output currents and grid power. A comparison between the different switching frequencies and their responses can be found in Appendix C. The output current after the filter for the switching frequency of 1.4 kHz is given in Fig. 6.12. The currents are still distorted after the filter. This is of course not an ideal situation. This can cause resonances, overheating and equipment maloperation. A solution to this problem could have been an active filter. This could have compensated

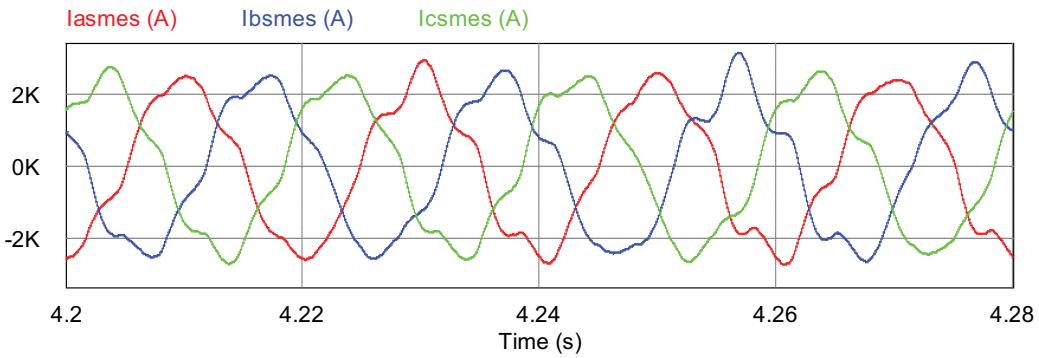

Figure 6.12: The currents after the filter.

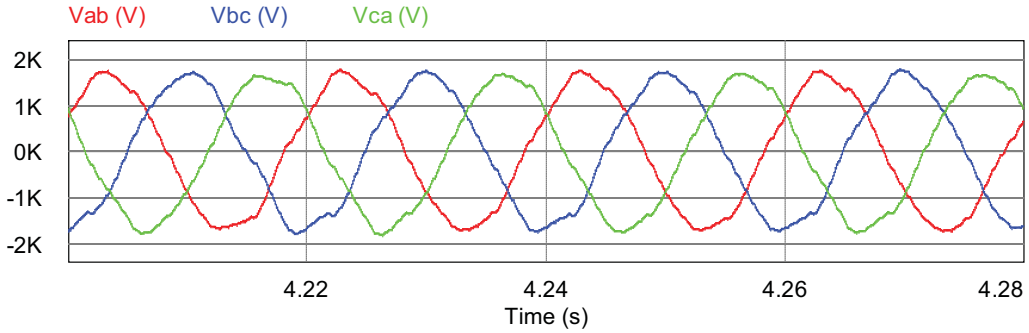

Figure 6.13: The line to line voltages at the converter terminals.

for the harmonics in a more flexible way. The active filter is possible to tune for a much wider spectrum than its passive counterpart. It is also possible to be more selective and choose which harmonic currents to compensate for [24].

Another aspect regarding the currents is that the amplitudes of the filtered currents are much higher than for the non filtered currents. The reason for this is the filter. Having the large capacitors in shunt will produce much reactive power. Hence the currents in Fig. 6.12 will have a large reactive component making the amplitude higher than for the non filtered currents.

The voltages at the converter terminals are given in Fig. 6.13. It is evident that the line to line voltages are not as distorted as the currents. This is probably due to the rather strong connection to the stiff grid. At the grid terminals the voltage is purely sinusoidal.

6.2.2 Comparison with VSC

Here the performance of the power conditioning system developed in the master, from this point referred to as system M, is compared with the system developed in the project [33], from this point referred to as system P. During these simulations the line of events are different compared to the last section in order to comply with the sequence used in the project. As the losses were not studied in the project, their influence is not studied here. The software PSCAD was used for simulation in the project. One difference in the simulations was the reference power. In the project the goal of the SMES was to deliver constant power to a constant power load. In the master, the

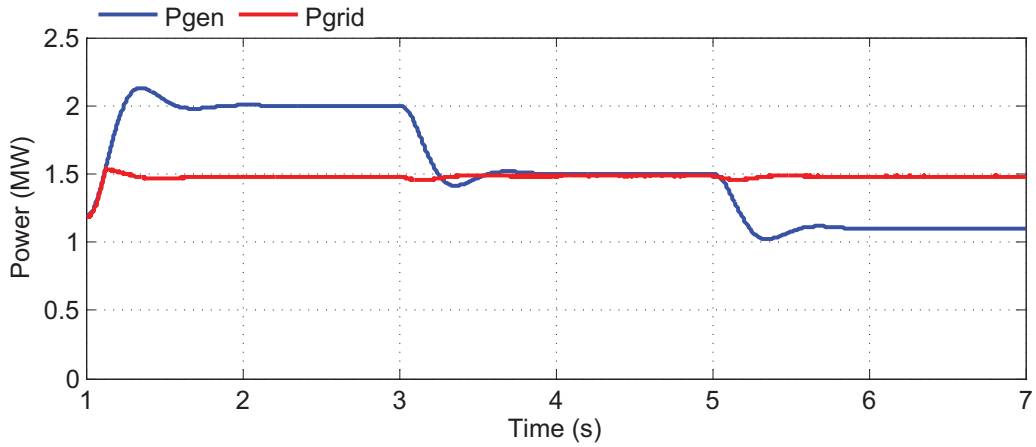

(a) System P.

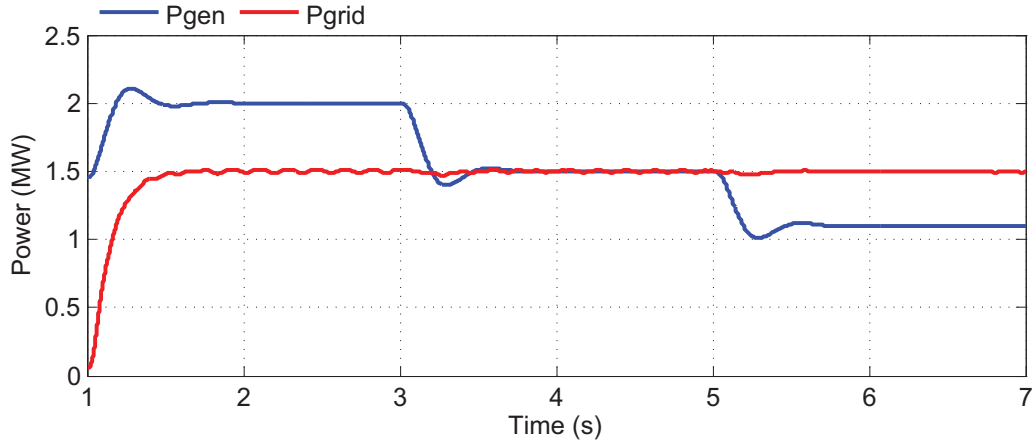

(b) System M.

Figure 6.14: The power output from the induction generator.

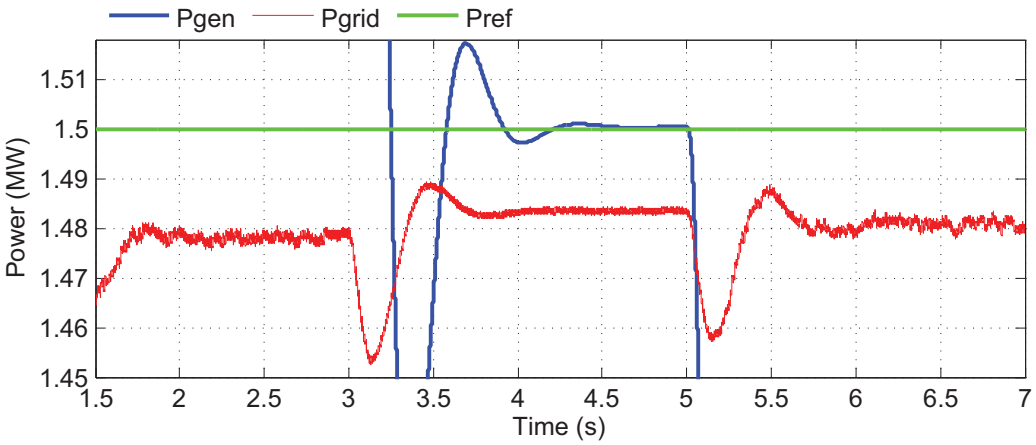

(a) System P.

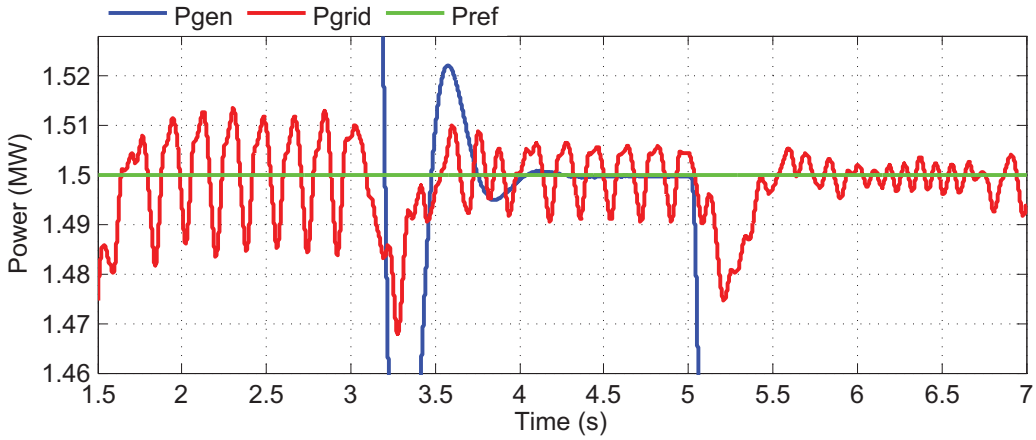

(b) System M.

Figure 6.15: Zoom of the power flow into the grid.

objective has been to deliver constant power to the grid. The difference is not significant. The start-up periods in the two models were not completely identical, but apart from that the events are similar. The output power of the induction generator is in both cases changed to force the SMES system to first absorb 0.5 MW for 2 s, then operate in steady state for 2 s and then deliver 0.4 MW for 2 s. This means a charging period followed by a pure energy storage mode, and then a discharging period. This sequence can seem a bit unrealistic, as the wind speed does not change this momentarily, but it tests the performance of the systems in a tough way. The power output for the two cases is shown together with the power flow into the grid in Fig. 6.14. The change in power output happens a little bit faster in system M. This is due to a larger moment of inertia in the generator of system P.

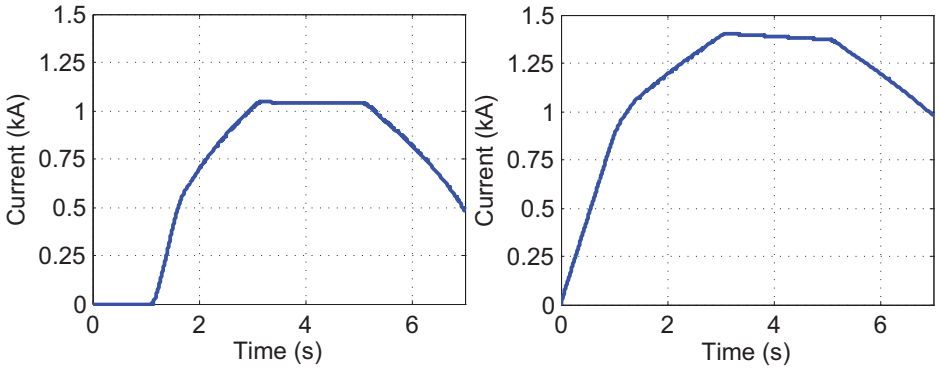

(a) System P. (b) System M.

Figure 6.16: Current in the coil during charging.

The power fluctuations from the generator are smoothed in both systems. However the power delivered to the grid has larger fluctuations in system M, than in system P as can be seen in Fig. 6.15. On the other hand the oscillations have higher frequency in system P. The power flow to the grid is neither maintained at the desired level. There is a deviation of about 20 kW, which corresponds to 1.33 % of the reference value. The biggest fluctuations in system M are in the same order as this, but the fluctuations become smaller when the operation mode changes. The reason for why the deviation is present in system P is probably that the reference power for the SMES to deliver does not equal the green line in Fig. 6.15a. Instead its reference is the difference in power between the generator output, and the constant load. This would have worked perfectly in a lossless system, but when there are losses in transformer and converter connection, some of the power dissipates on the way. These power losses should be counteracted for in the control system. The fluctuations in system M are not that easy to explain. One reason can be the rather simple control system. The response speed of this can be too slow to compensate for the disturbances. There is also a small ripple in the output power from the induction generator in system M. This ripple occurs due to a DC-offset in the currents. The result of this offset is that the three phase currents become slightly unbalanced, and thus the three phase power is not constant. However these oscillations are small compared to the power oscillations in the grid power, and are probably not too much involved in these oscillations.

The current in the coil during the simulation sequence is shown in Fig. 6.16. The current in system M is higher because the charging starts earlier. The maximum values of the currents are however not that interesting in this re-

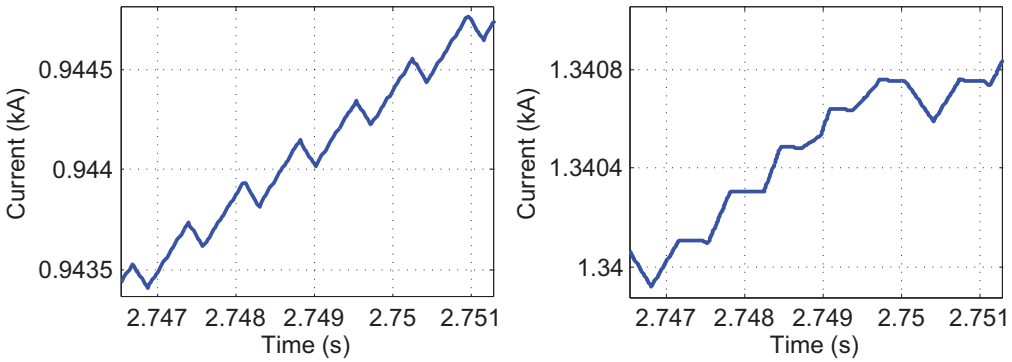

(a) System P. (b) System M.

Figure 6.17: Zoom of current in the coil during charging.

lation. The interesting factors are the changes and the behaviour of each system. When not considering the losses, the current in the coil does only say something about the energy level, and as long as there is enough energy the amount does not matter. It is evident that the current in system M decreases more during the steady state than in system P. The reason for this is that the steady state is difficult to reach because the power output from the generator is not entirely constant. The generator power is also more varying in PSIM than in PSCAD. From the two figures it is evident that the current in system P has a larger difference between the current at the end of steady state and at the end of simulation. The reason for this is not a less efficient system, but the fact that approximately the same amount of energy is extracted from both systems. Calculated based on the currents at 5 s and 7 s, the energy difference is 810 kJ in system P and 829 kJ in system M. The difference is 19 kJ which equals 2.3 % of the energy from system M. This distinction can come from the fact that system M is modeled with real IGBTs, while system P has ideal switches. It can be attributed to numerical differences. System P had to be simulated with a plot step of 80 µs when the calculation time step was 10 µs because of instabilities of the simulation software if simulating with too low plot step. The accuracy of the plotting is less for larger time steps.

Fig. 6.17 shows the different shapes of the current while charging in the two systems. System P is able to charge faster because the voltage applied to the coil can be maintained on a higher level because it is a constant DC-voltage. The voltage applied to the coil in system M is an AC-voltage with non constant amplitude. This makes the coil current more untidy.

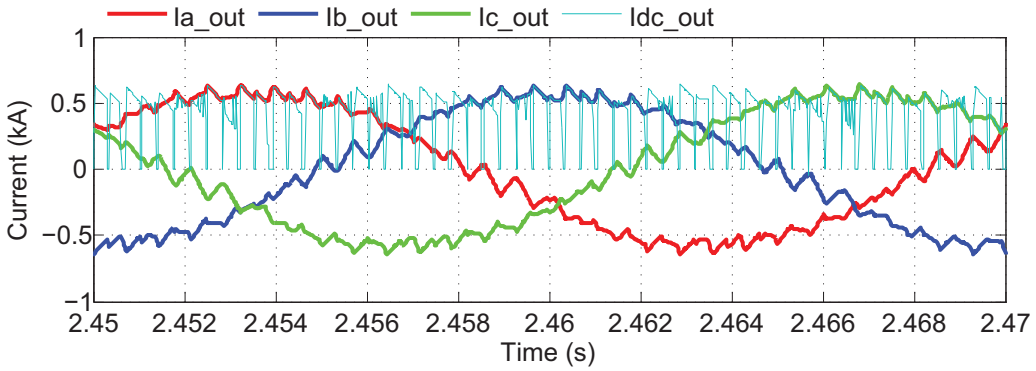

Figure 6.18: The output current from the converter in system P during charge, together with current on DC-side.

The output current from the converter in system P is shown in Fig. 6.18 together with the current on the DC-side. The output currents from the converter in system M are similar for this case as the previous case, and can be seen in Fig. 6.11. The currents out of the VSC are not as distorted as those out from the CSC. The reason for this is that the current in the DC-link of the converter in system P is not constant, but follows the current on the AC-side, though it is not crossing the zero line depending on the direction of the power flow. The DC-current in Fig. 6.18 is positive, thus the power flow is into the SMES. In the CSC it is different. It is the current on the DC-side which dictates the current on the AC-side. The shape of the AC-current becomes a square wave because of this. The voltages on the AC-side of the VSC have the same shape as the currents directly out of the CSC. In the VSC it is the constant DC-voltage which dictates the AC-side voltage. This illustrates the opposite nature of the two converter typologies.

The filtered currents from the VSC can be seen in Fig. 6.19a. Compared to the currents from the CSC in Fig. 6.19b they are much nicer. They have a shape closer to sinusoidal, and are very good balanced. However they look as being influenced by third harmonics due to the sag at the peaks which is a sign of this. The same can be spotted in Fig. 6.19b, but these currents are also polluted by other harmonics. It seems like it is easier to filter the pollutions from the distorted voltage from the VSC than it is to filter the polluted currents from the CSC. The VSC does also require quite large capacitor banks to make the currents smooth, and as for the CSC in the previous section it is evident that the filtered currents have a large reactive component. It is clear that the amplitude of the filtered currents is about twice the amplitude of the currents straight from the converter. This extra amplitude will give higher losses in the converter connection, and should

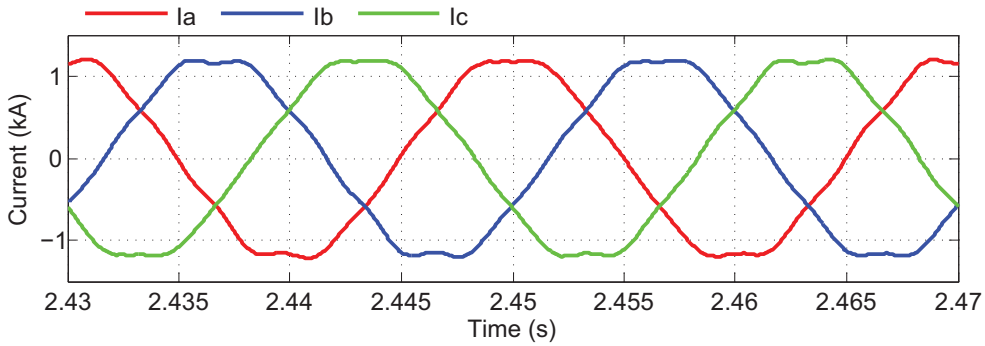

(a) System P.

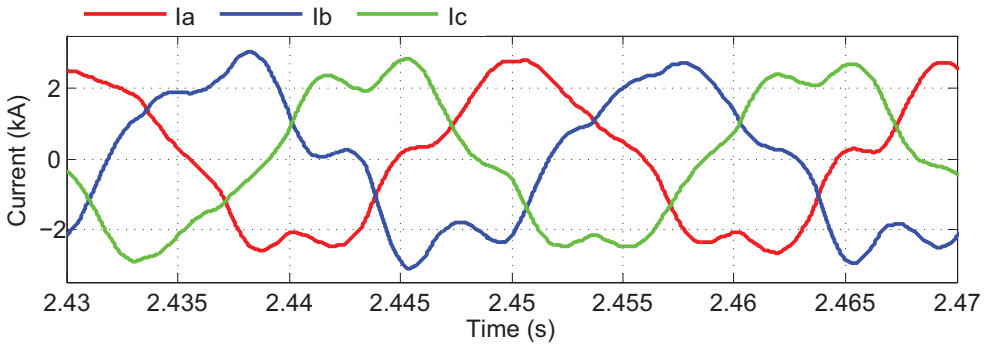

(b) System M.

Figure 6.19: The filtered currents from the converter.

ideally be avoided.

The reactive power flow is shown in Fig. 6.20. System M has clearly the most reactive power to deal with. The reactive power consumption of the two induction generators is fairly similar. Being two machines with the same rating and operating on the same voltage this stands to reason. The reactive power consumption is proportional to the active power generation, and this drops when the wind speed drops. In system P, the reactive power output from the converter, Q_smes is varying to some extent with the changing active power output. However this should not be the case as the converter is set to only compensate for active power. The reason for why it is doing it is that the control system is not completely decoupled; hence a demand for active power will also give some reactive power. In system M, the reactive power output from the converter is almost equal to the requirement of the generator. This shows that the system in addition to being an active power compensator also works as a reactive power compensator. This is a consequence of the control system using the abc-theory which in this case does

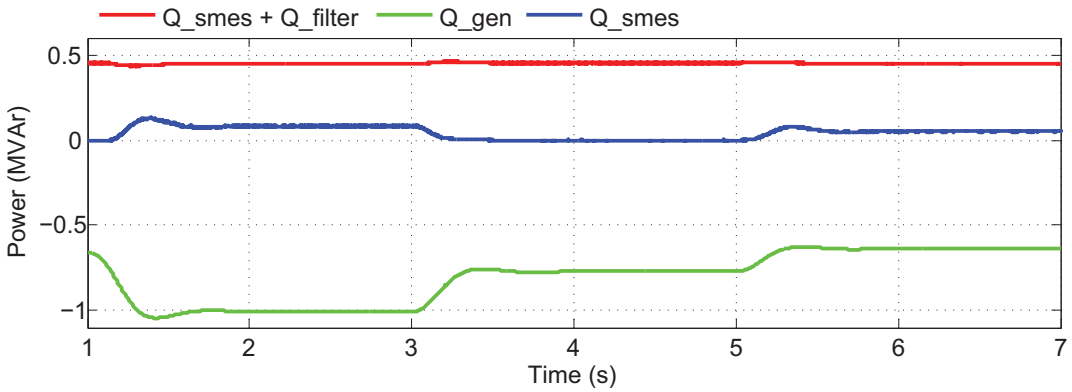

(a) System P.

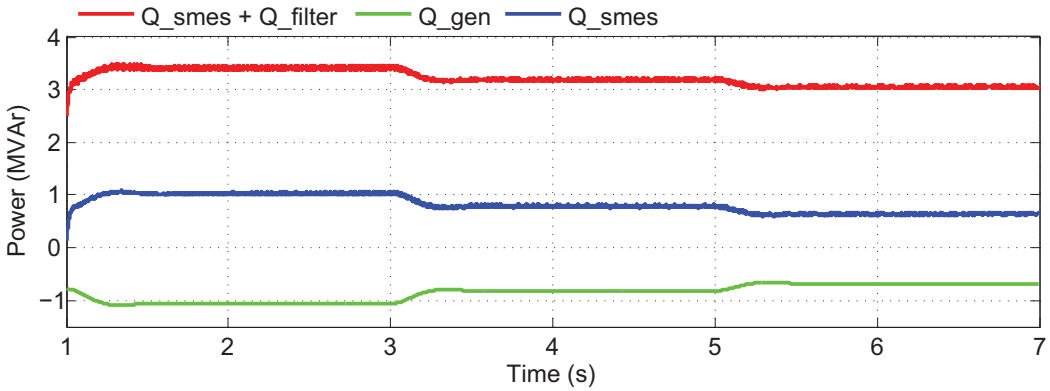

(b) System M.

Figure 6.20: Reactive power in converters, filters and generators.

not distinguish between active and reactive power. Thus it is not possible to compensate for only one of the power components. When supporting an induction generator this is necessarily not only negative. However the reactive power compensation from the SMES seems superfluous when the capacitors in the filter provide that much reactive power. The reason for why the filter in system M produces much more reactive power than the filter in system P is the voltage level. In system P the line to line RMS-voltage is 690 V, while it is 1100 V in system M. The reactive power production is dependent on the voltage squared.

6.3 High switching frequency

Due to the relatively large amounts of power transmitted here, the switching frequency had to be set to a fairly low value. The harmonic content in the currents is as a result of this quite high. In this section the filtered currents are studied for the high switching frequency ten times higher than the frequency used here, 14 kHz. Today this is unrealistic at the power levels in this system. However in the future a new switch technology using chemical vapour deposition (CVD) diamond triode can utilize high switching frequency, low conduction losses and low switching losses [27]. Fig. 6.21 shows the currents after the filter for this high switching frequency. It is clear that they are closer to sinusoidal shape than the ones in Fig. 6.12, and the advantage of high switching frequency is evident. The amplitude is still influenced by the reactive component, which proves that the filtering requirement has not disappeared, but the filter works better for this high switching frequency. Because the switching frequency is so high the switching losses will get very high, thus making it inappropriate to use in this connection. For low power applications, such as wave power units this converter would maybe be a viable solution. When not being in the megawatt-range the switches can be scaled down, and switching frequency increased. This is also seen from Eq. 4.20, where both the P_{cond}-term and the switching energies in the denominator would be smaller.

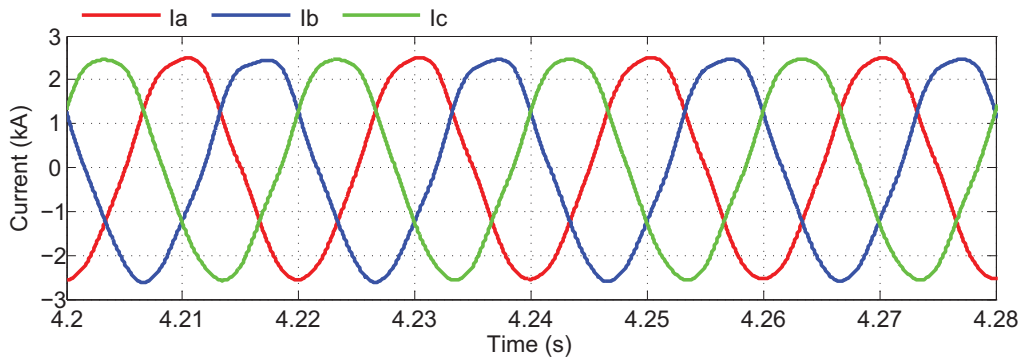

Figure 6.21: The currents after the filter at a switching frequency of 14 kHz

Chapter 7

Conclusion and further work

7.1 Conclusion

In this master thesis a power conditioning system for SMES has been demonstrated. The conditioning system is based on a current source converter (CSC) typology. This typology is not as common as its counterpart, the voltage source converter (VSC). The CSCs feasibility as an interface between the superconducting coil and the power system was because of this desirable to study. A comparison with results from the project thesis carried out in the autumn which concentrated on a VSC/DC-chopper based converter system was carried out too.

The results from an educational trip in the autumn to Tokyo Institute of Technology, Japan has also been presented. An experiment on a force balanced superconducting coil was participated on here, but the results were not ready before this year. One of the goals of the experiment was to cool the superconducting coil to 2 K (supercooling) in order to improve its performance, and get closer to the theoretical limit of magnetic field and current. The results from this experiment showed that the difference between atmospheric pressurized liquid helium of 4 K and the supercooled was minor. In fact the record magnetic field was not obtained when using the supercooled helium.

The SMES was as in the project thesis connected in shunt with the power system. The control system consisted of one PI-regulator working on the power and giving a reference to a block where the reference currents on the AC-side were calculated. Both active and reactive power was compensated.

The SMES system was capable of compensating for fluctuating power from an induction generator. The power delivered to the grid was kept on a nearly constant level, although ripple was present. The efficiency of the

converter proved to be acceptable, both when referring to the power flow in the converter and the energy stored.

The comparison with the typology from the project thesis was giving the best results for the converter system from the project. This had smaller ripple in the compensated power, and less distorted currents from the converter. However it is hard being too dogmatic on the conclusion here because the converter system during the master thesis was implemented late in the semester due to a misunderstanding. This limited the development of the converter system.

The high distortion in the currents from the converter proved that this solution might not be the best for such a high power application as wind power. The results from the simulations with higher switching frequency proved that the converter would act better for a situation like this. The converter should because of that be further investigated on wave power and other low power applications.

7.2 Further work

There are several topics which could be further investigated in the SMES concept. Some of them are:

- Improvement of the control system.
- Better filtering of the output currents from the converter.
- Investigation of SMES to be used for low power applications, such as wave power.
- Different connection strategies of the converter. Series compensation or both series and shunt compensation.
- Fault response of the system.

Bibliography

[1] "Renewable Energy Focus." http://www.renewableenergyfocus.com/view/5304/six-renewable-energy-sources-judged-to-be-best-prospect-for-future-says-report/.

[2] J. Kondoh, I. Ishii, H. Yamaguchi, A. Murata, K. Otani, K. Sakuta, N. Higuchi, S. Sekine, and M. Kamimoto, "Electrical energy storage systems for energy networks," *Energy Conversion & Management*, vol. 41, pp. 1863–1874, February 2000.

[3] U. D. of Energy, "20% wind energy by 2030," July 2008.

[4] T. Ackermann, *Wind Power in Power Systems*. Chichester: Wiley, 2005.

[5] J. F. Manwell, J. G. McGowan, and A. L. Rogers, *Wind Energy Explained*. Wiley, 2007.

[6] S. M. Muyeen, J. Tamura, and T. Murata, *Stability Augmentation of a Grid-connected Wind Farm*. Springer, 2008.

[7] A. J. Pujante-López, E. Gómez-Lázaro, J. Fuentes-Moreno, A. Molina-García, and A. Vigueras-Rodríguez, "Performance compariosn of a 2 MW DFIG wind turbine model under wind speed variations," in *EWEC 2009 conference proceedings*, 2009.

[8] J. Machowski, J. Bialek, and J. Bumby, *Power System Dynamics*. Wiley, 2008.

[9] Y. huei Wan and D. B. Jr., "Short-term power fluctuations of large wind power plants," tech. rep., National Renewable Energy Laboratory, 2002.

[10] J. Bray, "Superconductors in applications; some practical aspects," *Applied Superconductivity, IEEE Transactions on*, vol. 19, pp. 2533–2539, June 2009.

[11] "American Magnetics."
http://www.americanmagnetics.com/tutorial/charactr.html.

[12] H. Boenig and J. Hauer, "Commissioning Tests of the Bonneville Power Administration 30 MJ Superconducting Magnetic Energy Storage Unit," *Power Apparatus and Systems, IEEE Transactions on*, vol. PAS-104, pp. 302–312, Feb. 1985.

[13] P. Tixador, "Superconducting magnetic energy storage: Status and perspective," *IEEE/CSC and ESAS European superconductivity news forum*, January 2008.

[14] S. Nomura, N. Tanaka, K. Tsuboi, H. Tsutsui, S. Tsuji-Iio, and R. Shimada, "Design considerations for SMES systems applied to HVDC links," in *Power Electronics and Applications, 2009. EPE '09. 13th European Conference on*, pp. 1–10, Sept. 2009.

[15] K. F. da Silva and M. Saidel, "Digital control and integration of a 192 mw wind farm with doubly fed induction generator into the brazilian power system," *Electric Power Systems Research*, vol. 80, no. 1, pp. 108 – 114, 2010.

[16] A. T. Holen, O. B. Fosso, and K. J. Olsen, *TET4115 Power system analysis TET5100 Power engineering updates*. NTNU Institutt for elkraftteknikk, 2007.

[17] N. G. Hingorani and L. Gyugyi, *Understanding FACTS: Concepts and Technology and Technology of Flexible AC Transmission Systems*. IEEE Press, 2000.

[18] M. Routimo, M. Salo, and H. Tuusa, "Comparison of voltage-source and current-source shunt active power filters," in *Power Electronics Specialists Conference, 2005. PESC '05. IEEE 36th*, pp. 2571 –2577, 16-16 2005.

[19] A. Odaka, J. Itoh, I. Sato, H. Ohguchi, H. Kodachi, N. Eguchi, and H. Umida, "Analysis of loss and junction temperature in power semiconductors of the matrix converter using simple simulation methods," in *Industry Applications Conference, 2004. 39th IAS Annual Meeting. Conference Record of the 2004 IEEE*, vol. 2, pp. 850 – 855 vol.2, 3-7 2004.

[20] "Ixys Product Portofolio."
http://www.ixys.com/Product _portfolio/power _devices.asp.

[21] B. Backlund and E. Carroll, "Voltage ratings of high power semiconductors," tech. rep., ABB, 2006.

[22] Mohan, Undeland, and Roobins, *Power Electronics Converters, Applications and Design*. John Wiley & Sons, 2003.

[23] "Industrial Control Design Line."
$http://www.industrialcontroldesignline.com/howto/198000755;jsessionid=CMU0R1CMI33VJQE1GHPCKHWATMY32JVN?pgno=5$.

[24] H. Akagi, E. H. Watanabe, and M. Aredes, *Instantaneous Power Theory and Applications to Power Conditioning*. John Wiley & Sons, 2007.

[25] Hassi, Weir, and Thomas, *University Calculus*. Pearson Addison Wesley, 2007.

[26] D. G. Holmes and T. A. Lipo, *Pulse Width Modulation For Power Converters*. Wiley Interscience, 2003.

[27] B. Wang and J. J. Cathey, "DSP-controlled, space-vector PWM, current source converter for STATCOM application," *Electric Power Systems Research*, vol. 67, no. 2, pp. 123 – 131, 2003.

[28] E. Kreyszig, *Advanced Engineering Mathematics*. John Wiley & Sons, 1999.

[29] N. Holtsmark, "Reactive power compensation using a matrix converter," 2009. Project thesis, NTNU.

[30] V. Prasad, "Analysis and comparison of space vector modulation schemes for three-leg and four-leg voltage source inverters," Master's thesis, Virginia Polytechnic Institute and State University, 1997.

[31] Powersim Inc., *PSIM User Manual*, January 2010.

[32] S. Nomura, T. Shintomi, S. Akita, T. Nitta, R. Shimada, and S. Meguro, "Technical and Cost Evaluation on SMES for Electric Power Compensation." Presentation at 21st International Conference on Magnet Technology, Hefei China, October 2009.

[33] K. E. Nielsen, "Superconducting magnetic energy storage (smes in power systems with renewable energy sources," 2009. Project thesis, NTNU.

Appendix A

Key parameters of the model FBC

Table A.1: Key parameters of the model FBC.

This appendix shows the key parameters of the model FBC used in the experiment at Tokyo Institute of Technology.

Coil configuration	Force-balanced coil
Superconductor	NbTi/Cu composite (ϕ 1.17 mm)
Winding form	Aluminium alloy
Outer diameter /inner diameter /height (m)	0.53 /0.27 /0.13
Helical windings	6 poloidal turns $\times$ 3 coils
Total number of poloidal turns	10584
Critical coil current (A)	552
Self inductance (H)	1.8
Conductor length (km)	3.9
Maximum magnetic field (T)	7.1
Maximum magnetic energy (kJ)	270
Weight (kg)	50 (incl. winding form)

Appendix B

Component parameters

Table B.1: The wind turbine parameters.

Machine parameter	*Value*
Nominal output power (MW)	2.0
Base wind speed (m\s)	12
Base rotational speed (rpm)	15
Moment of inertia (kgm^2)	5.9×10^6

Table B.2: The induction generator parameters.

Machine parameter	*Value*
Nominal output power (MW)	2.0
Rated RMS voltage (V)	690
Rated RMS current (A)	1675
Speed rating (rpm)	1500
Stator resistance, Rs (Ω)	0.0022
Stator inductance, Ls (mH)	0.119722
Rotor resistance, Rr (Ω)	0.0018
Rotor inductance, Lr (mH)	0.049329
Magnetizing inductance, Lm (mH)	2.93191
No. of Poles	4
Moment of inertia (kgm^2)	59

Table B.3: The transformer data.

Machine parameter	*Value*
Resistance primary, Rp (Ω)	0.001
Resistance secondary, Rs (Ω)	0.001
Leakage inductance primary Lp (mH)	0.01
Leakage inductance secondary (mH)	0.01
Magnetizing inductance, Lm (mH)	500
Primary side RMS voltage (V)	1100
Secondary side RMS voltage (V)	1100 & 690

Appendix C

Different switching frequencies

The following figures shows the difference between the power output to the grid for different switching frequencies. They range from 1.0 kHz to 1.5 kHz.

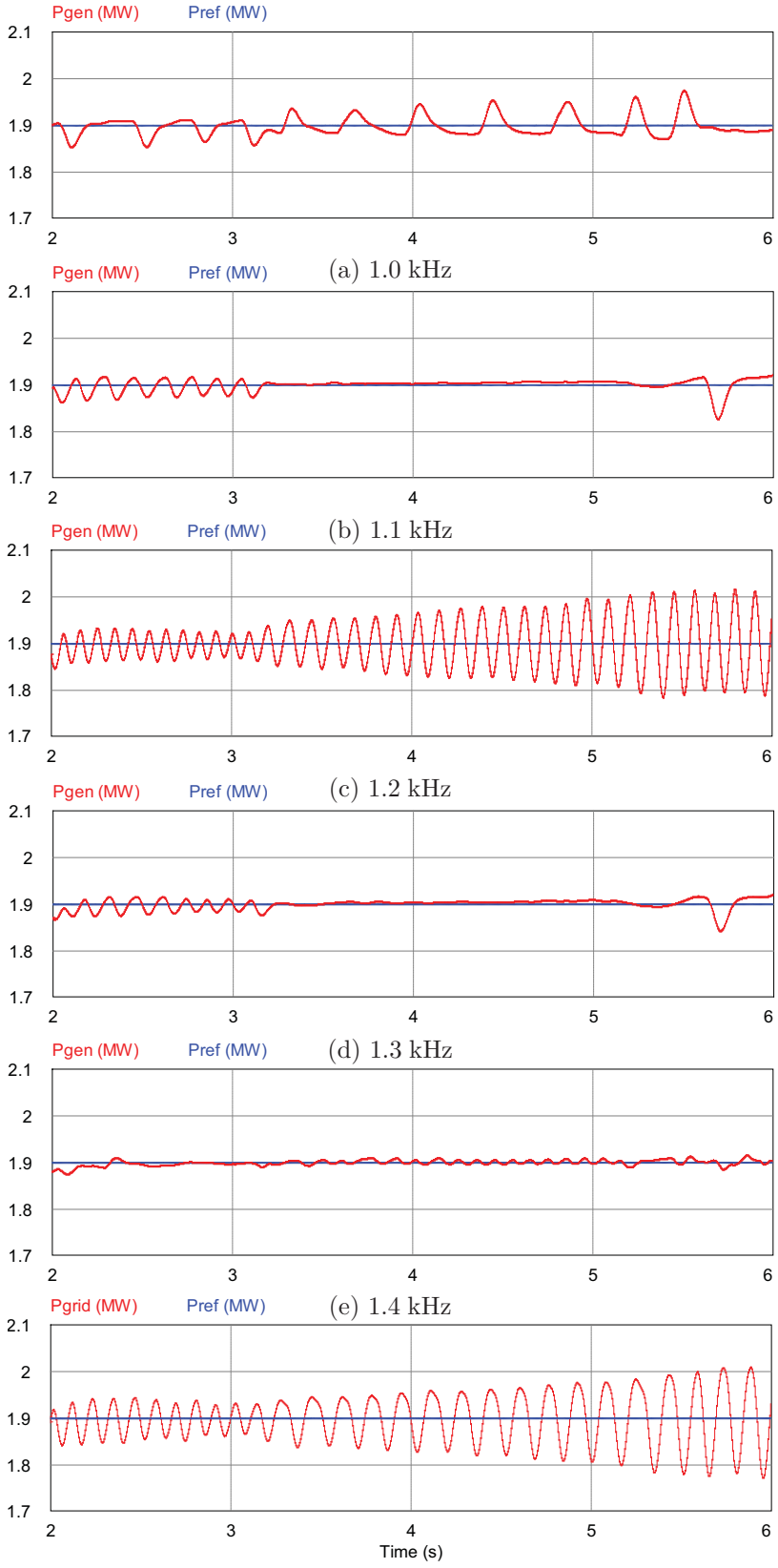

(a) 1.0 kHz

(b) 1.1 kHz

(c) 1.2 kHz

(d) 1.3 kHz

(e) 1.4 kHz

(f) 1.5 kHz

Figure C.1: The power to the grid for different switching frequencies.

Appendix D

Simulation model from PSIM

This appendix contains the simulation model from PSIM. The first shows the system modeled. The second is the converter. The third is the control and modulation.

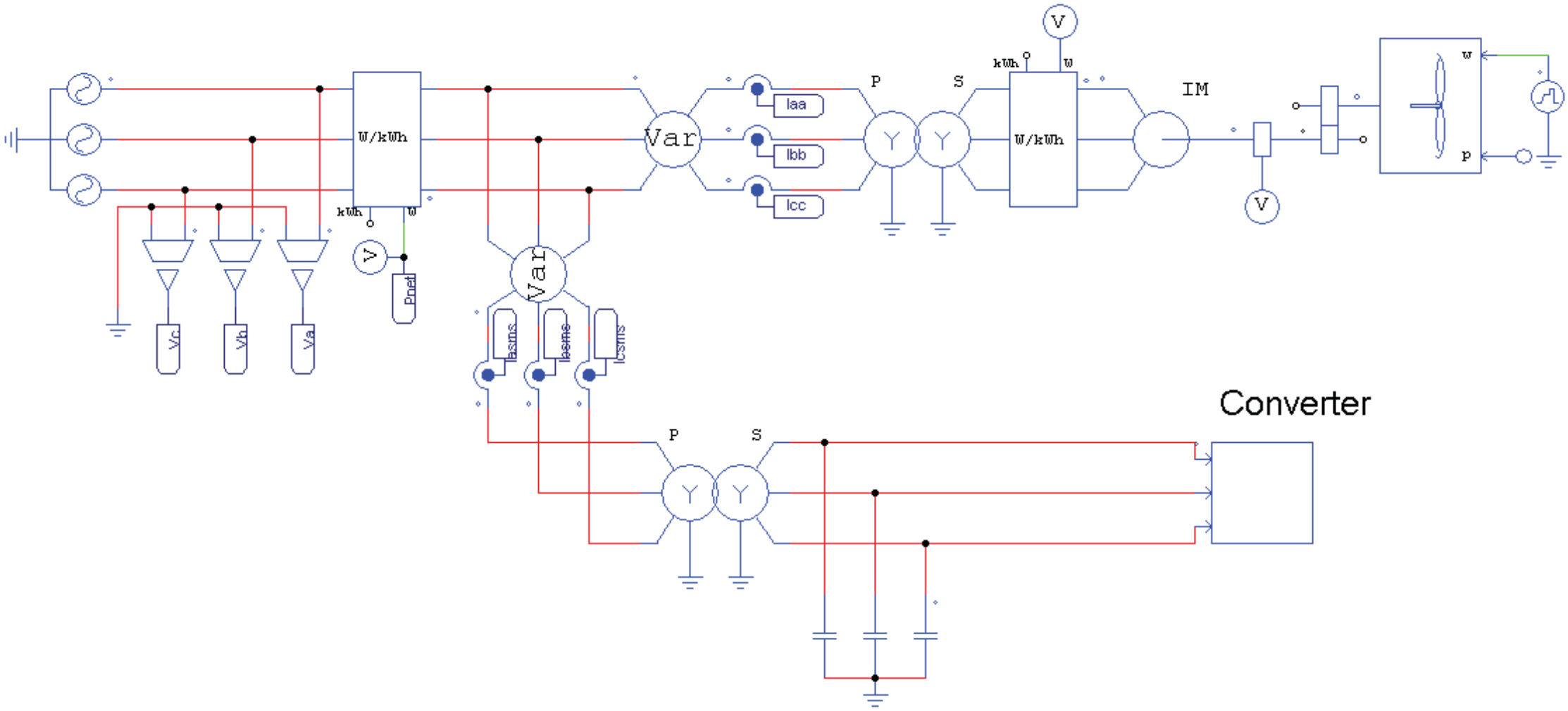
W/kWh
kWh
W
V
Pnet
Vc
Vb
Va
Var
Iaa
Ibb
Icc
P
S
V
kWh
W
W/kWh
IM
V
w
p
Var
Iasms
Ibsms
Icsms
P
S
Converter

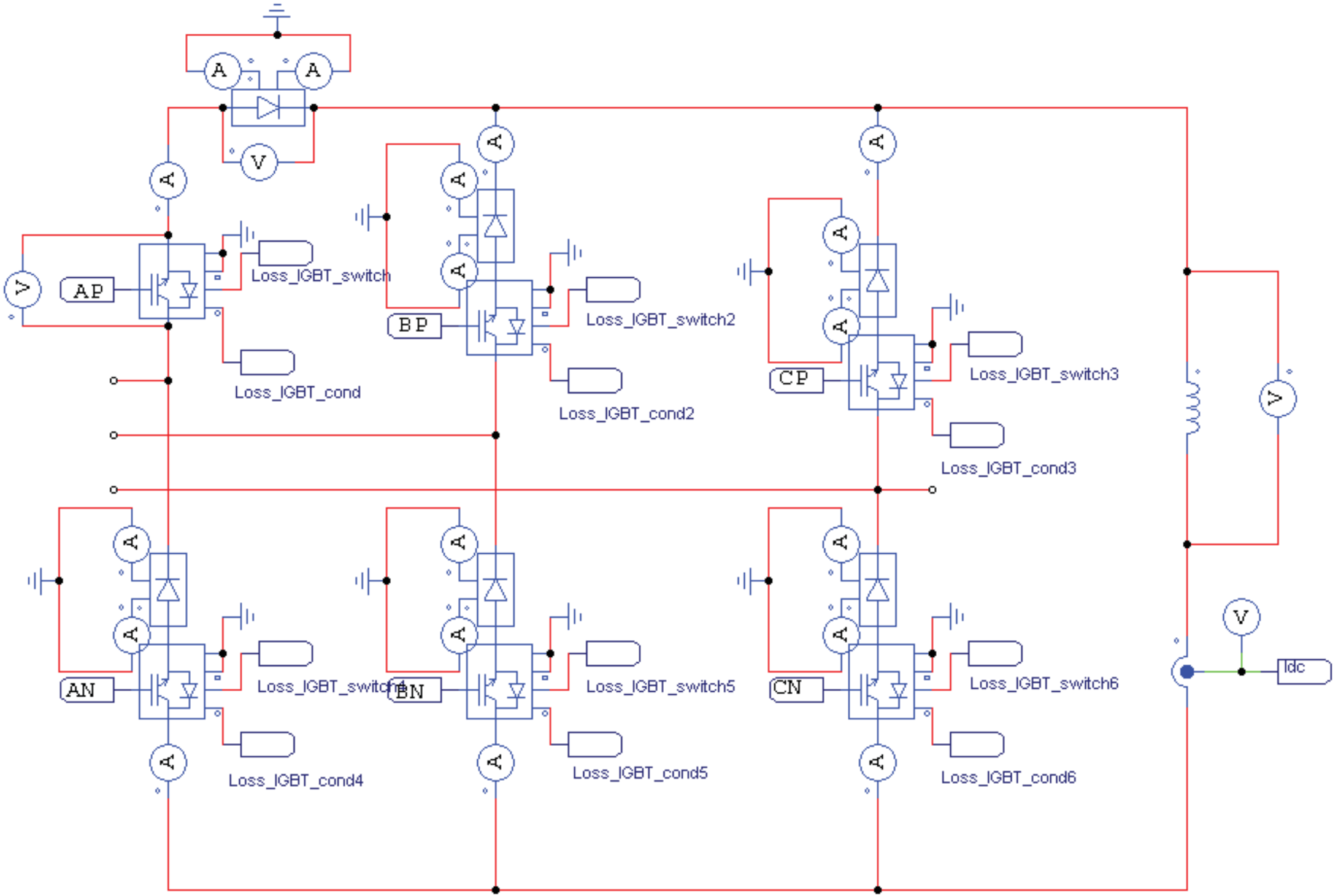
A
A
V
A
V
AP
Loss_IGBT_switch
Loss_IGBT_cond
A
A
A
BP
Loss_IGBT_switch2
Loss_IGBT_cond2
A
A
A
CP
Loss_IGBT_switch3
Loss_IGBT_cond3
V
V
Idc
A
A
A
AN
Loss_IGBT_switch4
Loss_IGBT_cond4
A
A
A
BN
Loss_IGBT_switch5
Loss_IGBT_cond5
A
A
A
CN
Loss_IGBT_switch6
Loss_IGBT_cond6

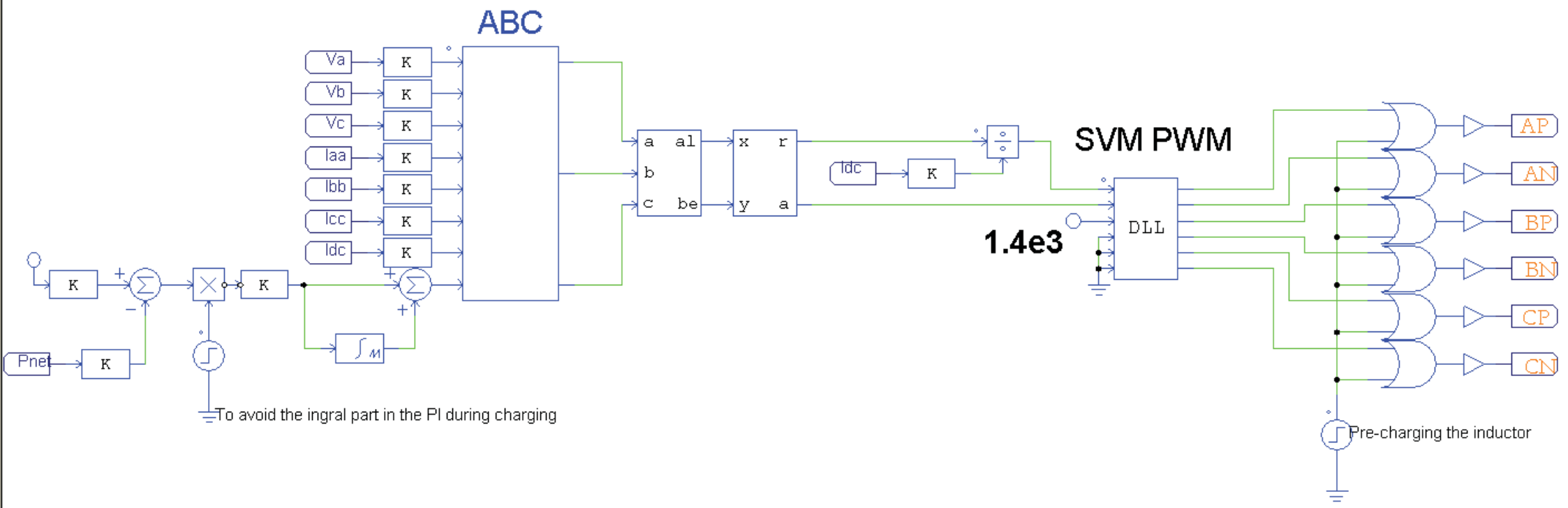
ABC
Va
Vb
Vc
Iaa
Ibb
Icc
Idc
K
a al
b
c be
x r
y a
Idc
K
1.4e3
SVM PWM
DLL
AP
AN
BP
BN
CP
CN
Pnet
K
K
K
To avoid the ingral part in the PI during charging
Pre-charging the inductor

Appendix E

Space vector modulation

The following shows the c-code used to utilize the space vector modulation pulse width modulation.

```
/*
    Space vector modulation for the Current Source Rectifier:
*/
#include <math.h>
// constants
#define ws  314.1592653589793    // 2*pi*50
#define mr  1.632993161855452    // 2*sqrt(2/3)
#define pi3 1.047197551196598    // pi/3
#define s32 0.866025403784439    // sqrt(3)/2
#define DPI 6.283185307179580    // 2*pi
#define pi6 0.523598775598299    // pi/6

typedef struct {
    int e;
    double b;
}knut;

// ------------ Determine the position of the vector ------------//
knut posicion(double a)
{
    knut var;

    int R;
    double an;
    R = 0;
    an = a + pi6;
    if (an<0)
    {
        an = DPI + an;   // angle between 0 and 2*pi
    }
    if (an>DPI)
    {
        an = an-DPI;
    }
    an = an / pi3;      // multiple of pi/3
    R = floor(an);
    // return R;
    var.e = R;
    var.b = an;

    return var;
}

//----------------- Main Function --------------------------//
__declspec(dllexport) void simuser (t, dt, in, out)
double t, dt;
double *in, *out;
{
// variables
    double angel;
    double Tp;
    double anr;
    double sap;
    double sbp;
    double scp;
    double san;
    double sbn;
    double scn;
    double wap;
    double wbp;
    double wcp;
    double wan;
    double wbn;
    double wcn;
    double za;
    double zb;
    double zc;
    double M;

// static variables
    static double tt  = 0;
    static double dxx = 0;
    static double dyy = 0;
    static double dzz = 0;
```

```
    static int    S   = 0;
// input
    M      = in[0];                 // current ratio
    angel = in[1];                  // angle
    Tp     = 1/in[2];               // 1/frequency
    if (angel<0)
    {
        angel = DPI + angel;
    }
    tt = tt + dt;
// Determine the sector
    if (t>Tp)
    {
        knut u;
        u = posicion(angel); // position
        S = u.e;
    }
    anr = angel-S*pi3;              // rotate
// change reference vector
if (tt>Tp)
{
    tt  = 0;
    dyy = M*sin(pi6+anr)*Tp;
    dxx = M*sin(pi6-anr)*Tp;
    dzz = (Tp-dxx-dyy);
}
// output:
    sap = 0;
    sbp = 0;
    scp = 0;
    san = 0;
    sbn = 0;
    scn = 0;
    wap = 0;
    wbp = 0;
    wcp = 0;
    wan = 0;
    wbn = 0;
    wcn = 0;
    za = 0;
    zb = 0;
    zc = 0;

switch(S)
{
case 0: // ab-ac
    {
    sap = 1;
    sbn = 1;

    wap = 1;
    wcn = 1;

    za = 1;

    break;
    }
case 1: // ac-bc
    {
    sap = 1;
    scn = 1;

    wbp = 1;
    wcn = 1;

    zc = 1;

    break;
    }
case 2: // bc-ba
    {
    sbp = 1;
    scn = 1;
```

```
    wbp = 1;
    wan = 1;

    zb = 1;

    break;
    }
case 3: // ba-ca
    {
    sbp = 1;
    san = 1;

    wcp = 1;
    wan = 1;

    za = 1;

    break;
    }
case 4: // ca-cb
    {
    scp = 1;
    san = 1;

    wcp = 1;
    wbn = 1;

    zc = 1;

    break;
    }
case 5: // cb-ab
    {
    scp = 1;
    sbn = 1;

    wap = 1;
    wbn = 1;

    zb = 1;

    break;
    }
}
// output
if(tt<dxx)
{
    out[0] = sap;
    out[1] = san;
    out[2] = sbp;
    out[3] = sbn;
    out[4] = scp;
    out[5] = scn;
    out[6] = 0.5;
    out[7] = S;
}
else
{
    if(tt<(dxx+dyy))
    {

      out[0] = wap;
      out[1] = wan;
      out[2] = wbp;
      out[3] = wbn;
      out[4] = wcp;
      out[5] = wcn;
      out[6] = 1.0;
      out[7] = S;
    }
    else
    {

      out[0] = za;
```

```
      out[1] = za;
      out[2] = zb;
      out[3] = zb;
      out[4] = zc;
      out[5] = zc;
      out[6] = 0;
      out[7] = S;
    }
}
//:-----------------------------:
}
```

Appendix F

Data sheets

The data sheets for the IGBT and diode used from ABB are given here.

V_{CE} = 3300 V
I_C = 1500 A

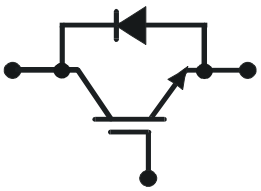

ABB HiPak™

IGBT Module

5SNA 1500E330300

Doc. No. 5SYA 1595-00 July 07

- **Ultra low-loss, rugged SPT+ chip-set**
- **Smooth switching SPT+ chip-set for good EMC**
- **Industry standard package**
- **High power density**
- **AlSiC base-plate for high power cycling capability**
- **AlN substrate for low thermal resistance**

Maximum rated values [1]

Parameter	Symbol	Conditions	min	max	Unit
Collector-emitter voltage	V_{CES}	V_{GE} = 0 V		3300	V
DC collector current	I_C	T_c = 85 °C		1500	A
Peak collector current	I_{CM}	t_p = 1 ms, T_c = 85 °C		3000	A
Gate-emitter voltage	V_{GES}		-20	20	V
Total power dissipation	P_{tot}	T_c = 25 °C, per switch (IGBT)		11750	W
DC forward current	I_F			1500	A
Peak forward current	I_{FRM}			3000	A
Surge current	I_{FSM}	V_R = 0 V, T_{vj} = 125 °C, t_p = 10 ms, half-sinewave		14000	A
IGBT short circuit SOA	t_{psc}	V_{CC} = 2500 V, $V_{CEM\,CHIP} \leq$ 3300 V $V_{GE} \leq$ 15 V, $T_{vj} \leq$ 125 °C		10	µs
Isolation voltage	V_{isol}	1 min, f = 50 Hz		6000	V
Junction temperature	T_{vj}			150	°C
Junction operating temperature	$T_{vj(op)}$		-40	125	°C
Case temperature	T_c		-40	125	°C
Storage temperature	T_{stg}		-40	125	°C
Mounting torques [2]	M_s	Base-heatsink, M6 screws	4	6	Nm
	M_{t1}	Main terminals, M8 screws	8	10	
	M_{t2}	Auxiliary terminals, M4 screws	2	3	

[1] Maximum rated values indicate limits beyond which damage to the device may occur per IEC 60747
[2] For detailed mounting instructions refer to ABB Document No. 5SYA2039

IGBT characteristic values [3]

Parameter	Symbol	Conditions		min	typ	max	Unit
Collector (-emitter) breakdown voltage	$V_{(BR)CES}$	V_{GE} = 0 V, I_C = 10 mA, T_{vj} = 25 °C		3300			V
Collector-emitter [4] saturation voltage	$V_{CE\ sat}$	I_C = 1500 A, V_{GE} = 15 V	T_{vj} = 25 °C		2.4		V
			T_{vj} = 125 °C		3.0	3.4	V
Collector cut-off current	I_{CES}	V_{CE} = 3300 V, V_{GE} = 0 V	T_{vj} = 25 °C			12	mA
			T_{vj} = 125 °C			120	mA
Gate leakage current	I_{GES}	V_{CE} = 0 V, V_{GE} = ±20 V, T_{vj} = 125 °C		-500		500	nA
Gate-emitter threshold voltage	$V_{GE(TO)}$	I_C = 240 mA, V_{CE} = V_{GE}, T_{vj} = 25 °C		4.5		6.5	V
Gate charge	Q_{ge}	I_C = 1500 A, V_{CE} = 1800 V, V_{GE} = -15 V .. 15 V			11.0		µC
Input capacitance	C_{ies}	V_{CE} = 25 V, V_{GE} = 0 V, f = 1 MHz, T_{vj} = 25 °C			152		nF
Output capacitance	C_{oes}				12.2		
Reverse transfer capacitance	C_{res}				3.77		
Turn-on delay time	$t_{d(on)}$	V_{CC} = 1800 V, I_C = 1500 A, R_G = 1.0 Ω, C_{GE} = 220 nF, V_{GE} = ±15 V, L_σ = 100 nH, inductive load	T_{vj} = 25 °C		600		ns
			T_{vj} = 125 °C		570		
Rise time	t_r		T_{vj} = 25 °C		220		ns
			T_{vj} = 125 °C		250		
Turn-off delay time	$t_{d(off)}$	V_{CC} = 1800 V, I_C = 1500 A, R_G = 1.5 Ω, C_{GE} = 220 nF, V_{GE} = ±15 V, L_σ = 100 nH, inductive load	T_{vj} = 25 °C		1480		ns
			T_{vj} = 125 °C		1680		
Fall time	t_f		T_{vj} = 25 °C		380		ns
			T_{vj} = 125 °C		470		
Turn-on switching energy	E_{on}	V_{CC} = 1800 V, I_C = 1500 A, R_G = 1.0 Ω, C_{GE} = 220 nF, V_{GE} = ±15 V, L_σ = 100 nH, inductive load	T_{vj} = 25 °C		1380		mJ
			T_{vj} = 125 °C		2000		
Turn-off switching energy	E_{off}	V_{CC} = 1800 V, I_C = 1500 A, R_G = 1.5 Ω, C_{GE} = 220 nF, V_{GE} = ±15 V, L_σ = 100 nH, inductive load	T_{vj} = 25 °C		1940		mJ
			T_{vj} = 125 °C		2680		
Short circuit current	I_{SC}	t_{psc} ≤ 10 µs, V_{GE} = 15 V, T_{vj} = 125 °C, V_{CC} = 2500 V, $V_{CEM\ CHIP}$ ≤ 3300 V			6500		A
Module stray inductance	$L_{\sigma\ CE}$				10		nH
Resistance, terminal-chip	$R_{CC'+EE'}$		T_C = 25 °C		0.06		mΩ
			T_C = 125 °C		0.085		

[3] Characteristic values according to IEC 60747 – 9
[4] Collector-emitter saturation voltage is given at chip level

Diode characteristic values [5]

Parameter	Symbol	Conditions		min	typ	max	Unit
Forward voltage [6]	V_F	I_F = 1500 A	T_{vj} = 25 °C		2.0		V
			T_{vj} = 125 °C		2.1	2.55	
Reverse recovery current	I_{rr}	V_{CC} = 1800 V, I_F = 1500 A, V_{GE} = ±15 V, R_G = 1.0 Ω, C_{GE} = 220 nF, L_σ = 100 nH inductive load	T_{vj} = 25 °C		1850		A
			T_{vj} = 125 °C		2100		
Recovered charge	Q_{rr}		T_{vj} = 25 °C		960		µC
			T_{vj} = 125 °C		1590		
Reverse recovery time	t_{rr}		T_{vj} = 25 °C		750		ns
			T_{vj} = 125 °C		1160		
Reverse recovery energy	E_{rec}		T_{vj} = 25 °C		1200		mJ
			T_{vj} = 125 °C		2030		

[5] Characteristic values according to IEC 60747 – 2
[6] Forward voltage is given at chip level

Thermal properties [7]

Parameter	Symbol	Conditions	min	typ	max	Unit
IGBT thermal resistance junction to case	$R_{th(j-c)IGBT}$				0.0085	K/W
Diode thermal resistance junction to case	$R_{th(j-c)DIODE}$				0.017	K/W
IGBT thermal resistance case to heatsink [2]	$R_{th(c-s)IGBT}$	IGBT per switch, λ grease = 1W/m x K		0.009		K/W
Diode thermal resistance case to heatsink [7]	$R_{th(c-s)DIODE}$	Diode per switch, λ grease = 1W/m x K		0.018		K/W

[2] For detailed mounting instructions refer to ABB Document No. 5SYA2039

Mechanical properties [7]

Parameter	Symbol	Conditions		min	typ	max	Unit
Dimensions	L x W x H	Typical , see outline drawing			190 x 140 x 38		mm
Clearance distance in air	d_a	according to IEC 60664-1 and EN 50124-1	Term. to base:	23			mm
			Term. to term:	19			
Surface creepage distance	d_s	according to IEC 60664-1 and EN 50124-1	Term. to base:	33			mm
			Term. to term:	32			
Mass	m				1380		g

[7] Thermal and mechanical properties according to IEC 60747 – 15

Electrical configuration

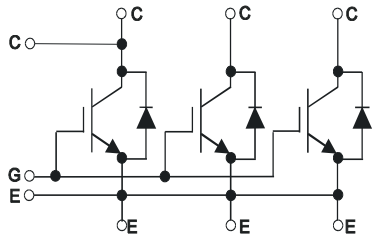

Outline drawing [2)]

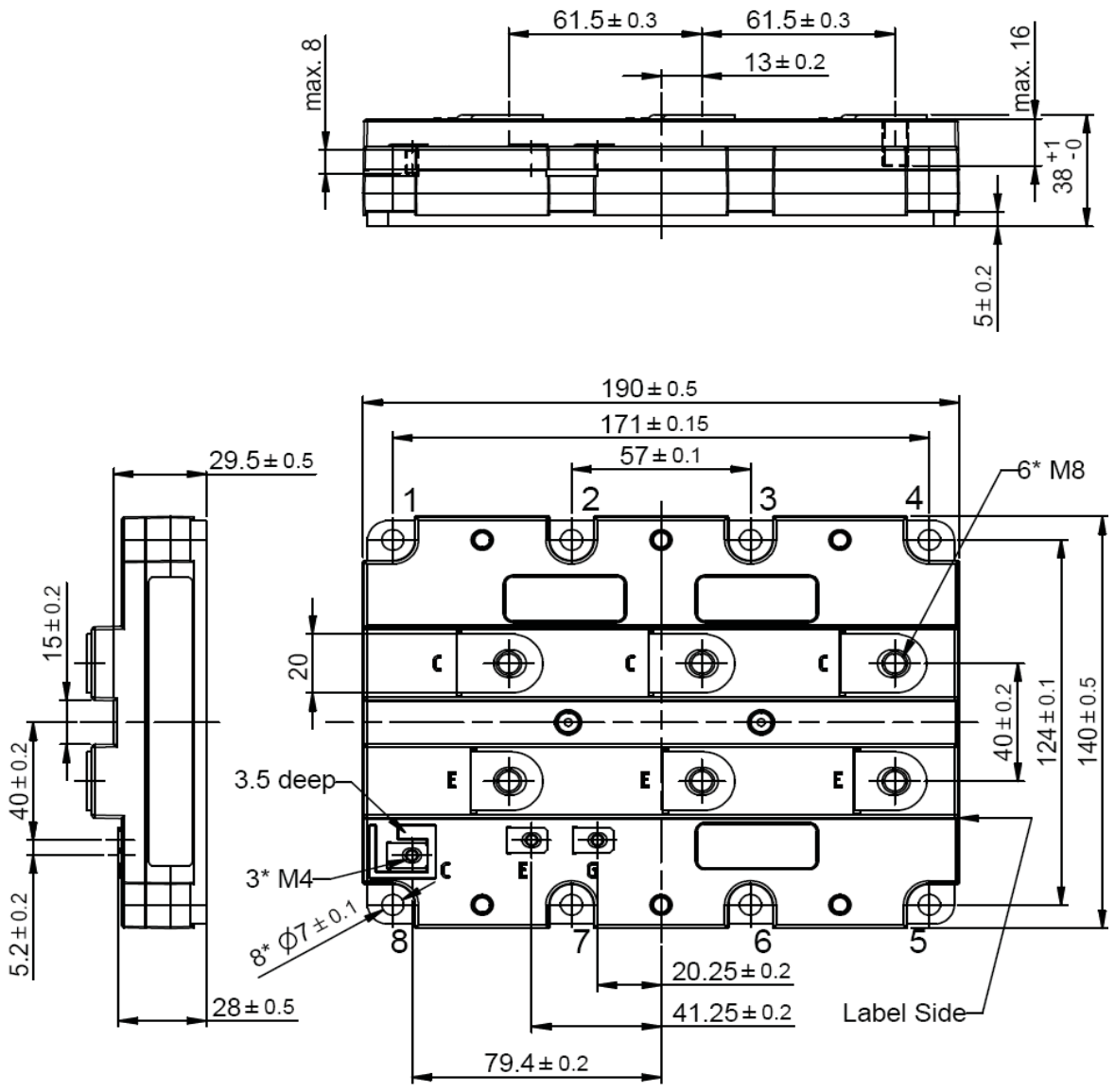

Note: all dimensions are shown in mm

[2)] For detailed mounting instructions refer to ABB Document No. 5SYA2039

This is an electrostatic sensitive device, please observe the international standard IEC 60747-1, chap. IX.

This product has been designed and qualified for Industrial Level.

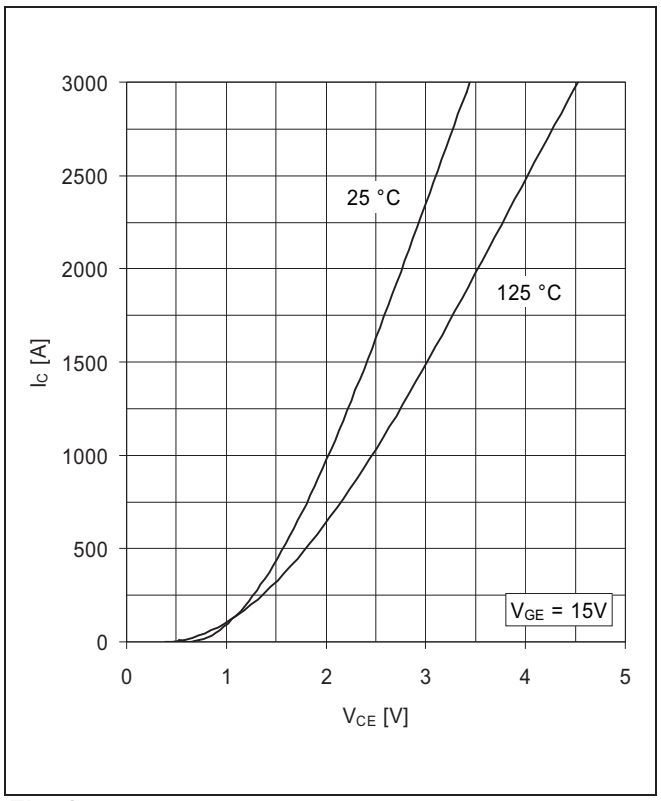

Fig. 1 Typical on-state characteristics, chip level

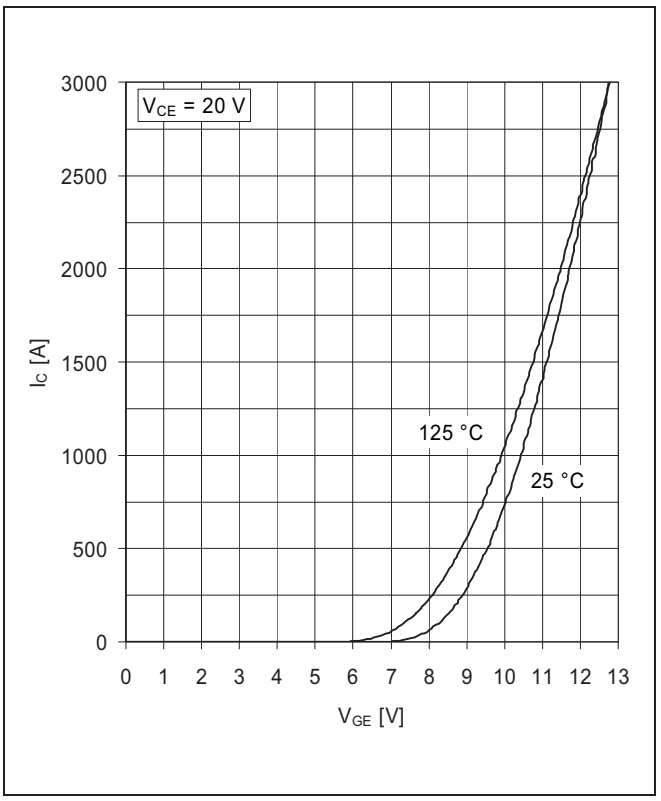

Fig. 2 Typical transfer characteristics, chip level

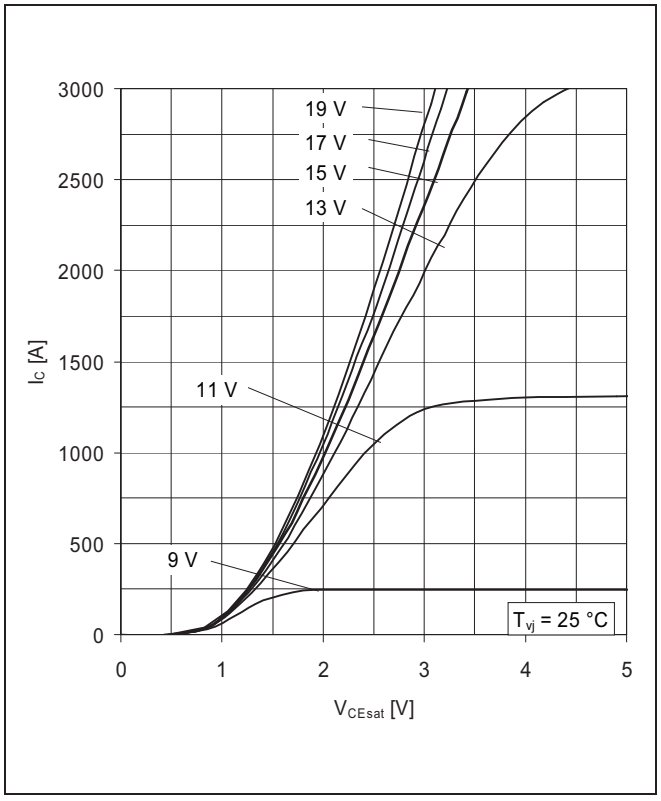

Fig. 3 Typical output characteristics, chip level

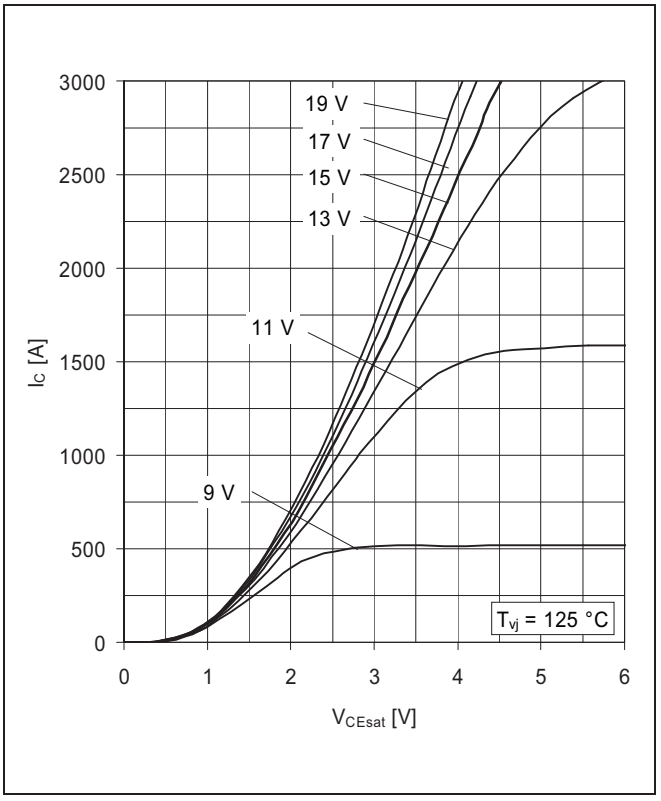

Fig. 4 Typical output characteristics, chip level

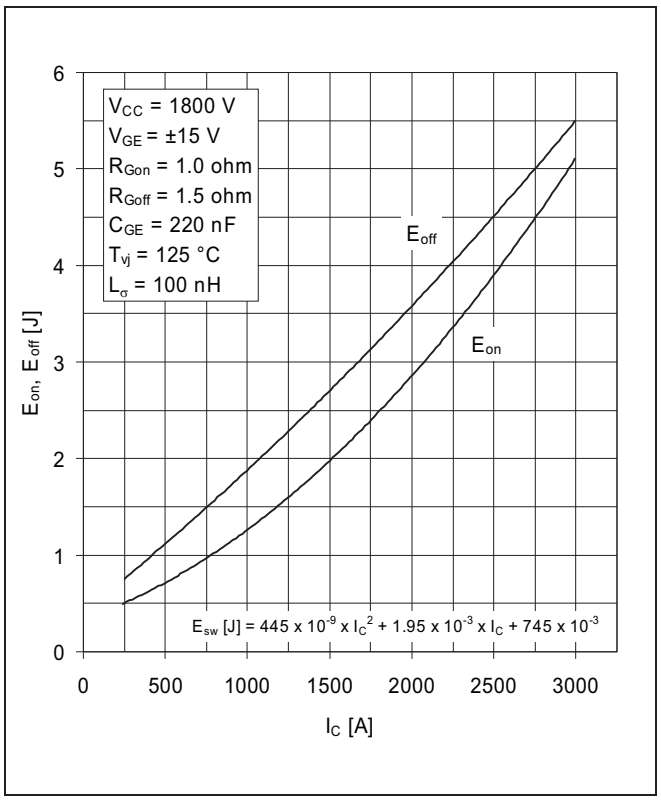

Fig. 5 Typical switching energies per pulse vs collector current

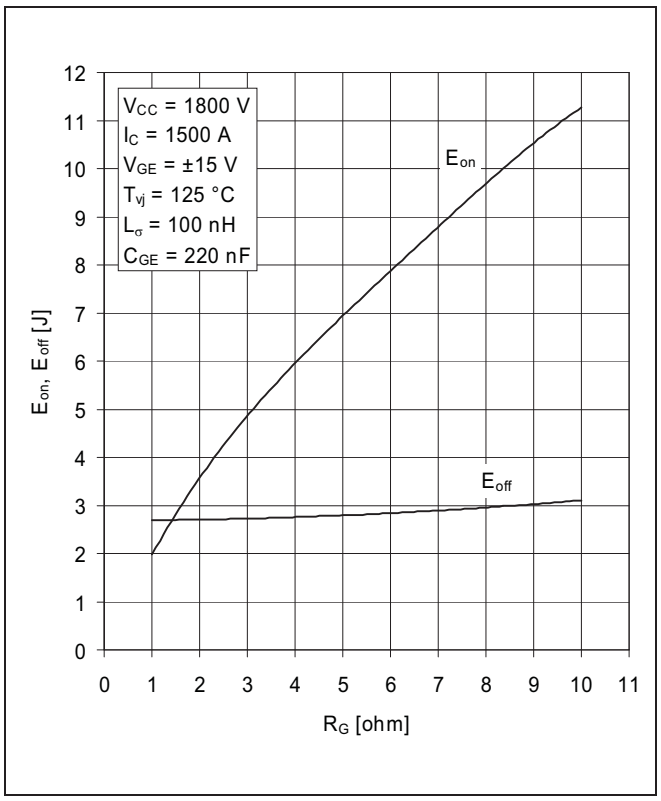

Fig. 6 Typical switching energies per pulse vs gate resistor

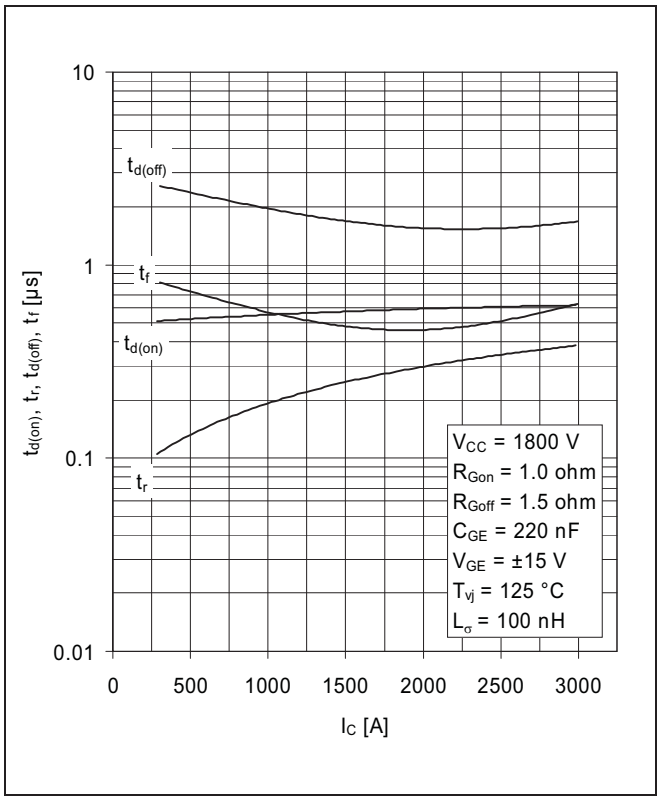

Fig. 7 Typical switching times vs collector current

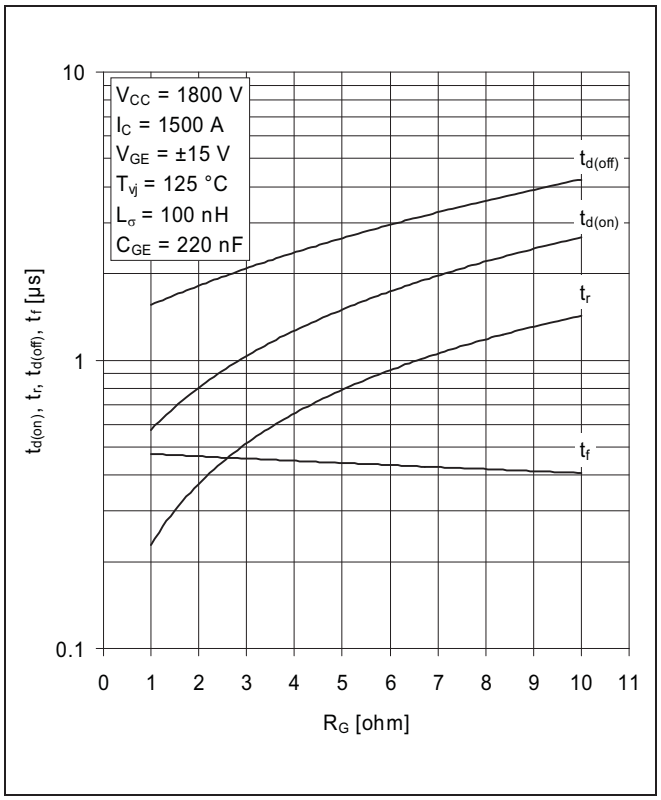

Fig. 8 Typical switching times vs gate resistor

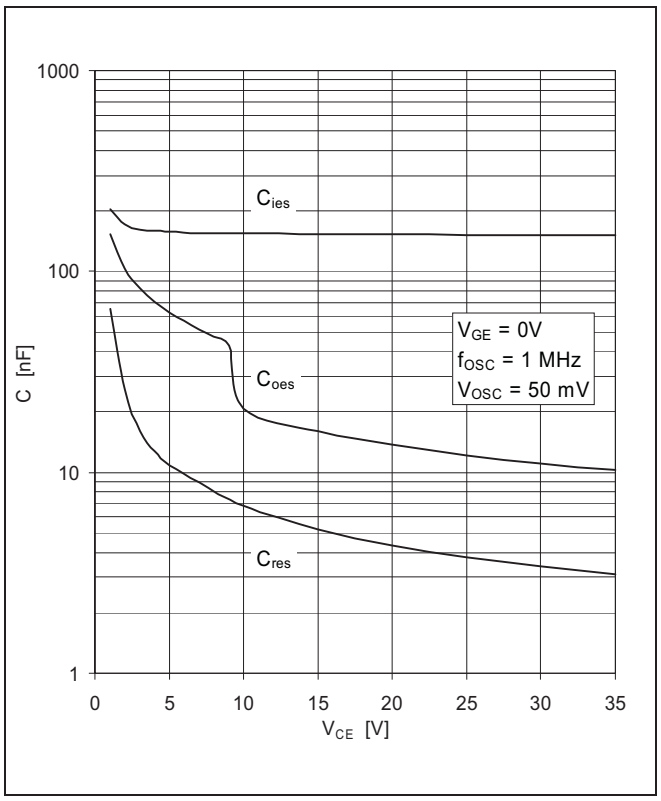

Fig. 9 Typical capacitances vs collector-emitter voltage

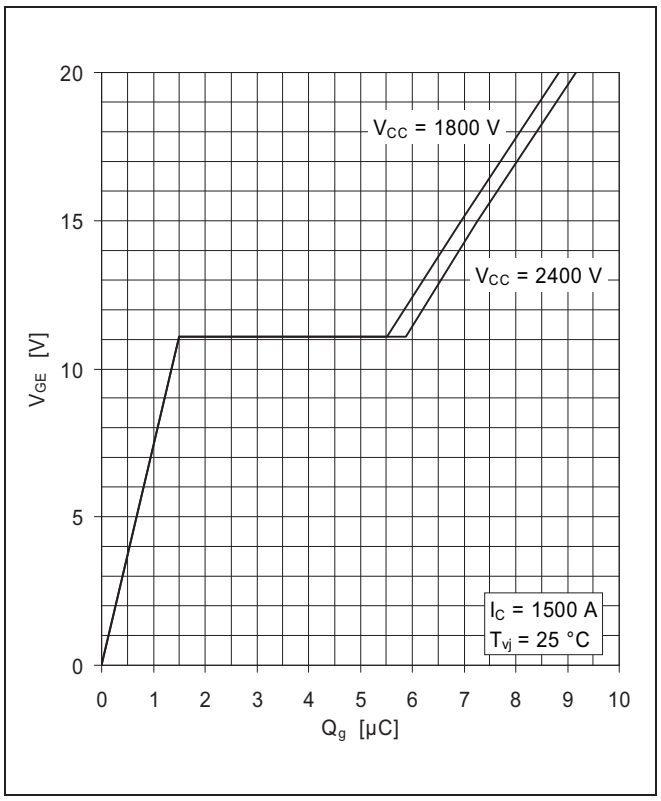

Fig. 10 Typical gate charge characteristics

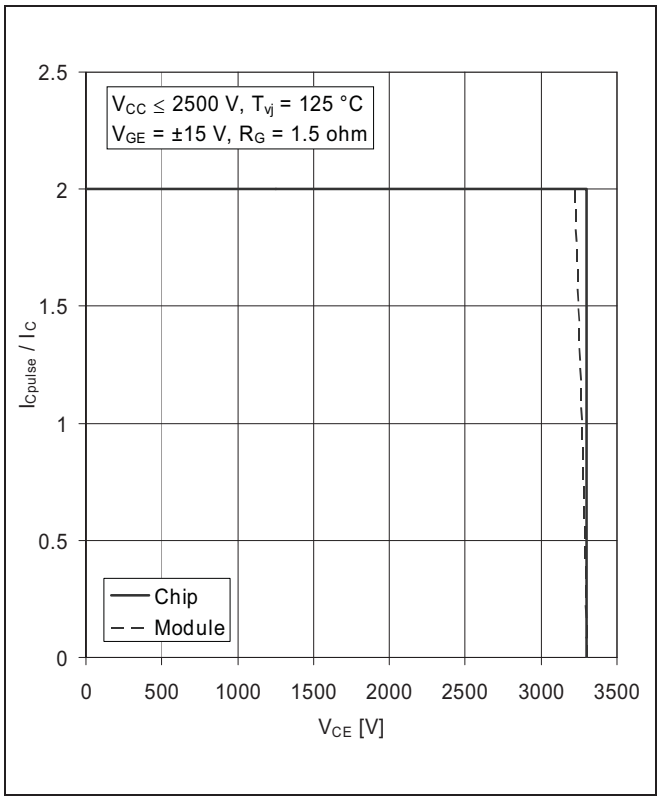

Fig. 11 Turn-off safe operating area (RBSOA)

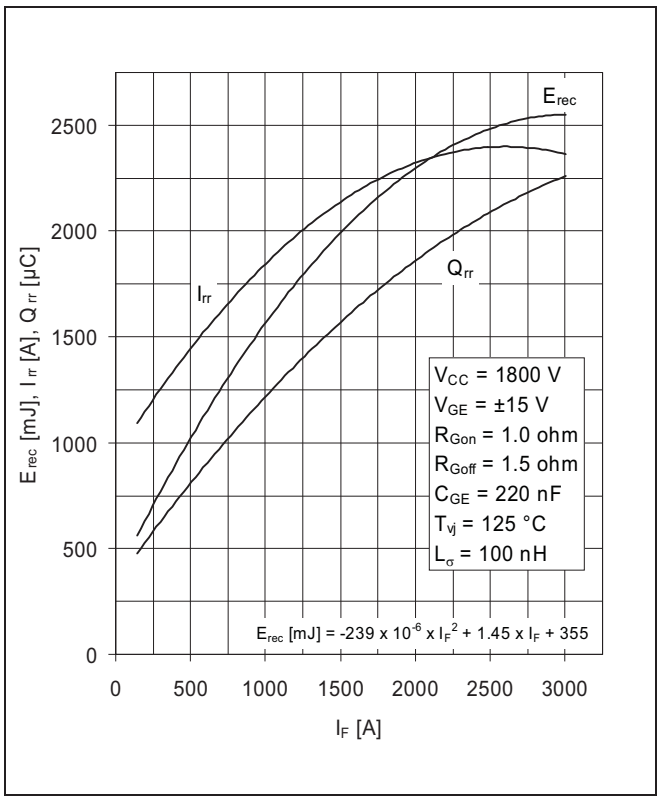

Fig. 12 Typical reverse recovery characteristics vs forward current

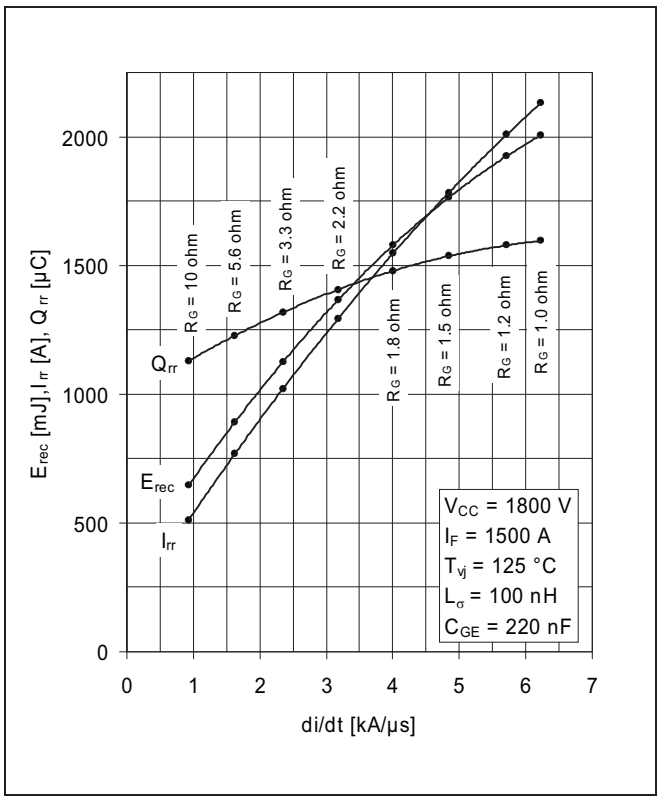

Fig. 13 Typical reverse recovery characteristics vs di/dt

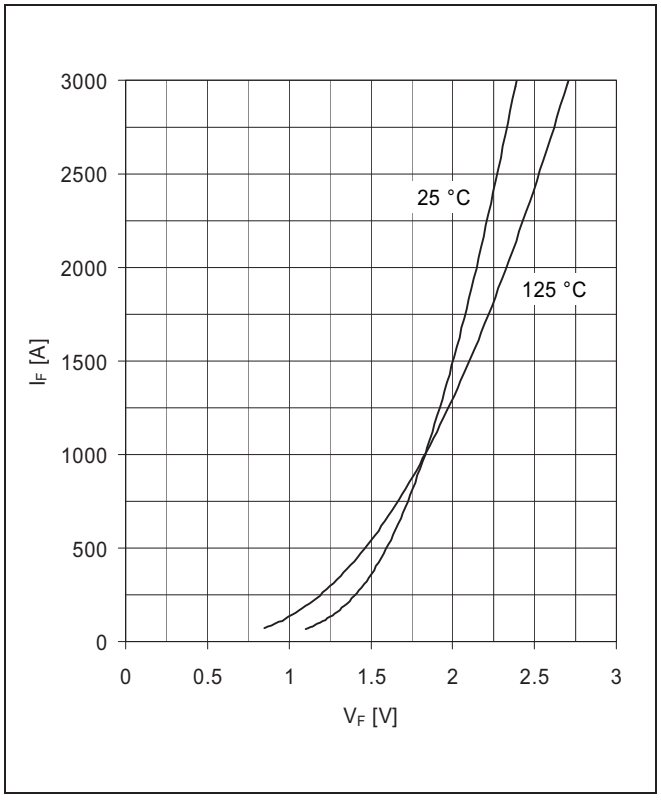

Fig. 14 Typical diode forward characteristics, chip level

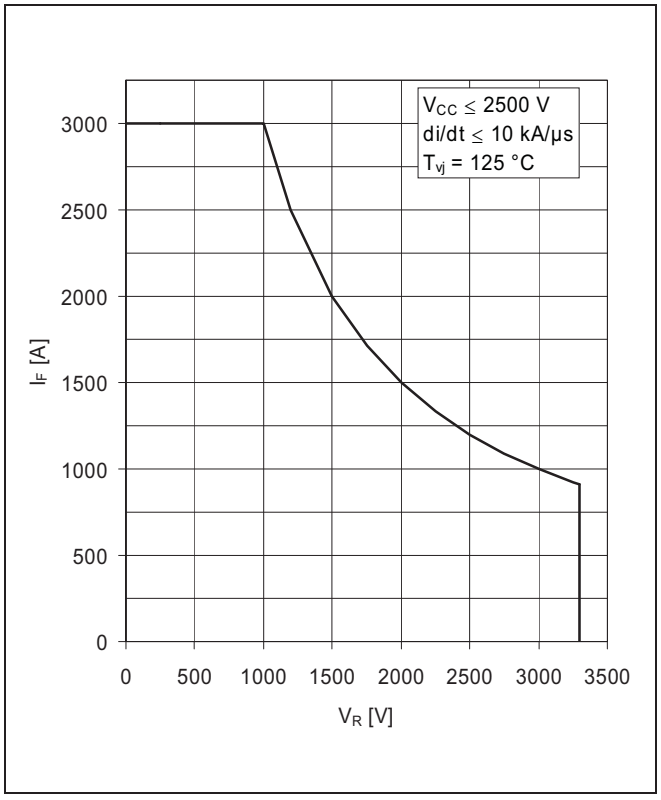

Fig. 15 Safe operating area diode (SOA)

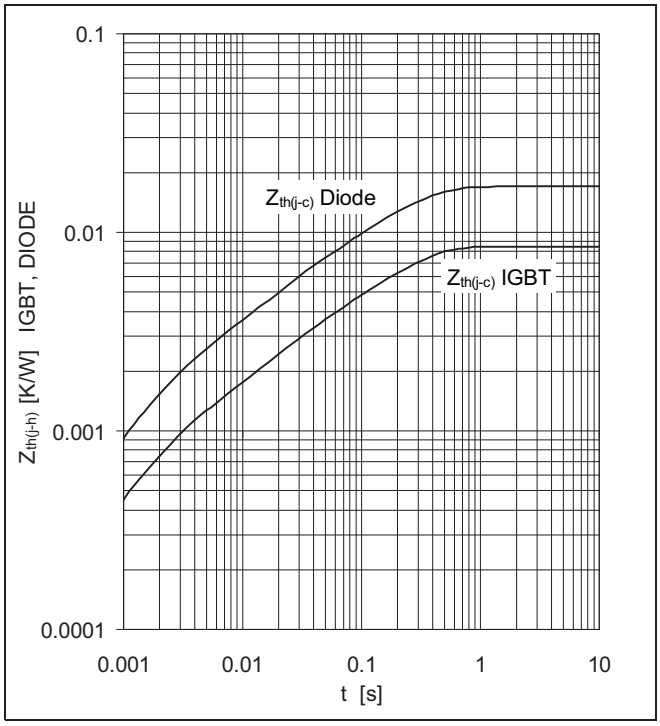

Fig. 16 Thermal impedance vs time

Analytical function for transient thermal impedance:

$$Z_{th\,(j\text{-}c)}(t) = \sum_{i=1}^{n} R_i\left(1 - e^{-t/\tau_i}\right)$$

	i	1	2	3	4	
IGBT	R_i(K/kW)	5.854	1.375	0.641	0.632	
	τ_i(ms)	207.4	30.1	7.55	1.57	
DIODE	R_i(K/kW)	11.54	2.887	1.229	1.295	
	τ_i(ms)	203.6	30.1	7.53	1.57	

For detailed information refer to:

- 5SYA 2042-02 Failure rates of HiPak modules due to cosmic rays
- 5SYA 2043-01 Load – cycle capability of HiPaks
- 5SZK 9120-00 Specification of environmental class for HiPak (available upon request)

ABB Switzerland Ltd
Semiconductors
Fabrikstrasse 3
CH-5600 Lenzburg, Switzerland

Telephone +41 (0)58 586 1419
Fax +41 (0)58 586 1306
Email abbsem@ch.abb.com
Internet www.abb.com/semiconductors

Doc. No. 5SYA 1595-00 July 07

V_{RRM}	=	4500	V
I_{FAVM}	=	1650	A
I_{FSM}	=	26	kA
V_{F0}	=	1.9	V
r_F	=	0.79	mΩ
V_{DClink}	=	2800	V

Fast Recovery Diode

5SDF 16L4503

PRELIMINARY

Doc. No. 5SYA1164-00 Sep. 01

- **Patented free-floating technology**
- **Industry standard housing**
- **Cosmic radiation withstand rating**
- **Low on-state and switching losses**
- **Optimized to use in snubberless operation**

Blocking

V_{RRM}	Repetitive peak reverse voltage	4500 V	Half sine wave, t_P = 10 ms, f = 50 Hz	
I_{RRM}	Repetitive peak reverse current	≤ 150 mA	$V_R = V_{RRM}$, T_j = 125°C	
V_{DClink}	Permanent DC voltage for 100 FIT failure rate	2800 V	100% Duty	Ambient cosmic radiation at sea level in open air.
V_{DClink}	Permanent DC voltage for 100 FIT failure rate	3200 V	5% Duty	

Mechanical data (see Fig. 6)

F_m	Mounting force	min.	36 kN	
		max.	70 kN	
a	Acceleration: Device unclamped Device clamped		 50 m/s^2 200 m/s^2	
m	Weight		1.45 kg	
D_S	Surface creepage distance		≥ 33 mm	
D_a	Air strike distance		≥ 14 mm	

On-state (see Fig. 3)

I_{FAVM}	Max. average on-state current	1650 A	Half sine wave, T_c = 70°C	
I_{FRMS}	Max. RMS on-state current	2590 A		
I_{FSM}	Max. peak non-repetitive surge current	26 kA	tp = 10 ms	Before surge: $T_c = T_j$ = 125°C
		47 kA	tp = 1 ms	
$\int I^2dt$	Max. surge current integral	$3.4 \cdot 10^6$ A^2s	tp = 10 ms	After surge: $V_R \approx 0$ V
		$1.1 \cdot 10^6$ A^2s	tp = 1 ms	
V_F	Forward voltage drop	≤ 4.51 V	I_F = 3300 A	T_j = 125°C
V_{F0}	Threshold voltage	1.9 V	Approximation for	
r_F	Slope resistance	0.79 mΩ	I_F = 500…4000 A	

Turn-on (see Fig. 2)

V_{fr}	Peak forward recovery voltage	≤ 80 V	di/dt = 600 A/µs, T_j = 125°C

Turn-off (see Fig. 5, 7)

di/dt_{crit}	Max. decay rate of on-state current	≤ 600 A/µs	I_F = 4000 A, T_j = 125 °C V_{Dclink} = 2800 V
I_{rr}	Reverse recovery current	≤ 1200 A	I_F = 3300 A, $V_{DC\text{-}Link}$ = 2800 V di/dt = 600 A/µs, L_{CL} = 300 nH C_{CL} = 8 µF, R_{CL} = 0.6 Ω, T_j = 125°C
Q_{rr}	Reverse recovery charge	≤ 3900 µC	
E_{rr}	Turn-off energy	≤ 9.0 J	

Thermal (see Fig. 1)

T_j	Operating junction temperature range	0...125°C		
T_{stg}	Storage temperature range	-40...125°C		
R_{thJC}	Thermal resistance junction to case	≤ 13 K/kW	Anode side cooled	F_m = 36… 70 kN
		≤ 13 K/kW	Cathode side cooled	
		≤ 6.5 K/kW	Double side cooled	
R_{thCH}	Thermal resistance case to heatsink	≤ 5 K/kW	Single side cooled	
		≤ 3 K/kW	Double side cooled	

Analytical function for transient thermal impedance.

$$Z_{thJC}(t) = \sum_{i=1}^{n} R_i(1 - e^{-t/\tau_i})$$

i	1	2	3	4
R_i(K/kW)	4.05	1.28	0.62	0.56
τ_i(s)	0.56685	0.10686	0.01239	0.00300
F_m = 36… 70 kN Double side cooled				

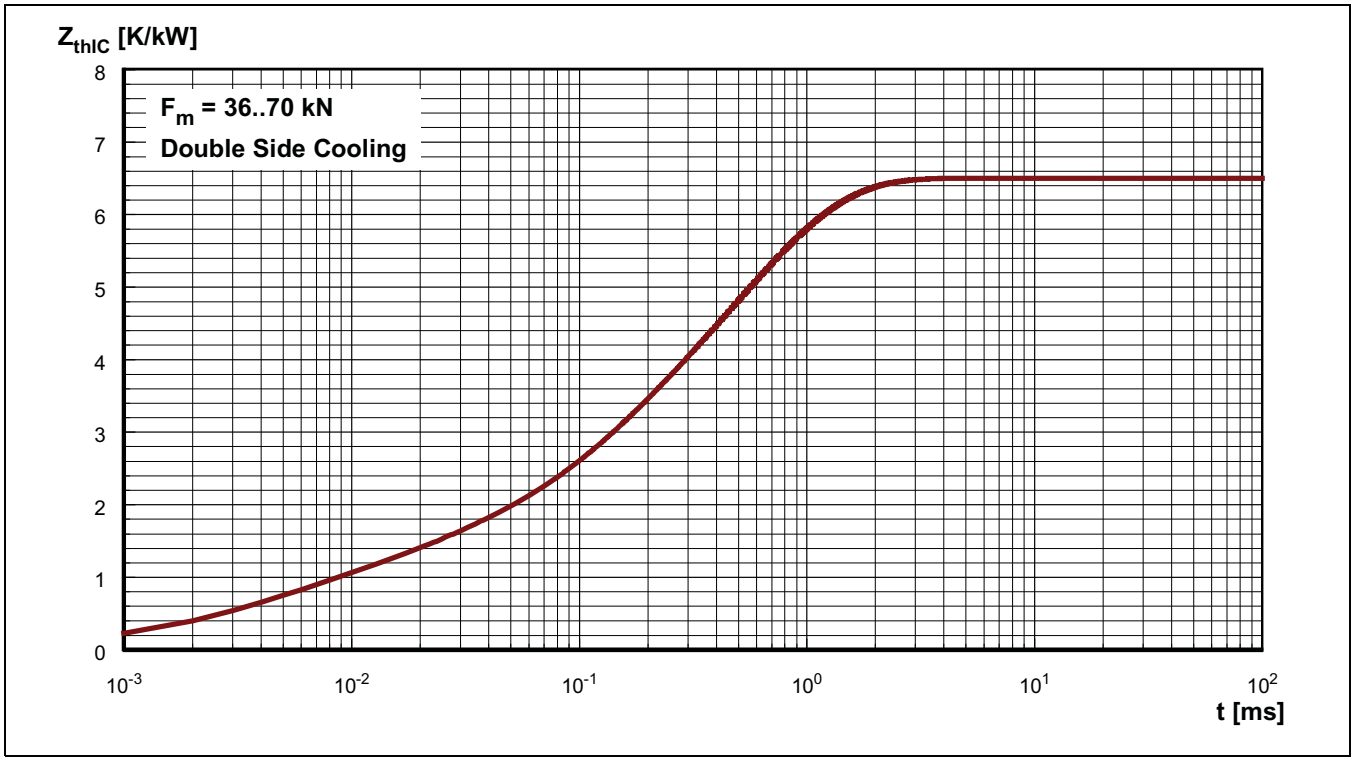

Fig. 1 Transient thermal impedance (junction to case) vs. time in analytical and graphical form (max. values).

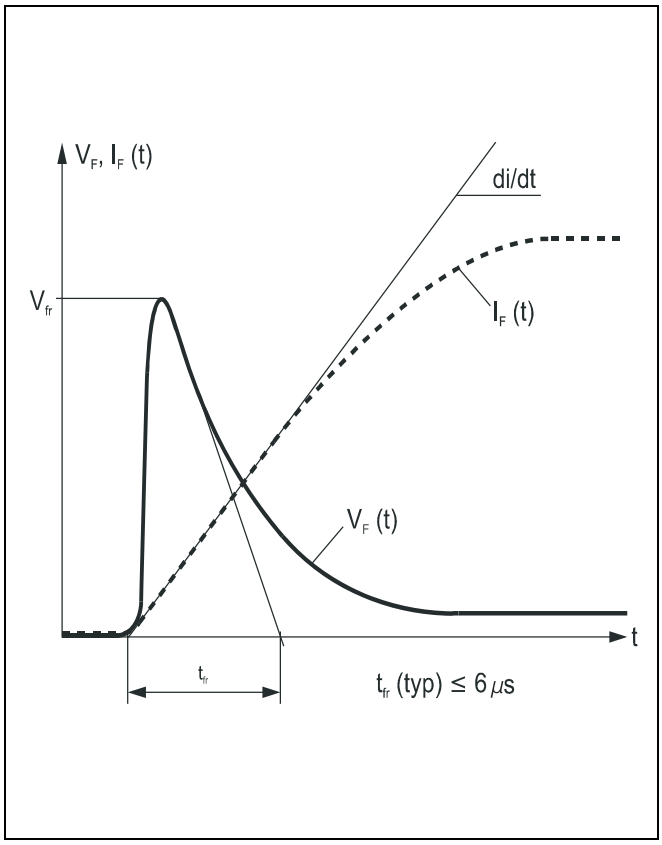

Fig. 2 Typical forward voltage waveform when the diode is turned on with high di/dt.

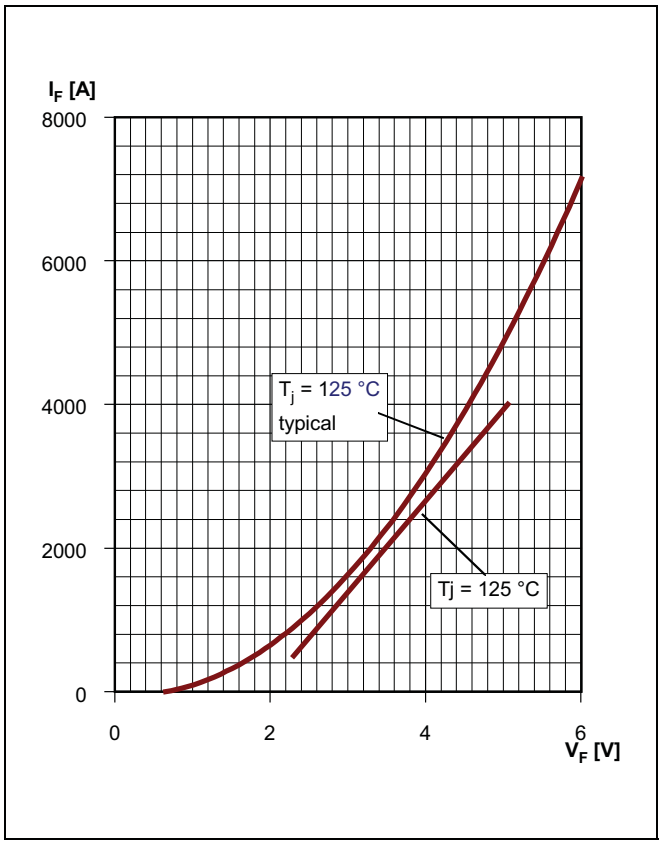

Fig. 3 Forward current vs. forward voltage.

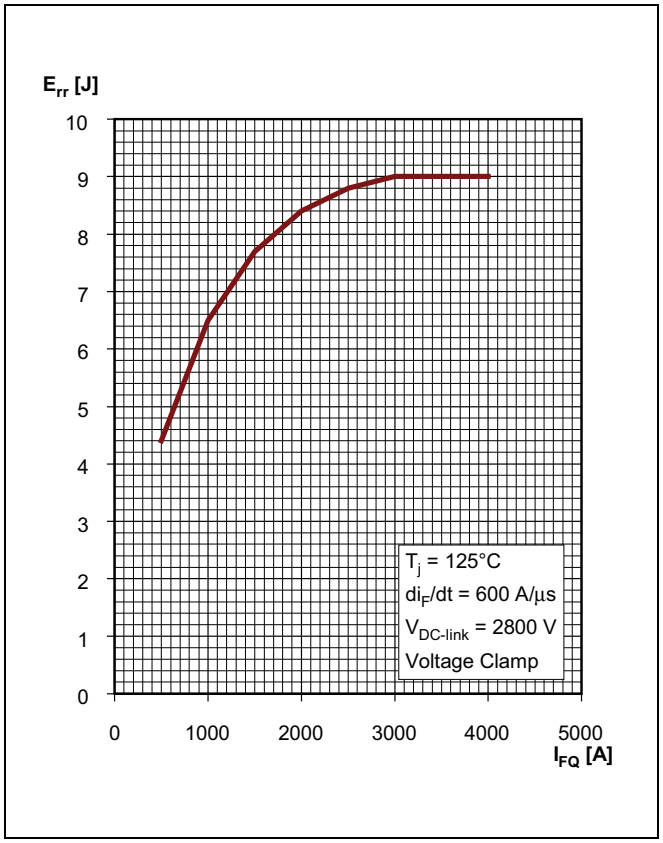

Fig. 4 Diode turn-off energy per pulse vs. turn-off current.

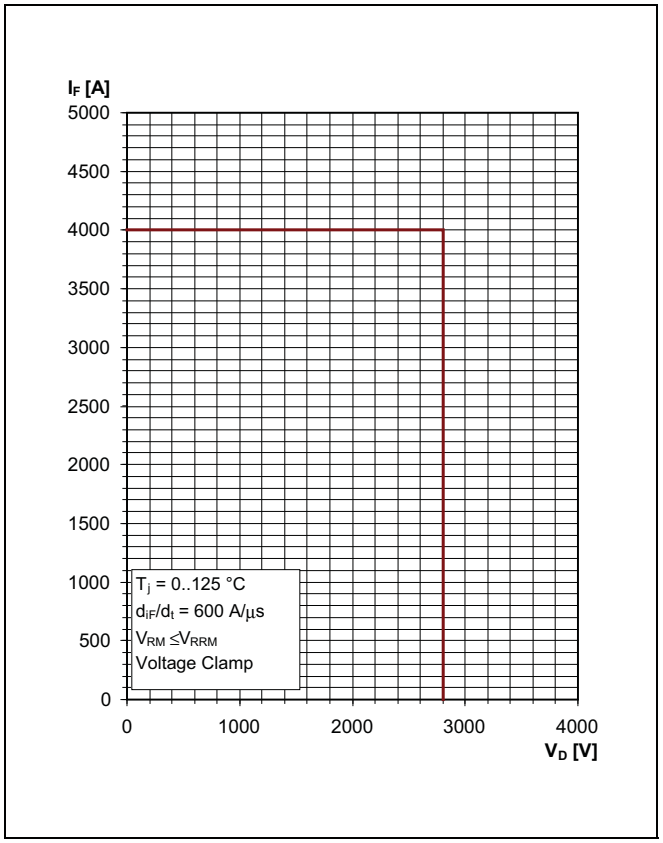

Fig. 5 Max. repetitive turn off current.

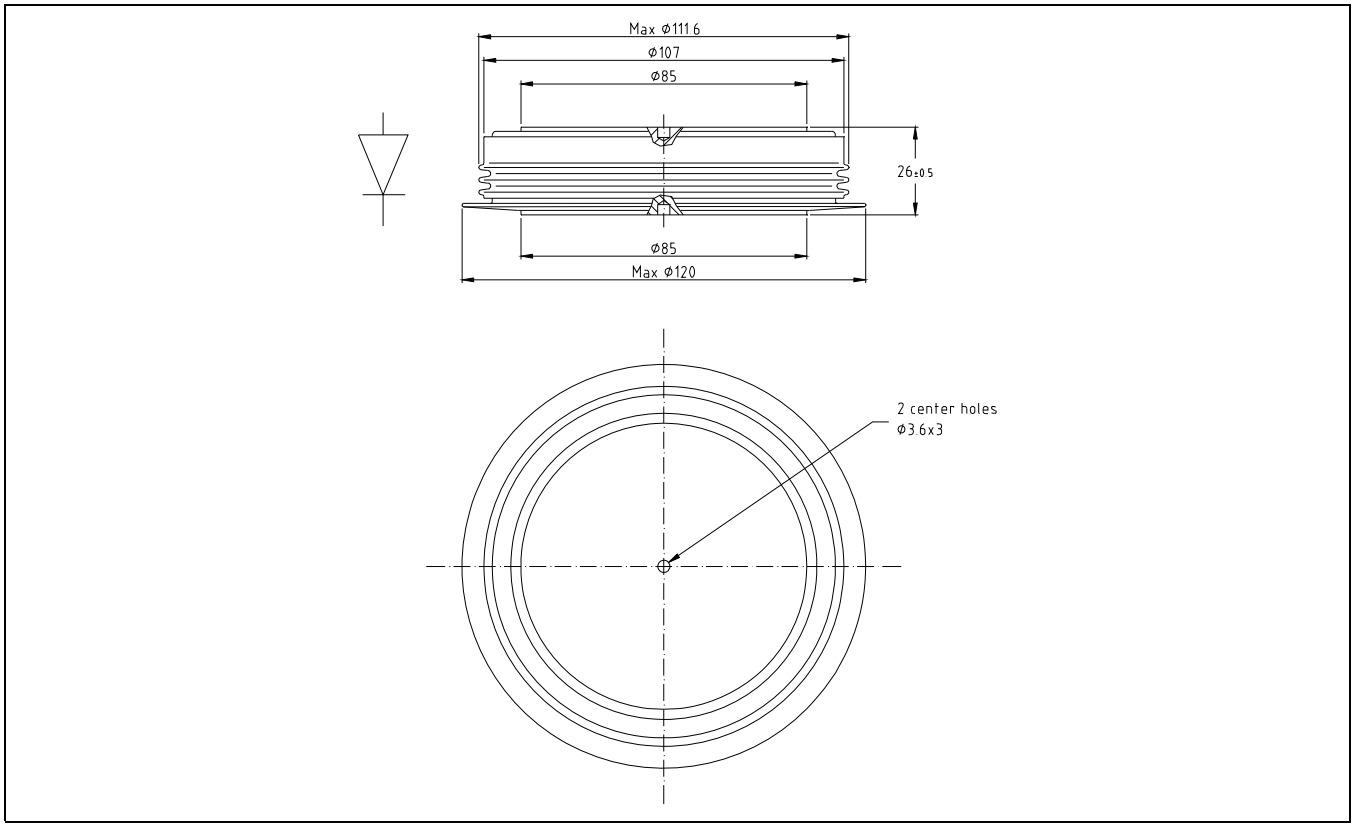

Fig. 6 Outline drawing. All dimensions are in millimeters and represent nominal values unless stated otherwise.

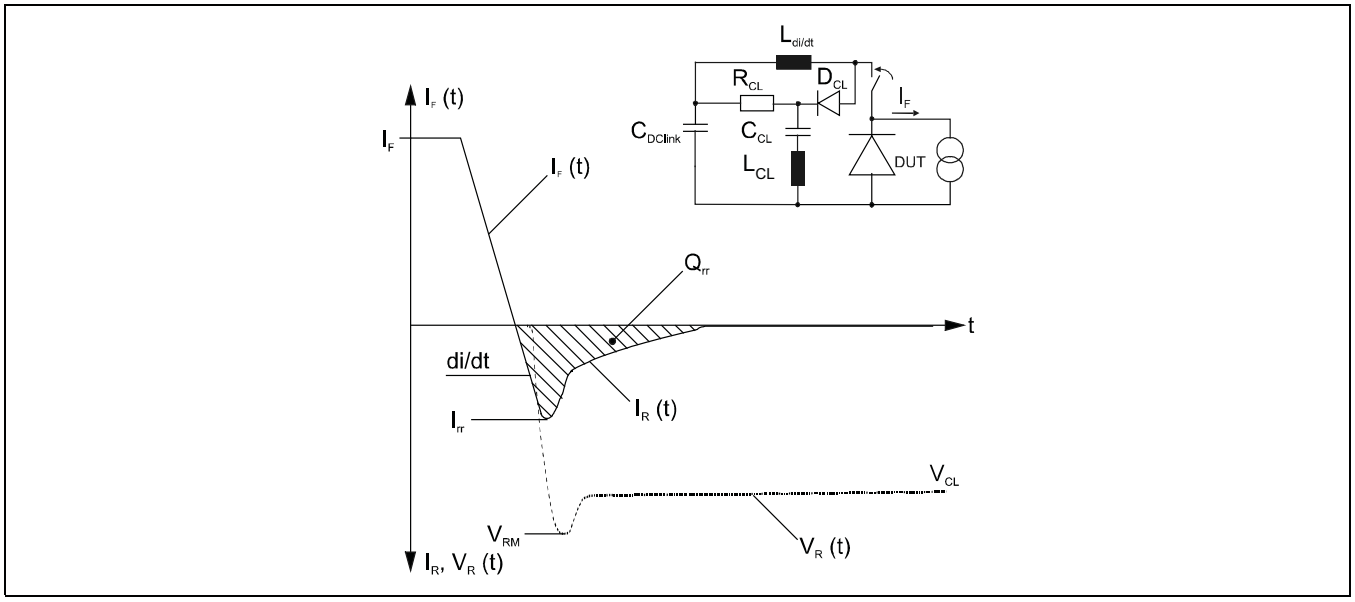

Fig. 7 Typical current and voltage waveforms at turn-off in a circuit with voltage clamp.

ABB Semiconductors AG reserves the right to change specifications without notice.

ABB Semiconductors AG
Fabrikstrasse 3
CH-5600 Lenzburg, Switzerland

Telephone +41 (0)62 888 6419
Fax +41 (0)62 888 6306
Email abbsem@ch.abb.com
Internet www.abbsem.com

Doc. No. 5SYA1164-00 Sep. 01